Porous Magnesium Zinc Oxide Layers for Photoanodes in Dye-Sensitized Solar Cells

Dissertation

zur Erlangung des Doktorgrades

der Naturwissenschaften

(Dr. rer. nat.)

vorgelegt von

Andreas Ringleb

dem Fachbereich 07

der Justus-Liebig-Universität Gießen

Supervisor & First Referee: Prof. Dr. Derck Schlettwein

Second Referee: Prof. Dr. Detlev Hofmann

Ehrenwörtliche Erklärung

Ich erkläre: Ich habe die vorgelegte Dissertation selbstständig und ohne unerlaubte fremde Hilfe und nur mit den Hilfen angefertigt, die ich in der Dissertation angegeben habe. Alle Textstellen, die wörtlich oder sinngemäß aus veröffentlichten Schriften entnommen sind, und alle Angaben, die auf mündlichen Auskünften beruhen, sind als solche kenntlich gemacht. Ich stimme einer evtl. Überprüfung meiner Dissertation durch eine Antiplagiat-Software zu. Bei den von mir durchgeführten und in der Dissertation erwähnten Untersuchungen habe ich die Grundsätze guter wissenschaftlicher Praxis, wie sie in der „Satzung der Justus-Liebig-Universität Gießen zur Sicherung guter wissenschaftlicher Praxis“ niedergelegt sind, eingehalten.

Andreas Ringleb
Gießen, den 10.12.2022

Kurzfassung

Farbstoffsensibilisierte Solarzellen (dye-sensitized solar cells, DSSCs) öffnen neue Räume für photovoltaische Anwendungen, welche bereits etablierten Solarzellkonzepten wie siliziumbasierten Solarzellen nicht zugänglich sind. Zinkoxid (ZnO) wird seit langem als vielversprechende Alternative zu den traditionell verwendeten Photoanoden auf der Basis von Titandioxid (TiO_2) in DSSCs untersucht, da es bessere Elektronentransporteigenschaften besitzt. Allerdings bleiben die Photokonversionseffizienzen (photo-conversion efficiencies, *PCEs*) von ZnO-basierten DSSCs im Allgemeinen hinter denen zurück, die von Titandioxid-basierten Zellen erreicht werden, insbesondere aufgrund einer niedrigeren Leerlaufspannung V_{OC}. In dieser Arbeit wurde die Mg-Dotierung von ZnO als ein vielversprechender Weg untersucht, um die V_{OC} in ZnO-basierten DSSCs durch eine Erhöhung der Energie des Leitungsbands deutlich zu erhöhen. Mesoporöse Schichten aus Mg-dotiertem ZnO (MZO) wurden sowohl in Form von homogen dotierten Nanopartikeln als auch von Core/Shell-Partikeln mit einer MZO-Schale und einem reinen ZnO-Kern hergestellt. Die erhaltenen Proben wurde mittels optischer und struktureller Analyse untersucht, um die Integration von Mg in das ZnO-Kristallgitter zu bestätigen, welche zu einer Vergrößerung der optischen Bandlücke in Abhängigkeit von der Mg-Konzentration führte. DSSCs, die aus homogen dotierten MZO-Nanopartikeln hergestellt wurden, wiesen eine deutlich erhöhte V_{OC} auf, litten aber bei höheren Mg-Konzentrationen unter stark verminderten Kurzschlussströmen J_{SC}. Eine detaillierte photoelektrochemische Analyse dieser Zellen zeigte eine fallenbedingte Erhöhung der Rekombinationsrate und des Transportwiderstands. Optimierte Core-Shell-Strukturen wurden durch Atomlagenabscheidung (ALD) von konformen MZO-Schichten kontrollierter Zusammensetzung und Dicke auf der inneren Oberfläche poröser ZnO-Schichten präpariert. DSSCs, die aus dieser gemischten Architektur hergestellt wurden, zeigten im Vergleich zu vollständig dotierten Nanopartikeln eine viel höhere Beibehaltung der J_{SC} bei hohen Mg-Konzentrationen, was auf die Vermeidung von erhöhten Transportwiderständen zurückzuführen ist. In Verbindung mit einer deutlich erhöhten V_{OC} führte dies zu einer insgesamt höheren PCE für Zellen mit MZO.

Abstract

Dye-sensitized solar cells (DSSCs) open new possibilities for photovoltaic applications that are inaccessible to established solar cell concepts, such as silicon-based photovoltaics. Due to its superior electron transport characteristics, zinc oxide (ZnO) has long been studied as a promising alternative to the traditionally used titanium dioxide (TiO_2)-based photoanodes in DSSCs. However, photo conversion efficiencies (PCEs) of ZnO-based DSSCs generally lack behind the ones reached by titania-based cells, specifically due to lower open-circuit voltages V_{OC}. The present study investigated Mg doping of ZnO as a promising way to significantly increase the V_{OC} in ZnO-based DSSCs through an upward shift of the conduction band energy. Mesoporous layers of Mg-doped ZnO (MZO) have been prepared in the form of homogenously doped nanoparticles and core-shell particles with an MZO shell and a pure ZnO core. Optical and structural analysis was performed to confirm the integration of Mg into the ZnO crystal lattice, which increased the optical band gap depending on the respective Mg concentration. DSSCs prepared from homogeneously doped MZO nanoparticles exhibited significantly increased V_{OC} but suffered from strongly reduced short-circuit currents J_{SC} at higher Mg concentrations. Detailed photoelectrochemical analysis of these cells revealed a trap-related increase in recombination rate and transport resistance. Optimized core-shell structures were fabricated by atomic layer deposition (ALD) of conformal MZO layers of controlled composition and thickness on the internal surface of porous ZnO layers. DSSCs built from this hybrid architecture showed much higher conservation of J_{SC} at high Mg concentrations than homogenously doped nanoparticles due to the prevention of increased transport resistance. Coupled with significantly increased V_{OC}, this resulted in an overall increased PCE for cells containing MZO.

Table of Contents

1. Introduction

On November 15th, 2022, the United Nations announced that Earth's population has reached 8 billion people after having quadrupled in the last century.[1] This explosive growth was fueled by energy gained from fossil fuel sources such as gas, oil, and coal, whose consumption increased in step with the population.[2] Awareness of the impact of continued fossil fuel consumption on the climate has spread over the last decade, putting these issues in the focus of society and politics worldwide and also in my home country Germany. Protest movements like Fridays For Future or the Last Generation use increasingly extreme methods to demand political changes, while political parties with environmentally-centered agendas increasingly succeed in our national and European Parliament elections.[3,4] The war in Ukraine has further highlighted the dependence on fossil fuel sources and the importance of an independent energy supply. Increased cost of living and an economic downturn due to rising energy costs, climate change and extreme weather phenomena were the four most increased fears of German citizens in 2022, making the demand for clean energy higher than ever.[5]

Together with hydropower and wind energy, solar energy is among the biggest natural sources of energy for power generation and presents the most potential.[6] Applications to harvest solar energy are varied, but only photovoltaic cells, also called solar cells, enable the direct conversion of solar into electrical energy. Massive solar parks with thousands of solar panels based on highly crystalline silicon are used to produce the majority of the electricity currently generated from solar energy.[7] However, they require a significant amount of land to be covered and are often rejected by the neighboring population due to their aesthetics.[8] While increasing the efficiency of these cells presents a clear way to raise the amount of energy generated from sun light, unlocking new spaces for photovoltaic applications has the potential to expand solar cell coverage significantly, especially in urban areas. Dye-sensitized solar cells (DSSCs) may be the key to unlock these areas due to their semitransparency, their unique characteristics under low-intensity light and their aesthetic variability.[9]

While DSSCs already existed before 1991, they were brought to scientific attention when Michael Grätzel and Brian O'Regan published the first DSSC with a revised cell architecture, raising the energy conversion yield from below 1% to 7%.[10,11] With the declared goal of developing a low-cost alternative to the traditional solar cell concept, that publication marked the starting point for an entirely new branch of solar cell research. In contrast to previously established solar cell concepts, the semiconductor only serves as an electron transport material, while providing the structure for the dye to attach to. A liquid redox electrolyte regenerates the

dye, with the difference between the redox potential and the local Fermi energy in the semiconductor providing the voltage for the cell. The efficiency of DSSCs measured under laboratory conditions is rather low due to limitation of the current density under high-intensity light, such as the standard AM1.5G sunlight, with record efficiencies reaching only 14%.[12] However, measured under indoor light conditions, the efficiency of DSSCs rises above 30%, competing with that of silicon-based and other thin film solar cells.[9] DSSC's ability to harvest light under glazing and ambient light conditions makes them well suited to power consumer electronics such as head phones, portable speakers, sensors, remote controls or lights. This concept is already put into practice by the Swedish company Exeger, which integrates flexible DSSCs into their designs to fully cover their energy consumption.[13] Pilot projects like the installation of semitransparent, colorful DSSC panels in the SwissTech Convention Center in Lausanne and the Science Tower in Graz show the possible integration of solar cells in urban spaces with a new aesthetic. DSSCs, therefore, do not represent a possible replacement for traditional solar cell concepts, but an extension into underdeveloped terrain.

Recent advances in DSSC research were focused on the development of new dyes[14–16], electrolytes[14,17,18], and counter-electrodes[19], while the underlying semiconductor remained remarkably unchanged. Despite extensive research into different materials, preparation methods, and morphologies, nanoparticulate TiO_2 remains the standard semiconductor in high-efficiency DSSCs, with ZnO emerging as the only alternative. Motivated by a much higher electron mobility, extensive research has led to the preparation of ZnO-based DSSCs with efficiencies of up to 8%, still falling considerably short of the efficiencies reached by TiO_2-based cells of 14%.[12,20] While this difference in PCE can be partially attributed to the lack of optimized dyes and redox electrolytes for ZnO-based DSSCs, a comparative study by Grätzel et al. found fundamental differences in DSSC based on Al_2O_3 particles coated with thin layers of ZnO or TiO_2 by atomic layer deposition (ALD).[21–23] While the cells containing ZnO were able to reach higher photocurrents due to their faster electron transport, these gains are more than mitigated by faster recombination rates, leading to considerably reduced V_{OC} and fill factors *FF* compared to TiO_2-based cells.[21,24] These losses in V_{OC} can be observed across nearly all possible combinations of state-of-the-art dyes and electrolytes and prevent ZnO from becoming genuinely competitive as an electrode material in DSSCs.[24] A new approach is clearly needed in order to increase V_{OC} and close the gap to TiO_2-based DSSCs. Modification of the bulk or surface composition of ZnO with metal or rare earth ions has shown the potential to increase the V_{OC}, but often led to significant complications due to changes in crystal strucutre.[25–27] In contrast, the cationic substitution of Zn^{2+} (0.57 Å) with Mg^{2+} (0.60 Å) preserves the ZnO

wurtzite structure for Mg concentrations up to 33%, depending on the growth technique, due to the similar ionic radii.[28] Mg-doped ZnO $Mg_xZn_{1-x}O$ (MZO) has been used in various solar cell concepts as electron transport layer due to its enhanced electron mobility at low Mg concentrations and its tunable band gap.[29–31] In DSSCs, MZO has shown the potential to significantly increase V_{OC}, due to an upward shift of the quasi-Fermi level compared to pure ZnO. Nevertheless, studies so far have only been able to prepare MZO for DSSCs in non-standard morphologies, such as nanorods and nanosheets.[32–34] The negative effect of MZO on the J_{SC} of photovoltaic cells, especially at higher Mg concentration, has been discussed either in the context of electron transport or electron recombination.

The aim of this work is to achieve an increase in the efficiency of ZnO-based DSSCs through the use of Mg-doping. The tunable band structure of MZO has shown the potential to allow the V_{OC} of ZnO-based DSSCs to reach or even surpass the V_{OC} exhibited by TiO_2-based cells. Publication (I) of this cumulative dissertation contains a detailed study on the preparation of homogenously doped MZO nanoparticles, as well as their structural and optical properties. The photoelectrochemical analysis of the DSSCs fabricated from nanoparticulate MZO photoanodes focuses on the charge-transfer processes inside the cell in order to better understand losses of the J_{SC} at high Mg concentrations. Publication (II) presents an alternative approach to combine ZnO and MZO in an optimized core-shell structure to prevent these losses and fully utilize the enhanced V_{OC}.

2. Fundamentals

2.1 Dye-sensitized solar cells

2.1.1. Structure and basic operation principles

Since the seminal publication of Grätzel and O'Regan in 1991, the basic structure of DSSCs has primarily remained the same despite extensive optimization efforts.[10] As shown schematically in Figure **1**, all of the components of a DSSC are sandwiched between two glass substrates coated with a transparent conducting oxide (TCO).[35,36] A mesoporous layer of a wide band gap semiconductor is deposited on top of one of these substrates. A monolayer of a dye as sensitizer is attached to the surface of the semiconductor, completing the working electrode (WE) of the photovoltaic cell. The counter electrode is comprised of the second TCO-coated substrate and an additional catalytic layer, such as platinum, graphite, or a conductive polymer.[37] A liquid redox electrolyte connects both electrodes.

While the device's function has proven to be based on the complex interaction of multiple components on a molecular level, its fundamental principle of operation can be broken down into just six steps.[36,38] The green arrows in Figure **1** indicate desired processes for the current generation, whereas the red arrows highlight partially unavoidable loss mechanisms.

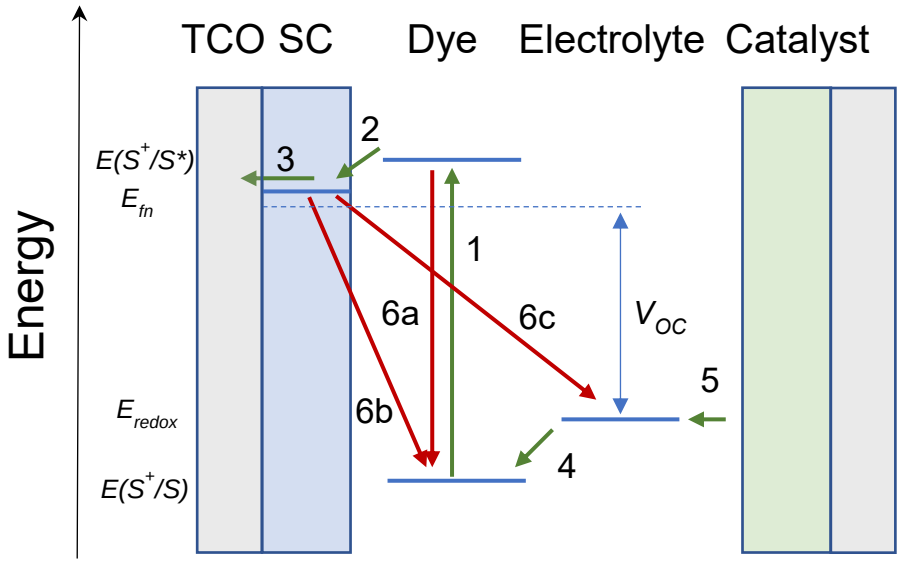

Figure 1 Schematic structure and principle of operation of a DSSC. *Shown are the energy level alignments of the working electrode, consisting of a TCO and a semiconductor (SC), the ground ($E(S^+/S)$) and the excited state ($E(S^+/S^*)$) of the dye, with the quasi-Fermi E_{fn}, and the redox energy level of the electrolyte shown as a dashed line.*

Absorption of an incident photon generates an excited dye molecule (step 1), which injects an electron into the semiconductor's conduction band (step 2).[36] The injected electron is transported through the mesoporous semiconductor network and collected at the TCO (step 3). The redox electrolyte regenerates the oxidized dye and transports the charge to the counter electrode by diffusion (step 4), where it is reduced again (step 5). Several recombination pathways reduce the efficiency of this sequence. Radiative recombination of the excited dye (step 6a) is thermodynamically unavoidable and leads to a reduced number of electrons available for injection. However, recombination from the semiconductor to the oxidized dye molecule (step 6b) or the electrolyte (step 6c) often dominate the recombination reactions, but can be influenced by the design of the dye molecule and the semiconductor/electrolyte interface.[39]

2.1.2 Role of the semiconductor in DSSCs

For each of the described components of a DSSC, a huge variety of alternatives and combinations have been researched and published over the last 30 years. However, due to the focus of this work, a spotlight will be put on the role of the semiconductor in DSSCs.

2.1.2.1 Structure

Introducing a porous TiO_2 layer with a high internal surface area was the defining factor that allowed Grätzel and O'Regan (1991) to strongly increase the efficiency of DSSCs.[10,36] Previous iterations of DSSCs operated only using smooth semiconductor surfaces.[40,41] The mesoporous TiO_2 layer allowed for a manifold increase in dye loading while being transparent to light in the visible range of the spectrum. Metal oxide semiconductors for DSSCs have been prepared from solution[42], including hydrothermal synthesis[43] and electrodeposition[44], gas phase[45], sputtering[46], and many more, creating an extensive tool kit for the preparation of nanostructured layers.[47,48] With the primary requirement of a high internal surface area, a vast variety of nanostructured semiconductors has been studied and reported, including but not limited to nanoparticles[42,48], nanowires[49,50], nanotubes[51,52], nanosheets[53,54], or core-shell structures[55,56]. The need for the electrolyte to fully infiltrate the layer and enable efficient dye regeneration calls for additional requirements on the structure of the semiconductor. Compromises must be made between internal surface area and porosity to avoid diffusion limitation of the J_{SC}.[57] The structure of the mesoporous layer also influences electron transport to the TCO, which is another core task of the semiconductor in DSSCs. Higher crystallinity, the avoidance of grain boundaries, and short diffusion pathways have all proven to be beneficial for electron transport (see 2.1.3.3).[47] In addition, combining different nanostructures, such as

the layering of nanoparticles of varying sizes, has improved the power conversion efficiency by backscattering the incident light.[36]

2.1.2.2 Energy levels and interactions

Besides their physical structure, the energy levels of semiconductors are significant for the function and performance of DSSCs. To ensure the efficient injection of electrons from the dye into the semiconductor, the energetic overlap between the excited state of the dye $E^0(S^+/S^*)$ and the unoccupied acceptor states of the semiconductor conduction band is needed (see 2.1.3.2).[38] The equilibrium Fermi energy level E_f in a semiconductor is given by[58]

$$E_f = E_c + k_B T \, ln\left(\frac{n_c}{N_c}\right) \qquad (1)$$

with the conduction band edge E_c, the thermal energy k_BT, the density of conduction band electrons n_c, and the effective density of conduction band states N_c. In the dark, E_f equals the electrochemical potential of electrons in the electrolyte, often referred to as the redox potential E_{redox} (Figure **2 a**).[36,59] Upon illumination, electrons from the excited dye molecule are injected into the semiconductor. The increased electron density in the semiconductor gives rise to a non-equilibrium quasi-Fermi energy E_{fn} with the potential difference between E_{fn} and E_{redox} defining the maximum theoretical photovoltage V_{OC} under open-circuit conditions.[39,60] Under these conditions, zero current flows and E_{fn} is constant across the entire semiconductor layer (Figure **2 b**). However, under short-circuit conditions E_{fn} decreases exponentially throughout the layer towards the TCO, reaching E_{redox} at the surface of the TCO and resulting in zero voltage overall (Figure **2 c**).[36,59] At the maximum power point, a current flows and E_{fn} decreases at the TCO, resulting in a voltage smaller than V_{OC} (Figure **2 d**).

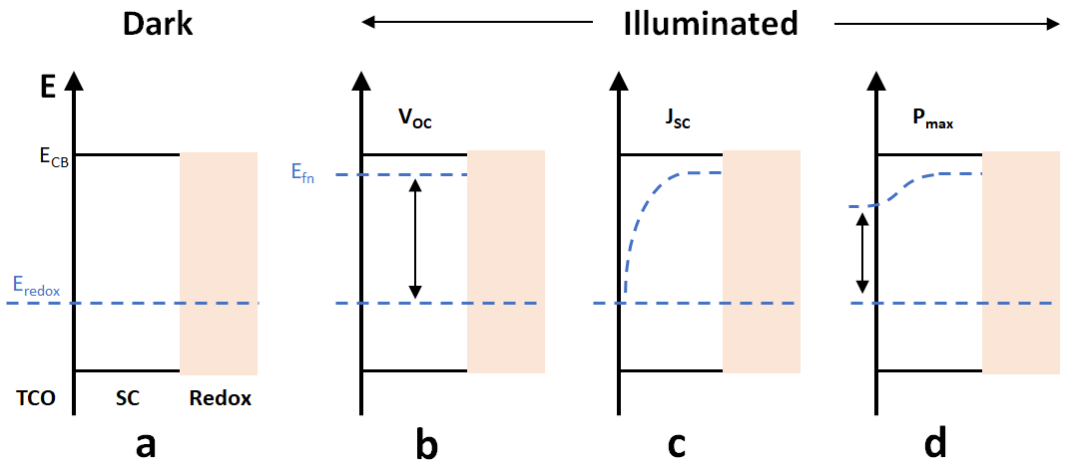

Figure 2. Quasi-Fermi energy in a DSSC. *Energy levels across the TCO, the semiconductor (SC) and the redox electrolyte (Redox) in the dark (a) and under illumination at open-circuit (b), short-circuit (c) and maximum power (d). Black arrows represent the achievable voltage under the respective conditions.*

Interactions of the semiconductor with other components of the DSSC are complex and, although crucial to cell performance, mostly understood on a phenomenological level only. The idea to influence the position of the conduction band edge through additives in the liquid electrolyte emerged early as a possible avenue to increase V_{OC} and overall cell efficiency.[61] The commonly used additive 4-tert-butyl pydridine (TPB) has been shown to increase V_{OC} and electron lifetimes, although possible explanations for this effect range from passivation of surface trap states[62] or sterically hindering recombination through adsorption on the semiconductor surface[63] to forming bulky complexes with the oxidized redox species.[64,65] Other common additives, such as Li^+ ions have even been shown to adsorb on the surface and cause a downward shift of E_c, thus decreasing the V_{OC}, but having a positive effect on J_{SC}.[36,66] Moreover, both additives are known to show varying interactions and levels of enhancement with different redox electrolytes and semiconductors, making them a highly complex way of influencing cell performance through interaction with the conduction band edge.[67] The study at hand presents a more direct method to increase the maximum achievable V_{OC} of a photoanode material through modification of the semiconductor.

2.1.3 Charge transfer processes

While the basic principle of operation is quickly described, a more detailed look at the relevant charge transfer processes is needed to provide a better understanding of the topic of the present work. As such, a focus will be put on the processes involving the semiconductor.

2.1.3.1 Excitation

Absorption of incident light in a DSSC occurs by excitation of an electron from the dye ground state $E^0(S^+/S)$ to an excited state $E^0(S^+/S^*)$, thereby converting photon energy into chemical potential energy.[59] The absorbed energy roughly equates to the difference between the highest occupied (HOMO) and lowest unoccupied molecular orbital (LUMO) of the dye. All processes following this step are dissipative and lead to a reduction in output energy.[59] Excited state lifetimes differ between the various dyes, but generally range between 1 and 10 ns, before decaying radiatively, although thermal, nonradiative relaxation to a lower vibrational state can occur in the femtosecond (fs) range.[68,69] The efficiency of the excitation process is called light-harvesting efficiency η_{lh}

$$\eta_{lh}(\lambda) = 1 - 10^{-A(\lambda)} \tag{2}$$

with the absorbance A, given by Beer-Lambert law[70,71]:

$$A(\lambda) = log\left(\frac{I_0}{I_T}\right) = \varepsilon_\lambda cd \tag{3}$$

where I_0 is the incident light intensity, I_T the transmitted light intensity, ε_λ the wavelength-depended molar absorption coefficient of the dye, c the concentration of the dye and d the thickness of the layer.

2.1.3.2 Injection

DSSCs introduced a novel feature compared to traditional solar cell concepts by separating the tasks of light absorption and charge transport.[36] This concept has since lead to the development of other successful solar cells types, such as perovskite or organic solar cells.[72] Charge separation in DSSCs occurs through injection of the electron from the excited state into the conduction band of the semiconductor.[73] While this process is often indicated in a simplified manner by a diagonal arrow as shown in Figure **1**, it is actually isoenergetic in nature and occurs, according to Marcus-Gerischer theory[74,75], between donor and acceptor states of the same energy. It is therefore highly beneficial for electron injection to ensure a significant energetic overlap between the density of the occupied excited states of the dye and the unoccupied states of the semiconductor through positioning of the excited state levels above E_c (see Figure **3 a**).[76,77]

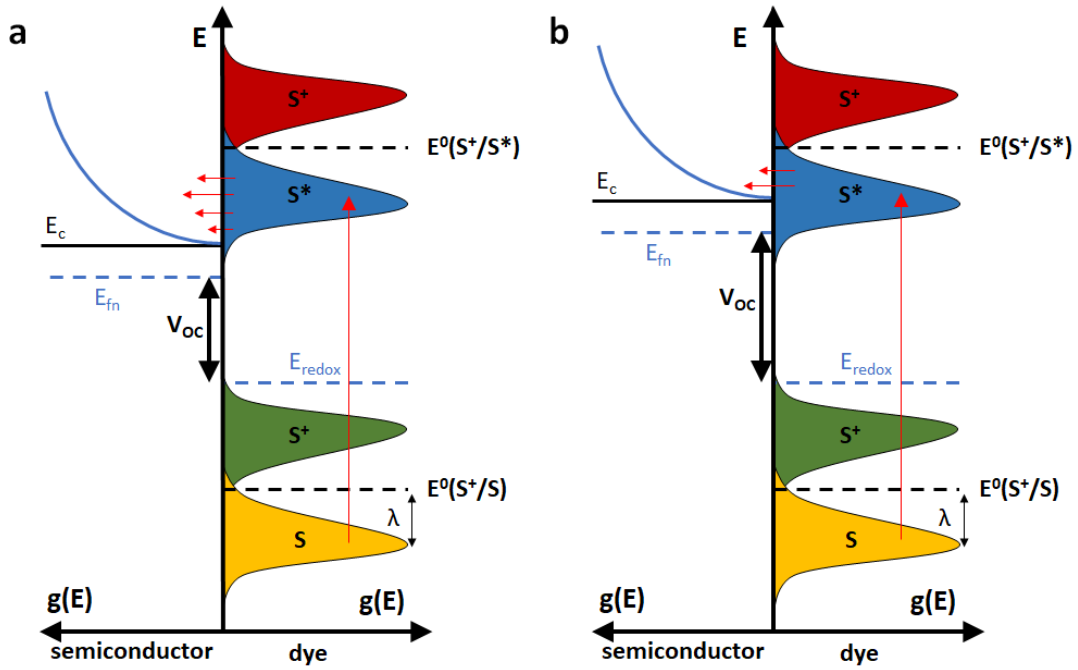

Figure 3. Gerischer diagram of the semiconductor/dye interface in a DSSC. *(**a**) Efficient electron injection can be achieved by having a large overlap between the states of the excited state of the dye S* (blue) and the acceptor states of the semiconductor conduction band. Red arrows show electron excitation in the dye and injection into the semiconductor. (**b**) An upward shift of E_c increases the V_{OC}, but lowers the rate of injection, which can cause J_{SC} to decrease. The maxima of the distribution of occupied and unoccupied states of the dye in the ground and exited state is separated from $E^0(S^+/S)$ and $E^0(S^+/S^*)$ by the reorganization energy λ, respectively. Adapted from [36] and [78] with modifications.*

A decrease of the overlap between the donor and acceptor states through additives to the electrolyte or direct modification of the semiconductor has been shown to be able to slow down electron injection, depending on the dye used (see Figure **3 b**).[68,79] Electron injection is generally ultrafast and occurs in the range of 10^{-13} to 10^{-11} s. A decrease of the injection rate has a diminishing effect on the electron injection efficiency η_{inj}[36]

$$\eta_{inj} = \frac{k_{inj}}{k_{inj} + k_{decay}} \tag{4}$$

with the rate constant for electron injection k_{inj} and the rate constant for radiative and nonradiative decay of the excited dye state k_{decay}. While a shift of E_c will increase the V_{OC}, a decrease in in the electron injection rate can lead to a decrease in η_{inj} and J_{SC}, making optimization of the electrical power output of the solar cell a compromise between the two.[36]

2.1.3.3 Transport and Recombination

Modelling of electron transport in DSSCs is frequently done only in the context of TiO_2 as semiconductor material. Due to the small size of the TiO_2 nanoparticles, low doping density as well as the large dielectric constant of the material, the Debye-length regularly surpasses the particle size, i.e. the electrode is considered free of any built-in fields.[80,81] Electron transport occurs only by diffusion, driven by the electron concentration gradient in the photoanode.[78] This assumption has been shown to not always hold up for alternative semiconductors, such as ZnO, with lower dielectric constants, leading to partially field-driven transport and band bending.[82,83] Cations[84] and additives in the electrolyte[64,84] as well as the oxidized dye[59] screen the semiconductor surface and ensure local charge neutrality, but have also been shown to influence electron diffusion due to electrostatic interactions. (Figure **4**).[85] Furthermore, experiments indicate that transport is significantly influenced by an exponentially decreasing tail of localized trap states below the conduction band.[86,87] The density of trapped electrons n_t in these states is given by

$$n_t = N_t \cdot exp\left(\frac{\alpha_t(E_{fn} - E_c)}{kT}\right) \tag{5}$$

where N_t is the total trap density and α_t is a trap distribution parameter below E_C. The most widely used approach to explain diffusive transport in the context of these trap states is the multi trapping (MT) model.[88] Electrons are assumed to be repeatedly trapped in shallow trap states below E_c, from where they can be thermally detrapped and excited back to the conduction band. This repeated trapping and detrapping process strongly increases the electron transport

times and leads to a reduction in electron mobility compared to single crystals.[89] A direct relation between electron mobility and diffusion in semiconductors is given by the Einstein-Smoluchowski equation.[90] In a quasi-static approximation, an efficient diffusion coefficient D_n is determined

$$D_n = D_0 \left(1 + \frac{\partial n_t}{\partial n_c}\right)^{-1} \approx D_0 \left(\frac{\partial n_t}{\partial n_c}\right)^{-1} \tag{6}$$

with the diffusion coefficient of conduction band electrons D_0. Inserting (1) and (5) into (6) delivers an expression that highlights the dependence of electron diffusion on trap density and distribution as well as the relative position of the quasi-Fermi level[78,91]

$$D_n = D_0 \frac{N_c}{\alpha_t \cdot N_t} \exp\left(\frac{(1-\alpha_t)\cdot\left(E_{fn} - E_c\right)}{kT}\right) \tag{7}$$

Trap states involved in electron transport can be located at the surface, in the bulk or at the grain boundaries between nanoparticles. Avoidance of grain boundaries and increase of crystallinity has been shown to lower the trap density and decrease electron transport times.[92] In addition to shallow traps directly below E_c, deep trap states of 0.5 eV and more below E_c have been attributed to surface defects at the semiconductor/electrolyte interface.[93] These traps do not influence electron transport, but are possible recombination pathways. Recombination of photoinjected electrons from the semiconductor to the oxidized species of the redox electrolyte or the dye is a process that directly competes with electron transport and affects all cell parameters (V_{OC}, J_{SC} and FF) negatively. Due to the direct interaction of semiconductor, dye and electrolyte, recombination presents a widely complex topic that has often been discussed on a macroscopic (design of new dyes[94–96] and electrolytes[97–99]) and microscopic scale (charge-transfer mechanism and pathways[100–102]). A huge number of publications has been dedicated over the years to investigate the underlying mechanism of recombination of specific combinations of components and cell architectures as well as developing methods to suppress and control recombination. Analogous to electron transport, an expression for the effective electron lifetime τ_n, depending on the distribution of trap states in the band gap, can be determined in a quasi-static approximation[78,91]

$$\tau_n = \tau_0 \cdot \alpha_t \frac{N_t}{N_c} exp\left(\frac{(\alpha_t - 1)\cdot\left(E_{fn} - E_c\right)}{kT}\right) \tag{8}$$

with the constant lifetime of electrons in the conduction band τ_0. Electron lifetimes present a central and measurable parameter to study recombination dynamics in DSSCs. However, τ_n determined from (8) will generally be higher than experimentally measured values, since the simple model assumes linear, first order recombination only from the conduction band. A more

realistic description, which includes recombination via surface trap states, can be gained by replacing τ_0 with a characteristic lifetime τ_f that includes contributions from both recombination pathways as well as replacing (α_t - 1) by (α_t - β) with the recombination parameter $\beta < 1$, to accurately describe the often observed sub-linear recombination in DSSCs.[78,103] Both of the equations for the competing transport and recombination process can be combined to describe the diffusion length L_n of electrons being transported through the semiconductor.[104]

$$L_n = \sqrt{D_n \tau_n} \tag{9}$$

By comparing L_n to the respective layer thickness d an expression can be gained for charge-collection efficiency η_{col} at the back contact

$$\eta_{col} = \frac{k_{tr}}{k_{tr} + k_{rec}} = \frac{L_n}{d} \tag{10}$$

with the rate constant for electron transport in the semiconductor k_{tr} and the rate constant for the combined recombination from the conduction and band and surface states k_{rec}.

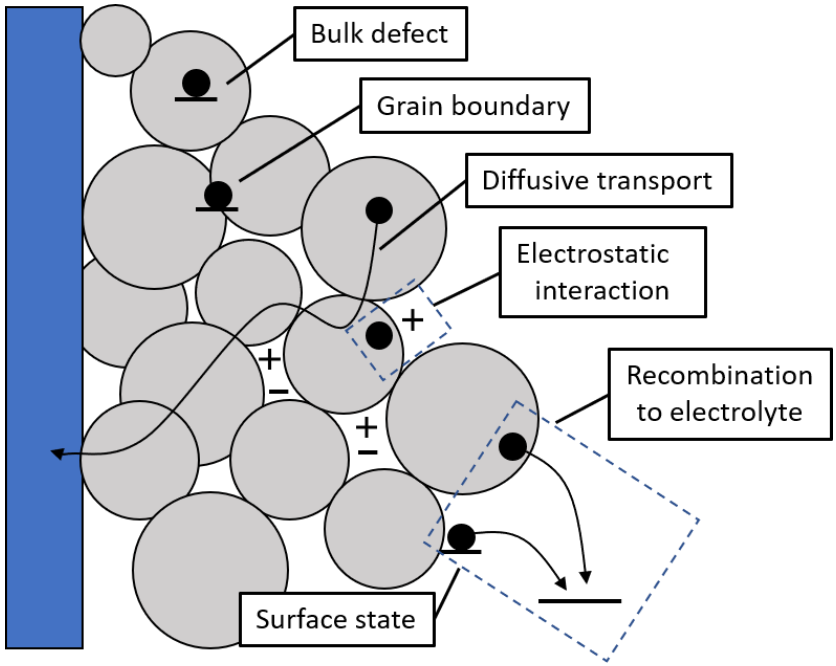

Figure 4. Schematic summary of the transport and recombination processes in a DSSC. *Diffusive transport to the back-contact is slowed down by repeated trapping and detrapping in traps located in the bulk, at grain boundaries and at the surface. Transport can also be affected by electrostatic interactions with cations. Electrons are lost due to recombination with the electrolyte from the conduction band or through surface trap states. Adapted and modified from [36].*

2.1.3.4 Regeneration

Similar to the injection of electrons from the dye to the semiconductor, regeneration of the oxidized dye by charge transfer from the redox electrolyte is described by Marcus-Gerischer

theory and requires overlap between the donor and acceptor states.[36,38,105] Due to the necessary driving forces for regeneration, depending on the reorganization energy λ of the redox couple, dye regeneration is one of the primary loss processes of potential energy in DSSCs.[106,107] The redox couple I^-/I_3^- had been the standard in DSSC devices for over 20 years, partially due to its high regeneration efficiency η_{reg}

$$\eta_{reg} = \frac{k_{reg}}{k_{reg} + k_{rec-d}} \tag{11}$$

with the rate constants for dye regeneration k_{reg} and recombination to the dye $k_{rec\text{-}d}$.[108] However, the formation of an $I_2^{\cdot-}$ radical during the regeneration process strongly increases the driving force of the reaction, leading to energy losses of about 600 mV and overall low V_{OC}.[109,110] While the formation of the radical also strongly slows down the recombination kinetics of iodide[109], its poor thermodynamic performance led to the development of modern Co- and Cu-based redox couples such as $[Co(bpy_3)]^{3+/2+}$ and $[Cu(tmby)_2]^{2+/+}$. Although these provide their own challenges in terms of recombination and diffusion, their small driving force as low as 100 mV needed for a fast regeneration strongly decreases energy losses while regenerating the dye at close to unity yield. [9,14,17]

2.1.3.5 Charge transport and reduction at the counter electrode

Charge transport to the counter electrode is determined mainly by diffusive mass transport of the oxidized redox species as a result of concentration gradients. While hole-hopping from one redox molecule to another has been shown to occur, the effects are limited to mostly Cu-based redox couples[58,107] and (quasi-)solid-state DSSCs[111,112]. Depending on the size of the redox mediator, diffusion inside the porous semiconductor network might be limited and vary from diffusion in the bulk.[113] This has been shown to strongly affect charge transport by Co-based electrolytes, such as the commonly used $[Co(bpy_3)]^{3+/2+}$, where the bulky octahedral ligands lead to slower diffusion and limited photocurrents under high illumination.[114,115] Recent advances in sealing techniques have also eliminated diffusion outside the porous network by directly placing the counter electrode on top of the photoanode, reducing transport times and increasing photocurrents.[116] However, this cell structure up to now has only been realized by using the conductive polymer poly(3,4-ethylene dioxythiophene) (PEDOT) as a catalyst at the counter electrode to avoid shunts. PEDOT has also emerged as an alternative to the highly catalytic but expensive platinum due to its good conductivity and stability, high flexibility, and low cost.[117]

2.2 Magnesium-doped Zinc Oxide

Zinc oxide has accompanied the development of human society for over 4000 years.[118] From its usage as skin treatments in ancient Egypt, through brass production in the middle ages, and as a pigment in watercolors in the 18th century, ZnO presently is mainly used in rubber, ceramic and concrete fabrication.[119,120] Modern science has found a wide variety of potential applications in photovoltaics[121–123], photocatalysis[124–126], optoelectronics[127–129], piezoelectronics[130–132], sensors[133–135] and more, based on its properties as a direct wide band gap semiconductor (E_g = 3.37 eV) with a large exciton binding energy (60 meV).[136,137] Most of these modern applications use ZnO in the form of nanostructures.[118] ZnO can be prepared with relative ease in a vast variety of nanostructures by a wide array of fabrication methods, including sputtering[138], spray pyrolysis[139], sol-gel processes[140], pulsed laser deposition (PLD)[141], atomic layer deposition (ALD)[142] and metal-organic chemical vapor deposition (MOCVD)[143]. Furthermore, significant variation of the ZnO band gap is enabled through cationic substitution with various metals of which Al, Ga, and B are those most excessively used.[144] Doping of ZnO with Mg results in the ternary alloy $Mg_xZn_{1-x}O$ (MZO), which has been shown to exhibit a strongly increased optical band gap depending on the Mg concentration.

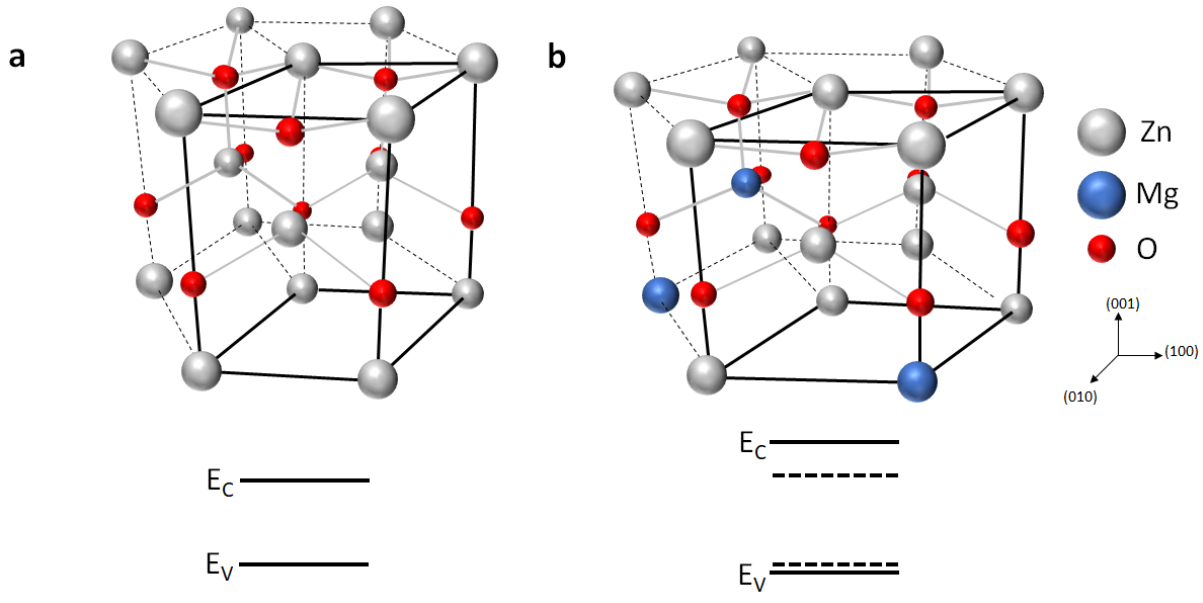

Figure 5. Schematic changes to structural and optical properties of ZnO. *Crystal structure of* **a** *ZnO and* **b** *MZO with their respective conduction band (E_C) and valence band (E_V) edge. The lattice constant in the (100) direction increases and shrinks in the (001) direction after the substitution of Zn with Mg. The shift of E_C is much more pronounced than the one of E_V.*

For Mg concentrations up to 5%, Mg^{2+} ions have been found to incorporate into Zn lattice sites, while higher concentrations can also lead to integration into interstitial sites.[125] However, while very similar in size, slight differences in the ionic radii of Mg^{2+} (0.57 Å) and Zn^{2+} (0.60 Å) ions result in changes to the lattice constants of the crystal structure in a- and c-direction (see Figure **5 a** and **b**), leading to the desired increase of the band gap. This increase is primarily caused by a shift of the conduction band rather than the valance band.[145,146]

$Mg_xZn_{1-x}O$ nanostructures have been prepared nearly identical to pure ZnO through wet-chemical or sol-gel synthesis, PLD, ALD, and MOCVD, with varying levels of Mg-doping. The upper limit for forming MZO without phase separation has been shown to vary greatly between different synthesis methods and can reach as high as x = 0.33 for PLD or x = 0.49 for MOCVD.[147,148] However, MZO layers prepared solely with these techniques are too thin and dense for the application in DSSCs, as they cannot provide the surface area required to reach high efficiencies. For the preparation of MZO nanoparticles through wet-chemical synthesis, a thermodynamic solubility limit of x = 0.05 was found.[149] Precipitation of wurtzite MZO nanoparticles outside this range will include nonequilibrium, compensated defects that affect the material's structural, electrical, and optical properties. Identical to the preparation of ZnO, the vast majority of publications for the preparation of MZO nanoparticles through wet-chemical synthesis propose a reaction pathway through the hydrolyzation of Zn^{2+} and Mg^{2+} ions.[150]

$$x\,Mg^{2+} + 1 - x\,Zn^{2+} + 2\,OH^- \rightarrow Mg_xZn_{1-x}(OH)_2$$
$$Mg_xZn_{1-x}(OH)_2 \overset{\Delta T}{\rightarrow} Mg_xZn_{1-x}O + H_2O \qquad (12)$$

Commonly used precursors for this co-precipitation include Mg- and Zn-acetate, nitrate or chloride, KOH and NaOH. One of the most significant advantages of this reaction pathway for pure ZnO is its low energy cost due to $Zn(OH)_2$ transforming into ZnO at only 70 °C. However, the transformation of $Mg(OH)_2$ to MgO is known to require over 350 °C, leading most publications to calcinate the $MgZn(OH)_2$ intermediate at temperatures around 500 °C, forgoing the aspect of energy conservation.[151] The reported range of successful Mg integration into wurtzite ZnO varies widely, from below 1%[152] through 5%[153], 7.5%[154], 10%[155], 15%[156] up to 17%[157]. Preparation of MZO through the sol-gel method has shown a similar variance in Mg-concentration, but reaching as high as x = 0.3 for the preparation of thin films through spin-coating[158] and x = 0.2 for direct calcination of the gel at 600 °C.[159] Kumar et al. proposed an alternative pathway for wet-chemical synthesis through an oxalate intermediate[160], similar to earlier reports on the preparation of mixed metal oxides.[161–163]

$$x\,Mg^{2+} + 1 - x\,Zn^{2+} + (C_2O_4)^{2-} \cdot\ 2\,H_2O \rightarrow Mg_xZn_{1-x}(C_2O_4) \cdot\ 2\,H_2O \quad (13)$$

$$Mg_xZn_{1-x}(C_2O_4) \cdot\ 2\,H_2O \xrightarrow{\Delta T} Mg_xZn_{1-x}O + 2\,CO_2 + 2\,H_2O$$

Following calcination of the oxalate intermediate, homogenously doped nanoparticles of Mg-concentrations up x = 0.2 could be obtained.

As a special version of MOCVD, ALD enables the preparation of MZO with very high control over film properties such as composition and layer thickness through layer-by-layer growth.[164,165] Liquid precursors, such as Diethylzinc (DEZ) and Bis(ethyl cyclopentadienyl)magnesium ($Mg(EtCp_2)$), are alternatively and sequentially vaporized and react in a self-limiting surface reaction with the functional groups on the substrate surface to form ZnO and MgO layers.[166] Every deposition cycle follows a [metal precursor – purge – H_2O – purge] timing sequence, with the duration of each step being a matter of optimization. Two deposition cycles with varying precursor materials can be combined to form a supercycle to prepare ternary materials such as MZO.[167] The composition of the deposited film can be tuned through the ratio and sequence of the individual deposition cycles. ALD can be used to prepare core-shell structures through the deposition of MZO inside porous thin films and nanoparticulate structures as shown in Publication (II) of this work.[168] The deposited films form conformal layers around the original structure, preserving the morphology of the sample.[169]

2.3 Characterization methods

Sample characterization in this work is divided into characterization of either MZO or full DSSCs. For the characterization of MZO nanoparticles and thin films, the focus lies in analyzing their structural and optical properties. As shown in chapter 2.2, changes to the crystal structure due to Mg-integration result in the desired changes in the band structure. X-ray diffraction (XRD) is, therefore, the perfect method to confirm successful integration of Mg^{2+} into the ZnO crystal lattice and analyze these changes in detail. Optical absorption spectroscopy allows for a quantified study of the changes to the optical band gap due to Mg doping, making it highly relevant for this work. Characterization of DSSCs with MZO-based photoanodes focuses on determining the photovoltaic characteristics and analyzing charge-transfer processes inside the cells. An established toolbox including current-voltage (*I-V*) and external quantum efficiency (EQE) measurements, electrochemical impedance spectroscopy (EIS), and intensity-modulated photovoltage (IMVS) and photocurrent spectroscopy (IMPS) were used for this purpose.[170]

2.3.2.1 Characterization of MZO nanoparticles and thin films

Periodically arranged atoms with long-range order can coherently scatter incoming x-ray photons, resulting in constructive or destructive interference. The resulting characteristic x-ray diffraction (XRD) pattern can be predicted for each crystallographic unit cell, depending on the structure and atom, by the structure factor F_{hkl}

$$F_{hkl} = \sum_{n=1}^{N} f_n \exp[2\pi i(hx_n + ky_n + lz_n)] \tag{14}$$

with the respective atomic form factors f_i, the fractional coordinates in the unit cell x_n, y_n, z_n, and the Miller indices *hkl* of the reflection under consideration.[171] For MZO in a wurtzite crystal lattice, this results in

$$F_{hkl} = \begin{cases} 4\left(f_{Mg/Zn} + f_O\right), & h + k + l = 4N \\ 4\left(f_{Mg/Zn} \pm i f_O\right), & h + k + l = 2N + 1 \\ 4\left(f_{Mg/Zn} - f_O\right), & h + k + l = 4N + 2 \end{cases} \tag{15}$$

with an integer *N*. Consequently, only reflections with *h*, *k*, and *l* all even or all odd show constructive interference, while others will appear with diminished intensity.[172] Constructive interference will only occur at characteristic angles 2θ at which incoming X-rays are scattered at parallel planes of atoms. For samples measured in the Bragg-Brentano geometry, θ can be determined from Bragg´s-law:

$$\lambda = 2d_{hkl} \cdot sin\theta \tag{16}$$

with the wavelength λ of the incoming x-rays and the interatomic distance between parallel planes d_{hkl}.[171,173] This interplanar spacing further depends on the lattice constants of the unit cell, which for hexagonal structures is given by

$$\frac{1}{d_{hkl}^2} = \frac{4}{3}\frac{h^2 + hk + k^2}{a^2} + \frac{l^2}{c^2} \tag{17}$$

with the lattice constants *a* and *c*.[171] Thus, changes to the lattice constants will also result in shifts of the 2θ position of the respective *hkl* reflex. The information gained from XRD patterns can be used to determine the phase composition of a given sample, unit lattice cell parameters, and, if the peak shape is considered, the crystallite size and defect density.

UV-vis spectroscopy is used to study the interaction of light from the ultraviolet (UV) and visible (vis) parts of the electromagnetic spectrum with matter.[174] It is based on the Bohr-Einstein frequency relationship to connect discrete energy states *E* of a probed material with the frequency *v* or wavelength λ of electromagnetic radiation:

$$\Delta E = E_2 - E_1 = h\upsilon = \frac{hc}{\lambda} \tag{18}$$

with Planck's constant *h* and the speed of light *c*.[175] Incoming photons can excite an electron in the probed material to a higher electronic energy level if their energy matches the energy difference of an available transition.[176] In semiconductors, this transition usually describes the excitation of an electron from the valance to the conduction band. The wavelength-dependent absorbance *A* of a material is determined by the ratio of transmitted to absorbed and scattered light and described by Beer-Lambert law (see Eq. 3). However, the empirical linear dependence of the absorbance on the concentration of the absorber only applies to very low concentrations (below 10^{-2} mol l^{-1}) making Beer-Lambert law only applicable for diluted solutions, gases or thin layers.[175,177] Additionally, the customary form of Beer-Lambert law in Eq. 3 is defined to exclude surface effects such as reflection losses and neglectable scattering and luminescence in the sample.[178] If surface effects cannot be excluded, for example by use of a cuvette, the absorptance α has to be used to describe the ratio of absorbed incident light[178]:

$$\tau + \alpha + \rho = 1$$
$$\alpha = \frac{I_{abs}}{I_0} \tag{19}$$

with the transmission τ, the reflectance ρ and the intensity of the absorbed incident light I_{abs}.

Diffuse reflection spectroscopy presents an alternative way to study materials that fall outside the parameters of Beer-Lambert law, such as nanoparticles. Diffuse reflection is a blanket term that is influenced by the reflection, refraction, diffraction, and absorption of light by randomly oriented particles.[179] Sufficiently thick powder samples are placed on a sample holder and the reflected light is collected inside an integrating sphere.[180] The resulting spectra are analyzed according to the Kubelka-Munk function $F(R_\infty)$:

$$F(R_\infty) = \frac{(1 - R_\infty)^2}{2R_\infty} = \frac{K}{S} \tag{20}$$

with the absolute reflectance R_∞, the absorption coefficient *K*, and the scattering coefficient *S*. The band gap energy E_g of semiconductors can be determined from optical spectroscopy measurements through a Tauc plot:[181,182]

$$(\alpha_i \cdot h\nu)^{\frac{1}{\gamma}} = C\ (h\nu - E_g) \tag{21}$$

with the absorption coefficient α_i, a constant *C*, and the factor γ, which is ½ for direct and 2 for indirect transitions. If UV-vis spectroscopy was used, the absorption coefficient α_i can be determined from the Absorbance *A* and the film thickness *d*. If only samples with the same film

thickness are compared, α_i can be replaced by *A*. If diffuse reflection spectroscopy was used to measure the optical spectrum, α has to be replaced by the Kubelka-Munk function:[178,183]

$$\alpha_i = \varepsilon_\lambda \cdot c = 2.303 \cdot \frac{A}{d}$$
$$(A \cdot h\nu)^{\frac{1}{\gamma}} = C\left(h\nu - E_g\right) \quad (22)$$
$$(F(R_\infty) \cdot h\nu)^{\frac{1}{\gamma}} = C\,(h\nu - E_g)$$

2.3.2.2 Characterization of DSSCs with MZO-based photoanodes

Current-voltage (*I-V*) curves are the most fundamental part of a toolbox containing complementary experimental methods used to gain detailed understanding of the internal processes of a DSSC.[184] Under standard solar illumination (AM1.5G), a linear voltage sweep is performed while recording the current response. The important solar cell performance parameters short-circuit current J_{SC} and open-circuit voltage V_{OC} are obtained at the intersections of the measured curve with the current-axis (V = 0) and the voltage-axis (J = 0), respectively. The fill factor FF is used to describe the ideality of the measured curve. In addition to losses across the semiconductor/electrolyte interface, it includes losses due to series resistances of the TCO substrate as well as ohmic and diffusion resistances of the electrolyte and semiconductor.[185]

$$FF = \frac{P_{max}}{J_{SC} \cdot V_{OC}} = \frac{J_{MPP} \cdot V_{MPP}}{J_{SC} \cdot V_{OC}} \quad (23)$$

with the maximum power P_{max} determined from the current J_{MPP} and voltage V_{MPP} at the maximum power point. Together with J_{SC} and V_{OC}, the fill factor can be used to determine the power conversion efficiency η of a solar cell:

$$\eta = \frac{P_{max}}{P_0} = \frac{J_{SC} \cdot V_{OC} \cdot FF}{P_0} \quad (24)$$

with the power of the incoming light P_0 (100 W/m^2 for AM1.5G).[184]

Measurements of the external quantum efficiency EQE can be used to further probe the current response of the cell. EQE reflects the combined efficiency of the charge-transfer processes described in chapter 2.1.3 and includes the wavelength-dependent light-harvesting efficiency η_{lh} (Eq. 2), the injection efficiency η_{inj} (Eq. 4), the charge-collection efficiency η_{col} (Eq. 10), and the regeneration efficiency η_{reg} (Eq. 11):[184]

$$EQE = \eta_{lh}\eta_{inj}\eta_{col}\eta_{reg} \quad (25)$$

EQE is measured under short-circuit conditions and monochromatic illumination. In the case that all absorptions bands of the dye equally contribute to the light-harvesting efficiency, EQE will largely match the absorptions spectrum. If measured across the entire solar spectrum, a theoretical J_{SC} can be determined and compared to the one gained from *I-V* curves:

$$J_{SC} = q \cdot \int_{\lambda_{min}}^{\lambda_{max}} EQE(\lambda) \cdot \Phi(\lambda) d\lambda \tag{26}$$

with the spectral photon flux density $\Phi(\lambda)$.[103] Furthermore, a fit of the measured *EQE* curve with respective optical absorption data can be used to determine the diffusion length L_n of electrons in the semiconductor layer with a thickness d

$$EQE = \frac{L\alpha}{1 + L\alpha} \tag{27}$$

under the assumption that $L_n < d$.[186]

Electrochemical impedance spectroscopy (EIS) is a cornerstone of the DSSC toolbox, giving access to the fundamental charge-transfer processes described in chapter 2.1.3. Under constant illumination, a small amplitude, harmonic voltage perturbation is superimposed on a constant bias over a wide frequency range (MHz to mHz), resulting in a slight variation of E_{fn}.[185] Amplitude and phase shift of the resulting current is recorded as a function of frequency and the corresponding impedance Z is displayed in the form of a Nyquist plot[78,187]

$$Z(\omega) = \frac{V(\omega)}{I(\omega)} = |Z|e^{i\Phi} = Z' + iZ'' \tag{28}$$

with the phase angle Φ, the real part Z' and the imaginary part Z'' of the impedance. Charge-transfer processes across interfaces, such as recombination across the semiconductor/electrolyte, charge-transfer across the electrolyte/counter-electrode interface and electron diffusion in the electrolyte and semiconductor, result in semicircles in the Nyquist plot. Simple parallel combinations of a resistor R and a capacitor C can be used to model each semicircle, with all components combined forming the equivalent electrical circuit to fit the measured EIS spectrum. All semicircles are shifted on the Z´-axis by the value of the series resistance R_S, which depends on the resistance of the conductively coated glass substrate.[185]

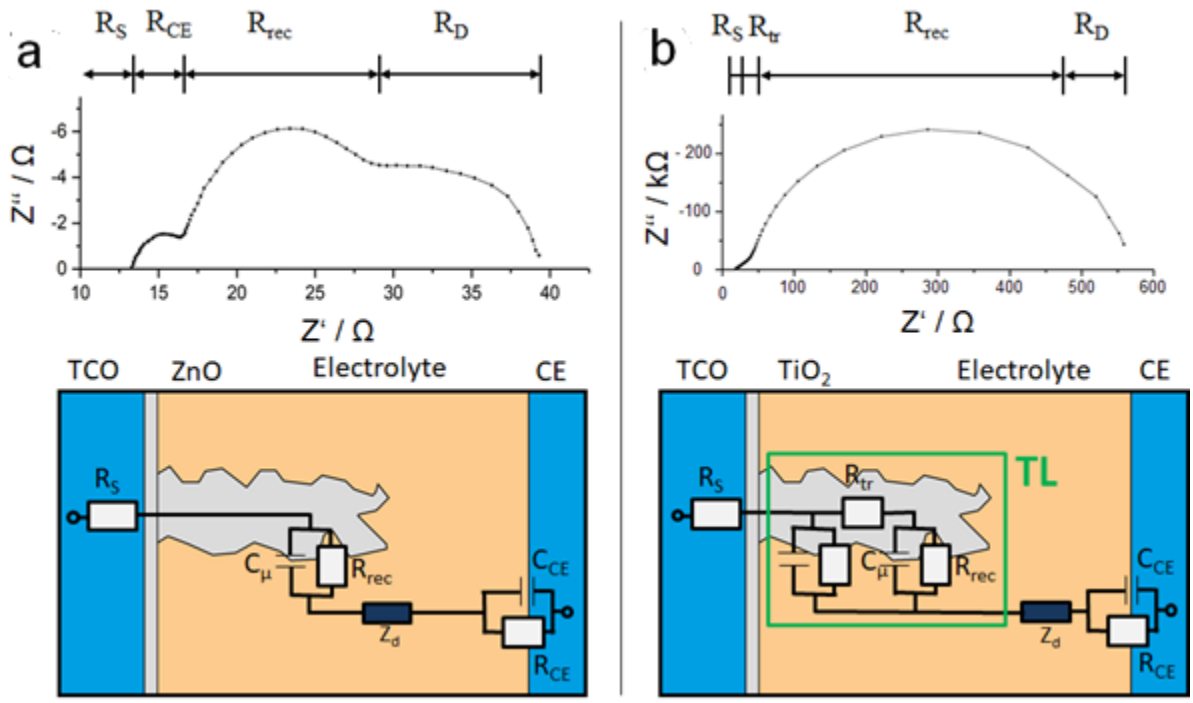

Figure 6. EIS analysis of ZnO- and TiO_2-based DSSCs. a *EIS spectrum in form of a Nyquist plot of a ZnO-based DSSC with a $[Co(bpy)_3]^{2/3+}$ and the respective equivalent electrical circuit. Three semicircles representing charge-transfer processes can be seen.* ***b*** *EIS spectrum and equivalent electrical circuit of a TiO_2-based DSSC. At low Z', a slope of 1 is indicative of a transport resistance. Together with R_{rec} and C_μ, R_{tr} forms the transmission line TL. R_{rec} and R_D overlap and R_{CE} cannot be seen due to very small values.*

The first semicircle at high frequencies (low *Z*') can be attributed to the counter-electrode and is described by the charge-transfer resistance R_{CE} and the capacitance C_{CE}. Since the basic notion of a parallel plate capacitor does not hold for DSSC photoanodes at low potentials, the electrochemical capacitance of the second semicircle representing the charge transfer between the semiconductor and the electrolyte is described by a chemical capacitance C_μ.[188] In DSSCs, C_μ is dominated by electrons in localized trap states in the band gap for $E_{fn} < E_C$ [188,189]:

$$C_\mu = C_\mu^{trap} = q^2 \cdot g(E_{fn}) = q^2 \frac{\alpha \cdot n_t}{k_B T} \qquad (29)$$

with the electron charge q, the exponential density of states distribution at the Fermi-level $g(E_{fn})$, the Boltzmann constant k_B and the temperature T.[188] The recombination resistance R_{rec} describes the charge-transfer from the semiconductor to the electrolyte[189]:

$$R_{rec} = \frac{1}{q^2} \cdot \left(\frac{\delta U_n}{\delta E_{fn}} \right)^{-1} \qquad (30)$$

with the rate of recombination U_n. The product of C_μ and R_{rec} describes the effective electron lifetime τ_n.[185]

$$\tau_n = R_{rec} \cdot C_\mu \tag{31}$$

In the case that τ_n is much higher than the electron transport time τ_{tr} to the substrate, as is often the case for ZnO, electron transport can be neglected in the equivalent electrical circuit. If $\tau_n \gg \tau_{tr}$ is not fulfilled, an increase at a 45° angle (slope of 1) can be observed in the semicircle describing the semiconductor/electrolyte interface, which can be described by a transport resistance R_{tr}.[185]

$$\tau_{tr} = R_{tr} \cdot C_\mu \tag{32}$$

The third semicircle is at low frequencies (high Z') and is attributed to charge transport through diffusion of the redox species. It is described by a so-called Warburg-short element Z_W, which includes the diffusion coefficient and the concentration of the oxidized redox species.[190] Depending on the electrolyte used, this semicircle might be very small (i.e. I^-/I_3^-) or clearly visible (i.e. $[Co(bpy_3]^{2/3+}$).

Intensity-modulated photocurrent and photovoltage spectroscopy (IMPS and IMVS) present additional ways to gain valuable insight into the charge-transfer processes in DSSCs. Analogous to EIS, IMPS and IMVS measurements are performed by applying a sinusoidal, small-amplitude signal to the incident light intensity while recording the dynamic response as a function of the frequency.[191] For IMPS, the amplitude of the phase-shifted AC current response $\hat{J}$ is measured under potentiostatic control and linked to the amplitude of the modulated light intensity $\hat{\phi}$ by the transfer function φ_{IMPS}. The same applies to IMVS with the AC voltage response $\hat{V}$ measured under galvanostatic control:[192,193]

$$\begin{aligned} \phi_{IMPS} &= \frac{\hat{J}}{q\hat{\phi}} \\ \phi_{IMVS} &= \frac{-\hat{V}}{q\hat{\phi}} \end{aligned} \tag{33}$$

A Nyquist plot of the respective transfer functions will result in a single semicircle in the fourth quadrant. The frequency ω_{max} at which the imaginary part $-i\varphi_{IMPS/IMVS}$ reaches its maximum has been shown to correspond to the electron transport time τ_{tr} or the effective electron lifetime τ_n, respectively. [194,195]

$$\begin{aligned} \tau_{tr} &= \varpi_{max,IMPS}^{-1} \\ \tau_n &= \varpi_{max,IMVS}^{-1} \end{aligned} \tag{34}$$

IMPS and IMVS measurements are performed at varying light intensities, resulting in different values for τ_{tr} and τ_n due to changes in the rate of electron injection.[194] If measured under

comparable conditions, the time constants determined from IMVS and IMPS can be compared to those obtained from EIS (see Eq. 31 and Eq. 32).

2.4 Experimental Section

This chapter summarizes experimental details for studies performed leading up to Publication 1 and 2 as well as efforts to establish screen-printed photoanodes and improve sample geometry and solar cell preparation. All the actions described below were performed by me, if not indicated otherwise. Experimental details directly related to Publication (I) and (II) are mentioned in the respective publications.

2.4.1 Preparation of Screen-printed Photoanodes

Prior to this work, photoanodes in the laboratories of the Schlettwein group were primarily prepared by electrodeposition of ZnO, sometimes compared to doctor-bladed films. The infrastructure and expertise to prepare photoanodes by screen-printing was acquired entirely throughout this project. ZnO and MZO nanoparticles were prepared by coprecipitation (Publication (I)) or acquired commercially (Publication (II)). Screen-printing pastes were prepared with an optimized composition of 7 wt. % nanoparticles, 5 wt. % deionized water, 3 wt. % ethyl cellulose (Aldrich), 25 wt. % terpinol (Roth) and 60 wt. % ethanol (Roth). After combining all of the components, the mixture was stirred vigorously on a magnetic stirrer for 5 min. Afterwards, the container holding the paste was suspended in a water bath for cooling and sonicated with an ultrasonic horn for 5 min. The combined magnetic stirring and ultrasonication treatment was repeated 3 times each, before the open container was transferred onto a platform shaker (Rotamax 120) for 2 days to reduce the ethanol content and increase viscosity. Attempts to shorten this time by reducing the ethanol content in a rotary evaporator remained unsuccessful due to the viscosity and the overall low amount (< 2g) of the paste after evaporation. Direct heat treatment of the container at 70 °C resulted in clumping of the mixture. After 2 days on the platform shaker, highly viscous and homogenous pastes could be obtained. Very small amounts of paste were deposited on the screen-printer (Zhuhai Kaivo) close to the template and printed onto FTO-coated glass substrates (Zhuhai Kaivo). The respective templates were custom designed with the shape and size of the photoanodes and transferred onto empty screens (Siebdruckversand) in cooperation with Silvia Schmandt. A muffle furnace (CWF 1100, Carbolite Gero) was acquired to anneal the screen-printed samples at 420 °C with a heating rate of 10 °C/min. The furnace enabled slower heating and cooling of the samples, as well as a lower temperature gradient resulting in fewer cracks in the samples in comparison to a heating plate that was used in first attempts. Calibration measurements were performed to

study the temperature gradient in the oven and a custom sample holder was designed and commissioned from the precision mechanics workshop of the physics department of JLU Gießen, on which the samples were held during the annealing process.

2.4.2 Optimization of cell geometry and solar cell preparation

Due to limitations of the sample holder during electrodeposition, the established cell geometry prior to this work was based on FTO-coated glass substrates with dimensions of 3 x 2.5 cm for both working and counter electrodes (Figure **7 a**). A 2.7 x 2.5 cm thermoplastic sealing film made of Surlyn® (Solaronix) separated the electrodes. The contact area between both electrodes was covered to avoid short-circuits. An additional 1 x 1 cm piece of melting foil was used to cover the holes through which the electrolyte was filled into the cell. A new cell geometry was designed for DSSCs using screen-printed photoanodes (Figure **7 b**). The area of both electrodes could be reduced to only 1.5 x 1 cm. Only a small circle of Surlyn® with a diameter of 9 mm was prepared using a pritchel. A smaller circle with a diameter of 7 mm was punched out from the middle, leaving only a thin ring to connect both electrodes. Instead of closing the holes in the counter-electrode with another slip of melting foil, a UV curing glue (ThreeBond 3035B) was introduced to cover the holes and subsequently cured under UV light for 30 min.

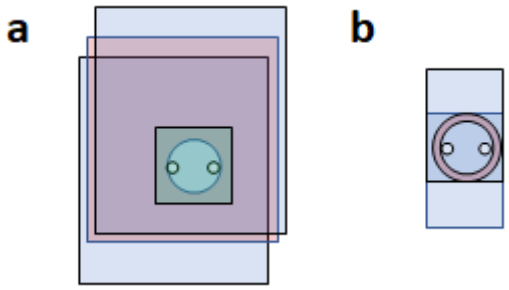

Figure 7. Proportional schematic highlighting the differences between the old (a) and the updated cell geometry (b). *Blue rectangles represent the area of the FTO-coated glass substrates, red areas represent the thermoplastic sealing foil between the two electrodes and green the area of the sealing foil used to close the cell on top.*

An analysis of the costs to fabricate a single DSSC based on the old and the newly designed cell geometry (Table **1**) revealed a reduction in cost of 90%, dropping costs per sample from 13.27 € to 1.29 € (disregarding energy costs).

Table 1. *Analysis of the difference in costs to fabricate a single DSSC prior to this work and using the newly designed cell geometry. The area of Surlyn® includes waste which could not be used further. Cost of material per cm^2 calculated from invoices of the materials.*

	Old cell geometry	New cell geometry
Area FTO	15 cm^2	3 cm^2
Area Surlyn®	7.75 cm^2	0.64 cm^2
Cost FTO at 0.11€/cm^2	1.65 €	0.33 €
Cost Surlyn® at 1.5€/cm^2	11.62 €	0.96 €
Cost per sample	13.27 €	1.29 €

Costs per cm^2 were calculated from the actual invoices of the respective materials including shipping fees, import tax, and bulk discount. The majority of the cost reduction could be achieved through the significant decrease in sealing foil used in the cells. Despite some of the area between both electrodes remaining uncovered, no increase in short-circuited samples was detected. The UV curing glue was acquired as a sample at no cost, courtesy of ThreeBond. Due to the meager amount of glue needed for each DSSC, the sample contained enough glue for hundreds of cells. In addition to the UV sealing glue, a heat press (Graveda) was acquired to optimize solar cell preparation. In contrast to the previously used soldering iron, the heat press can apply pressure and temperature significantly more homogenously across the whole sample while melting the sealing foil. This resulted in fewer cases of leakage of the electrolyte and higher reproducibility of samples.

2.4.3 Experimental details for work leading up to Publication (I)

This section describes the experimental details for the studies performed leading up to Publication (I) in chapter 3.1.2. All of the chemicals mentioned were purchased from Sigma-Aldrich and used without further purification, if not indicated otherwise. For the preparation of nanoparticles through a hydroxide intermediate, ZnO and MZO nanoparticles were prepared from Zn- and Mg-nitrate and -acetate precursors. Metal precursors were dissolved in water and an aqueous solution of KOH was dropwise added under constant stirring until 0.45 M was reached. The concentration of metal ions was set to 0.3 M after adding KOH. The combined solution was put into pressure-withstanding reaction tubes and treated in a microwave reactor

(StartD, Milestone S.r.L) for 30 min at 150 °C. The resulting precipitate was washed with water and ethanol three times and dried at 100 °C overnight. Nanoparticles prepared through the alternative oxalate intermediate were synthesized as described in Publication (I). XRD measurements of the nanoparticles were performed (Ultima III XRD, Rigaku) before and after calcination at 500 °C for 2h. Diffuse reflection spectroscopy (Solid-Spec 3700, Shimadzu) was performed on all nanoparticles after calcination. Combined thermogravimetric and mass spectroscopy (TGA MS) measurements (STA 409 CD, Netzsch) were performed by Alexander Sedykh in the group of Prof. Müller-Buschbaum of the JLU Gießen.

3. Results and Discussion

The scientific developments observed during this work have resulted in the publication of two peer-reviews papers in scientific journals. However, some achievements leading up to these publications were omitted due to length constraints and will be discussed below to provide further context. The main results of both papers will be summarized and discussed in the larger context of this thesis.

3.1 Publication (I): Influence of Mg-Doping on the characteristics of ZnO photoanodes in dye-sensitized solar cells

3.1.1 Work leading to Publication (I)

Preceding the results on the preparation of MZO presented in Publication (I) were a number of attempts to prepare MZO through the hydroxide intermediate (see chapter 2.2) since this was the primary reaction pathway described in the literature. Despite following the instructions given in the literature and the overall simplicity of the reaction, the reported results of successful MZO preparation with Mg concentrations above the known solubility limit of 5% could not be reproduced. After calcination of the $MgZn(OH)_2$ intermediate at 500 °C, an increase of the optical band gap could be observed in the Tauc plot of the optical absorption spectra (see Figure **8 a**), that does not increase for Mg-concentrations above 5%.

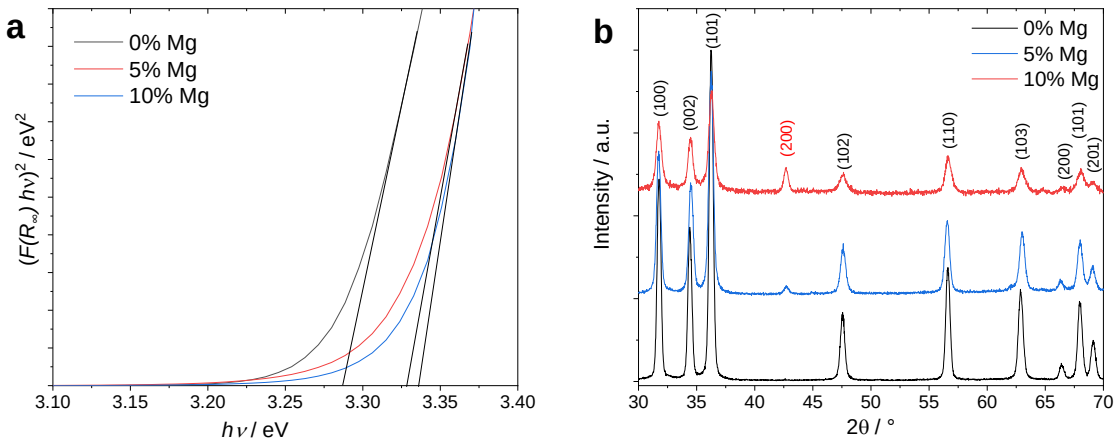

Figure 8. Analysis of MZO prepared through hydroxide intermediate. a *Tauc-Plot of the optical absorption spectra and fits to the linear part of MZO nanoparticles prepared through a hydroxide intermediate with different Mg-concentrations.* ***b*** *XRD of MZO nanoparticles prepared through a hydroxide intermediate with varying Mg-concentrations. The typical ZnO wurtzite reflexes are indexed in black color, while the (200) reflex of cubic MgO is indexed in red.*

Similarly, an identical shift of the (100) and (002) reflexes (not shown in detail) for the samples containing 5% and 10% indicates that similar amounts of Mg^{2+} were integrated into the ZnO wurtzite lattice. However, the emergence of a new reflex for the samples containing Mg strongly indicates the presence of an undesired cubic MgO phase (see Figure **8 b**). Furthermore, no discernable difference could be found between MZO nanoparticles prepared from different precursors, showing that the counter ion does not influence on Mg integration (see Figure **9**). Following reports of Mg diffusion into ZnO at higher temperatures[196–199], MZO nanoparticles containing 20% Mg were characterized after drying at 100 °C and calcination at 1000 °C. Despite the presence of Mg in the precursor solution, UV-vis measurements (Figure **9 a**) revealed that the optical band gap was identical to that of pure ZnO (Figure **8 a**) after drying at 100 °C. XRD measurements further showed the presence of ZnO, already transformed from $Zn(OH)_2$, as well as reflexes characteristic for $Mg(OH)_2$, dispelling the theory of a $MgZn(OH)_2$ intermediate for Mg concentrations above 5% (Figure **9 b**).[150] After calcination at 1000 °C, the MZO nanoparticles exhibited an increased optical band gap comparable to that shown for MZO containing 5% or 10% Mg (Figure **9 a**). Furthermore, $Mg(OH)_2$ transformed into cubic MgO instead of diffusing into the MZO.

Additional attempts to prepare MZO included the dissolution and recrystallization of a $MgAc_2/ZnAc_2$ mixture in water and ZnO/MgO mixture in acetic acid as well as mixing of $MgAc_2/ZnAc_2$ in a mortar, and were all followed by calcination at 1000 °C and resulted in surprisingly similar outcomes as those shown in Figure **9**.

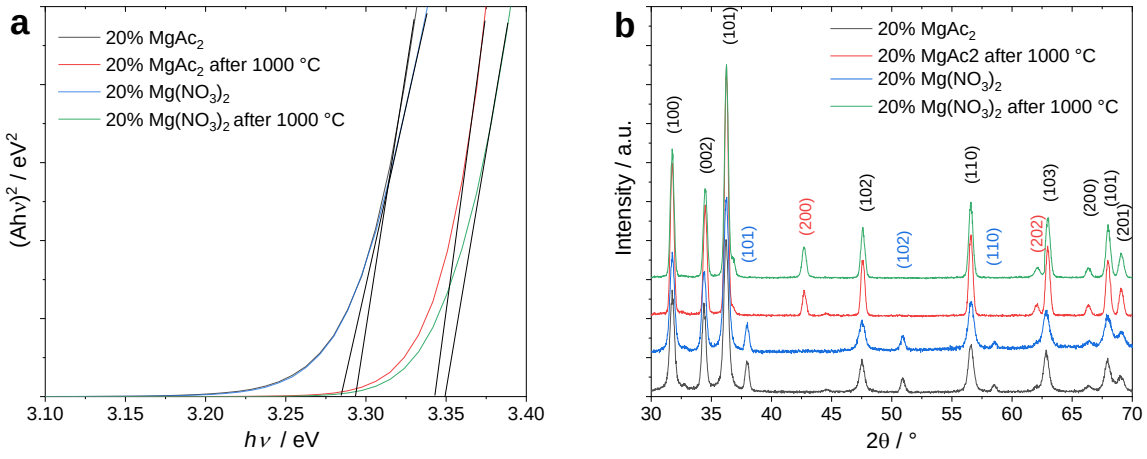

Figure 9. Effects of high temperature on Mg integration. a *Tauc-plot of the optical absorption spectra of MZO nanoparticles containing 20% Mg prepared from different precursors after drying at 100 °C and after calcination at 1000 °C.* ***b*** *Respective XRD of the same MZO nanoparticles. ZnO wurtzite reflexes are indexed in black, cubic MgO reflexes in red, and $Mg(OH)_2$ reflexes in blue.*

Compared to the reaction pathway through a hydroxide or acetate intermediate, the alternative pathway through the oxalate intermediate $MgZn(C_2O_4) \cdot 2H_2O$ proved immediately successful.[160] The XRD of the intermediate after drying at 100 °C is shown in Figure **10 a**. While the intensity of some of the reflexes changed upon the addition of Mg, no new reflexes could be found. This indicates that, in contrast to the hydroxide approach, Mg was truly integrated into the Zn oxalate network instead of appearing as a separate phase, resulting in the successful integration of Mg into the ZnO wurtzite structure after calcination at 500 °C. Up to 20% of Mg was successfully integrated into the ZnO lattice without the appearance of additional phases (see Figure **10 b**), making this approach the method of choice for Publication (I). Surprisingly, some of the results shown in Figure **10 a** heavily diverge from the results presented by Kumar et al.[160], who originally proposed this reaction pathway. In contrast to the XRD of $Zn(C_2O_4) \cdot 2H_2O$ shown in Figure **10 a** (black line), their intermediate exclusively exhibited the characteristic reflexes of the ZnO wurtzite structure. This led them to identify the additional peaks, which appeared with the addition of Mg, as a separate $Mg(C_2O_4) \cdot 2H_2O$ phase instead of a homogenously doped intermediate, as shown here.

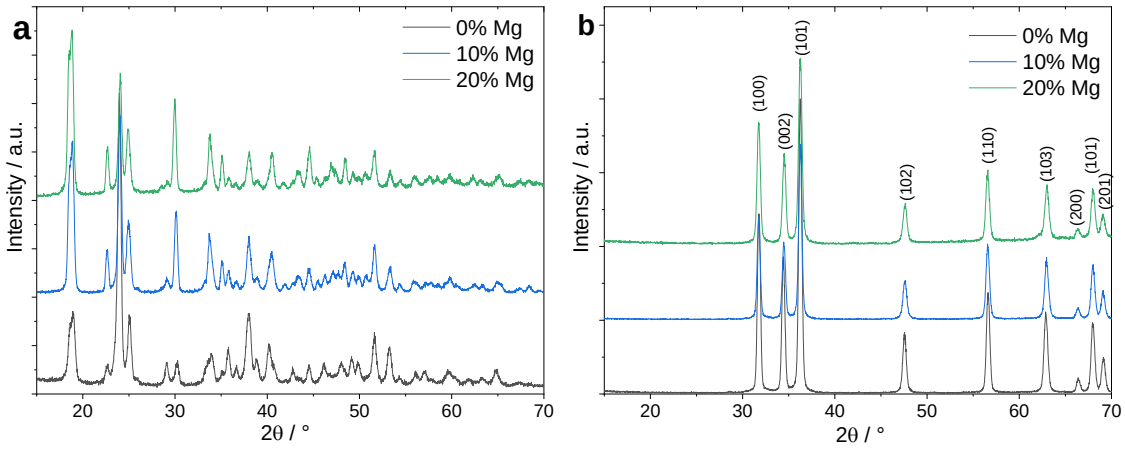

Figure 10. Structural analysis of MZO prepared through oxalate intermediate. a *XRD of the $MgZn(C_2O_4) \cdot 2H_2O$ intermediate with varying Mg-concentration after drying at 100 °C. No additional reflexes can be found after addition of Mg to the precursor solution.* ***b*** *XRD of the same samples after calcination at 500 °C. Oxalate intermediate was fully converted to MZO. No additional phases can be detected even for high Mg concentrations.*

Furthermore, combined thermogravimetric analysis and mass spectrometry (TGA MS) were performed on the samples shown in Figure **10**. A sample containing only pure $Zn(C_2O_4) \cdot 2H_2O$ (Figure **11 a**) as well as the sample containing 20% Mg (Figure **11 b**) showed nearly identical results. MS helped to identify the decomposition steps at 280 – 300 °C as H_2O (m/z = 18) and 380 – 420 °C as CO_2 (m/z = 44), respectively, in agreement with prior reports on the thermal decomposition of zinc oxalate.[200,201] This further proves that an intermediate only containing a

single, homogeneously doped phase was formed and later converted into homogeneously doped MZO.

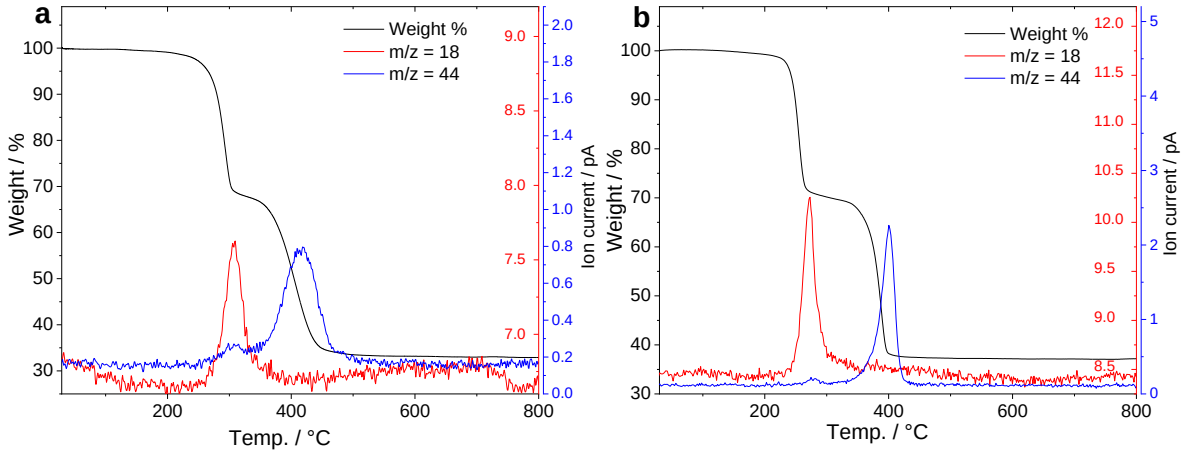

Figure 11. TGA MS analysis of oxalate intermediates. *Combined thermogravimetric analysis and mass spectrometry (TGA MS) for the calcination of a $Zn(C_2O_4) \cdot 2H_2O$ and $Mg_{0.2}Zn_{0.8}(C_2O_4) \cdot 2H_2O$. Two distinct decomposition steps related to the removal of H_2O (m/z =18) and CO_2 (m/z = 44) can be observed.*

These results are in stark contrast to the results of thermogravimetric analysis (TGA) by Kumar et al.[160], since their intermediate showed no weight loss at all for the pure ZnO sample, followed by strongly increasing weight loss with increasing Mg-concentration, identified as the decomposition of $Mg(C_2O_4) \cdot 2H_2O$ to MgO. Overall, this leads to the impression that their samples might have been exposed to significant heat before XRD and TGA measurements were performed. Further, perfect diffusion of MgO into ZnO is assumed in their publication at temperatures around 500 °C, which, as shown in Figure **9**, could not be confirmed in my study. The results in Figures **10** and **11** show the far more likely pathway of a homogenously doped intermediate which consists of only a single phase and is completely converted into MZO through calcination.

Earlier experiments in cooperation with Raffael Ruess highlighted the diverging reaction of modern Co-based electrolytes and the established I_3^-/I^- redox electrolyte[22] on ZnO surfaces as well as mass transport problems related to the much bigger size of Co-complexes.[113] High recombination rates and diffusion limited currents prevented the Co-based electrolytes from improving the cells to the same degree as shown for TiO_2 compared to iodide-based electrolytes. In addition, diffusion-related features in the EIS spectra, which are only visible in cells containing Co-based electrolytes, overlap with the features related to recombination, significantly increasing the difficulty of a detailed analysis. Since the study of recombination-

related electron transfer kinetics and pathways was of great interest to this study, the established I_3^-/I^- redox electrolyte was chosen.

3.1.2 Context of Publication (I)

Publication (I) contains the combined findings on the preparation of Mg-doped ZnO photoanodes and their influence on the performance of DSSCs.[202] Sample preparation and characterization for the wet-chemical synthesis of MZO nanoparticles was performed solely by me, mainly in the laboratories of Prof. Tsukasa Yoshida at the campus of Yamagata University in Yonezawa, Japan. A prior report about the use of MZO in DSSCs relied on a drop-casted sol-gel approach for the preparation of photoanodes[32], making Publication (I) the first to present MZO-based photoanodes in the traditional, nanoparticulate structure. Fabrication of photoanodes and DSSCs, as well as any related steps, were performed by me. Photoelectrochemical measurements on DSSCs were performed by me to study the effects of the Mg-doping on solar cell characteristics and the charge transfer processes inside the cell in particular, while Nico Hofeditz performed the time-resolved photoluminescence (TRPL) measurements in the group of Prof. Heimbrodt at Philipps-University of Marburg. While previous reports of MZO in photovoltaic applications mainly focused on its influence on electron transport[203,204] or recombination[32], Publication (I) considered both of these aspects.

3.1.3 Publication (I)

PCCP

ROYAL SOCIETY OF CHEMISTRY

PAPER

View Article Online
View Journal | View Issue

Cite this: *Phys. Chem. Chem. Phys.*, 2021, **23**, 8393

Influence of Mg-doping on the characteristics of ZnO photoanodes in dye-sensitized solar cells†

Andreas Ringleb,[a] Raffael Ruess,[b] Nico Hofeditz,[c] Wolfram Heimbrodt,[c] Tsukasa Yoshida[d] and Derck Schlettwein *[a]

Received 13th January 2021,
Accepted 1st March 2021

DOI: 10.1039/d1cp00179e

rsc.li/pccp

Dye-sensitized solar cells (DSSCs) based on ZnO photoanodes have, despite extensive research, lagged behind cells based on TiO_2, which is due to generally lower open-circuit voltages V_{OC} and fill factors. Here, DSSCs have been prepared using Mg-doped ZnO (MZO) photoanodes based on nanoparticles, thin films or ZnO–MZO core–shell-type nanoparticles with varying Mg-concentration. The cells were studied in detailed photoelectrochemical and photoluminescence experiments. It was confirmed that V_{OC} was significantly increased by Mg-doping. A clear influence of the Mg-concentration was also revealed on the transport and recombination of electrons in MZO, leading to a higher cell performance at low and lower cell performance at high concentrations of Mg in MZO. Nanoparticles with a pure ZnO core and an MZO shell offered a way to lower the influence of increased transport resistance in MZO and to capitalize on the significantly improved V_{OC}.

Introduction

Dye-sensitized solar cells (DSSCs) present a low-cost solution for the conversion of sunlight into electrical energy.[1] Despite the rather limited overall efficiency of DSSCs under standard AM1.5G conditions and in view of a significantly higher efficiency at lower light intensities, they present an alternative as sustainable and renewable energy sources because they do not require high purity materials or high temperature preparation steps, leading to low energy payback times.[2,3] As a working principle, DSSCs rely on a dye molecule as a light absorber, which injects an electron from its excited state into an electron transport layer (ETL). Traditionally, the wide band gap n-type semiconductor TiO_2 has been used as an ETL but alternative semiconductors like ZnO or SnO_2 have been explored extensively, which is due to their favourable optical and electrical properties.[4] In particular, ZnO has been in the focus as an ETL in multiple solar cell concepts motivated by its high electron mobility.[5,6] While this can result in higher photocurrents, ZnO-based DSSCs generally exhibit a significantly lower open-circuit voltage V_{OC} and fill factor FF compared to TiO_2-based cells, which result in a lower power conversion efficiency (PCE).[7,8] This difference is further increased by a high degree of optimization of cell concepts towards TiO_2 regarding the structure of the adsorbed dye and the composition of the redox electrolyte. Additives to the redox electrolyte such as lithium (Li^+) and *tert*-butyl pyridine (TBP) are typically used to influence the position of the conduction band edge E_{CB} of the semiconductor leading to an increased V_{OC}.[9–12] However, recent studies have revealed that the influence of such additives is significantly lower on ZnO than on TiO_2 photoanodes.[8,13]

The cationic substitution of metal ions in ZnO has emerged as an alternative way of influencing the position of the conduction band and improving its photovoltaic performance.[14] The incorporation of Mg^{2+} ions was very successful, reaching solubility limits of up to 33%, depending on the growth technique used, enabled by the almost identical ionic radii of Zn^{2+}(0.57 Å) and Mg^{2+}(0.60 Å).[15,16] The resulting $Mg_xZn_{1-x}O$ (MZO) retains the Wurtzite crystal structure typical for ZnO at the desired increased band gap, and is tuneable by the Mg-concentration in the lattice. In consequence, MZO has already been used in various photovoltaic cell concepts, such as bulk heterojunction organic solar cells,[17] inverted polymer solar cells,[18] perovskite solar cells,[19,20] quantum dot solar cells,[21] as a buffer layer for CdTe-solar cells[22] and also in DSSCs with, however, photoanodes of strongly differing morphology, which hindered a direct correlation of cell properties with changes in the electrical characteristics caused by Mg-doping.[23–25] For DSSCs as well as for organic or polymer solar cells, the desired

[a] *Institute of Applied Physics and Center for Materials Research, Justus-Liebig-University, Heinrich-Buff-Ring 16, D-35392 Giessen, Germany. E-mail: schlettwein@uni-giessen.de*
[b] *Institute of Physical Chemistry, Justus-Liebig-University Giessen, Heinrich-Buff-Ring 17, D-35392 Giessen, Germany*
[c] *Department of Physics and Materials Science Centre, Philipps-University of Marburg, Renthof 5, D-35032 Marburg, Germany*
[d] *Department of Chemistry and Chemical Engineering, Faculty of Engineering, Yamagata University, Jonan 4-3-16, Yonezawa, Yamagata 992-8510, Japan*

† Electronic supplementary information (ESI) available: Experimental details, additional experimental results and data evaluation. See DOI: 10.1039/d1cp00179e

increase in V_{OC} was observed, related to an upward shift ΔE_{CB} of the conduction band position and of the quasi Fermi energy $E_{F,n}$. Furthermore, an increased short-circuit current J_{SC} and FF for concentrations of Mg^{2+} of 5% to 10% but a significant decrease in photocurrent for higher concentrations of Mg^{2+} were observed for all aforementioned types of solar cell devices. The increase in J_{SC} for small concentrations of Mg was discussed as being caused by an increased electron mobility in MZO for low Mg-concentrations.[21,26,27] For quantum dot solar cells it was predicted that an increased electron mobility would promote faster transport through the semiconductor layer, reduce recombination and enhance charge extraction.[28] Explicit measurements of the electron mobility in MZO using the Hall effect or space-charge limited currents on electron-only devices showed an increased mobility for Mg-concentrations of up to 10%, with a decrease for higher Mg-concentrations, falling even below the level of pure ZnO.[26,27] These findings fit well with a reported increase in the series resistance in polymer-oxide hybrid solar cell devices for Mg-concentrations above 10%.[18] Furthermore, an observed decrease in the photocatalytic activity of highly doped MZO in the decomposition of methylene blue was discussed as being due to increased recombination as a consequence of the calculated formation of shallow Mg^{2+} acceptor levels below the conduction band edge.[29]

In this work, these scattered results of the successful application of MZO in different types of solar cells are utilized to systematically establish an alternative path to increase the open-circuit voltage V_{OC} and the fill factor FF of ZnO-based DSSCs. We report the preparation and characterization of three types of MZO-based photoanodes. Thin-film (TF) photoanodes were prepared *via* a sol–gel process to provide a direct comparison to earlier studies of organic, polymer, perovskite and dye-sensitized solar cells. To establish a high surface area required in DSSCs for achieving a high dye-loading and, hence, good light harvesting, nanoparticulate (NP) photoanodes of MZO were also prepared, based on a different wet-chemical synthesis. Significantly enhanced V_{OC} and FF resulting from Mg^{2+}-integration into ZnO was shown for DSSCs using both these approaches that in part surpass the values of TiO_2-based DSSCs, even without applying commonly used additives. Furthermore, ZnO–MZO core–shell (CS) type photoanodes were prepared to combine the best of both, *i.e.* the high mobility of a pure ZnO core and the higher V_{OC} established by an MZO shell, and, thereby, increase the PCE. The influence of Mg^{2+}-doping on J_{SC} and strategies to further improve the cells are discussed based on detailed photoelectrochemical and photoluminescence results.

Experimental

Synthesis of MZO photoanodes and DSSC preparation

TF MZO photoanodes were prepared by spin-coating (2000 rpm, 60 s) a solution of zinc acetate dihydrate ($Znac_2$) and magnesium acetate tetrahydrate ($Mgac_2$) in 2-methoxyethanol (2ME) with molar ratios of 0, 5, 10, 20 and 25% Mg onto glass substrates coated with fluorine-doped tin oxide (FTO, Kaivo, $<15\ \Omega\ cm^{-2}$). 0.75 M solutions of ethanol amine and of total metal acetate in 2ME were heated to 50 °C and stirred on a hotplate for 15 min. After cooling, the solutions were filtered by a 0.45 μm pore size syringe filter.[17] The substrates were precleaned by subsequent ultra-sonification in RBS solution (Roth), acetone (Roth) and isopropanol (Roth) for 15 min each. The resulting thin films were thermally annealed in air at 300 °C for 15 min.

For the preparation of MZO nanoparticles, $Znac_2$ and $Mgac_2$ were dissolved in ethanol (0.3 M of metal acetate) in molar ratios of 0, 5, 10 and 20% Mg. Each solution was heated to 60 °C and an ethanolic solution of oxalic acid dihydrate was added dropwise under constant stirring until a concentration of 0.45 M was reached. The solution was left stirring under reflux for 1 h, before being centrifuged (6000 rpm, 10 min). The resulting white precipitate was dried in an oven in air at 100 °C overnight before calcination at 500 °C for 2 h. The resulting nanoparticles were formulated into a screen-printing paste by addition of terpineol and ethyl cellulose but without the addition of acetic acid as described in ref. 30. The paste was screen-printed onto a cleaned FTO-coated glass substrate as a circle with a radius of 3 mm, followed by heating to 500 °C at a rate of 10 °C min^{-1} and leaving it at that temperature for 60 min. For the preparation of CS-type films of MZO, 10 μl of the solutions used for the preparation of TF-MZO were drop cast onto NP photoanodes of pure ZnO, before being thermally annealed as described for TF above. All chemicals and solvents were used as received from Sigma-Aldrich, unless mentioned otherwise, without further purification. All photoanodes were sensitized by immersion in a 0.5 mM solution of the indoline dye DN216 (Chemicrea) and 0.2 mM lithocholic acid in 1 : 1 (volume) acetonitrile : *tert*-butanol for 15 min. Counter-electrodes for the DSSCs were prepared by drop-casting a 5 mM solution of chloroplatinic acid in ethanol onto a cleaned FTO-substrate and subsequently heating to 400 °C for 15 min. Sensitized photoanodes and counter-electrodes were mechanically connected and sealed by a hot-melting Surlyn® spacer (25 μm). The redox electrolyte consisted of 0.5 M PMII (3-propyl-1-methylimidazolium iodide) and 0.05 M I_2 in acetonitrile. The cell was filled with this electrolyte through predrilled holes in the counter electrode and sealed using Surlyn® foil and a coverslip glass.

Sample characterization

X-ray diffraction (XRD) patterns of the TF-samples on glass substrates (X'Pert Pro MRD) and the NP-powders (Rigaku Ultima III) were investigated *via* Cu-Kα radiation.

Optical absorption spectra of the TF-samples on glass substrates were measured in transmission (Lambda 365, PerkinElmer) and the band gaps were determined from Tauc-plots. The powder samples were studied by diffuse reflection (Solid-Spec 3700, Shimadzu) using a $BaSO_4$ reference and the absorption coefficients were calculated using the Kubelka–Munk function. UV-Vis spectra of the sensitized photoanodes were measured in reflection using an Ulbricht sphere (getProbe 5393 SET, getAMO) and a Tec5 diode array spectrometer.

Scanning electron microscopy (SEM) images were taken on a Zeiss MERLIN microscope with an acceleration voltage of 3 kV and an emission current of 100 pA. Energy dispersive X-ray spectroscopy (EDX) was performed at 10 kV and 2 μA (X-Max 50 mm^2, Oxford Instruments). Time-resolved photoluminescence (TRPL) measurements were carried out using a standard streak camera setup. A tuneable pulsed 100 fs, 80 MHz repetition rate Ti:Sapphire laser was used as the excitation source. The output wavelength of the laser was 845 nm and the pulses were frequency-doubled to 442.5 nm. A microscope objective was used to focus the laser onto the samples. The average laser power in front of the objective was set to 1 mW to prevent bleaching effects.

Photoelectrochemical characterization was carried out using an IM6 potentiostat and a CIMPSpcs system (Zahner Elektrik). Current–voltage (*I–V*) characteristics were measured in the dark or under illumination using an LS0106 xenon arc lamp with an LSZ189 AM 1.5G filter with the intensity set to 100 mW cm^{-2} on a calibrated ML-020VM pyranometer (EKO Instruments). EQE measurements were performed under illumination by a white light source and a monochromator (TLS02, Zahner Elektrik) at a fixed intensity of 0.1 mW cm^{-2} on the sample. Electrochemical impedance spectroscopy (EIS) was performed with an amplitude of 0.01 V in a frequency range of 1 MHz to 0.3 Hz under illumination by a 510 nm LED with intensities ranging from 0.5 to 15 mW cm^{-2} while the DSSCs were kept at open-circuit bias. The spectra were fitted with RelaxIS 3 (rhd instruments) using the equivalent circuit shown in Fig. S1 (ESI†).

Results and discussion

SEM images in top-view as well as in cross-section show the mesoporous structure of the NP-type (Fig. 1a and d) and CS-type (Fig. 1b and e) photoanodes. Nanoparticles with a size of 10 to 40 nm are partially agglomerated into larger needle-like structures. A loose packing of these needles leads to the formation of pores across the entire film with about 100 nm diameter, favorable for the accessibility by the redox shuttle in DSSCs. The presence of smaller open volume between adjacent nanoparticles ensures a high overall surface area, needed for the adsorption of a sufficient amount of dye. Cross-section images also served to determine the film thickness. NP- as well as CS-type samples exhibited a largely homogeneous thickness of (3.0 ± 0.2) μm. SEM images of the TF-type samples (Fig. 1c and f) revealed a much smaller particle size below 10 nm that is further decreased for higher Mg-concentrations (Fig. S5, ESI†). The TF films completely covered the substrate at a thickness of typically 20 nm with root-like structures of up to 200 nm diameter on top.[23] As a combination between NP- and TF-type, the CS-type layers show the agglomerates of the NP-films covered with much smaller sized nanoparticles (Fig. 1b) like those of the TF-samples. However, the cross-section image (Fig. 1e) reveals that parts of the ZnO-nanoparticles near the bottom of the films remain uncovered by the MZO shell.

The crystal structures of the ZnO and MZO nanoparticles and thin films were studied by XRD measurements, which are

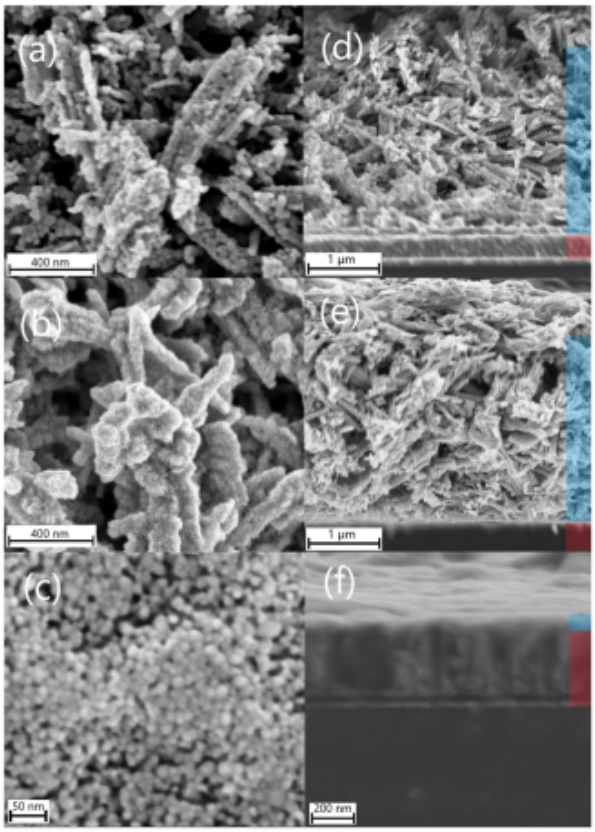

Fig. 1 SEM images of (a and d) pure ZnO nanoparticles (NP) and (b and e) CS-type nanoparticles after coating with an MZO shell compared to a TF sample (c and f) for which the same coating solution was used. Top views are seen in (a–c) while (d–f) show cross-sections obtained after breaking of the samples with the thickness (obtained from a variety of similar images) of the active film marked in blue and of the FTO substrate marked in red.

presented in Fig. 2 and Fig. S2, S3 (ESI†). The overview for MZO NPs of different Mg-contents in Fig. 2a only exhibits the diffraction peaks of the hexagonal wurtzite of ZnO. No additional phase was detected after the introduction of Mg into the crystal lattice, indicating that the Mg^{2+} ions were fully integrated. The detailed spectra of the (100) (Fig. 2b) and (002) (Fig. 2c) peaks revealed expected shifts of the peak position towards lower and higher angles, respectively.

The calculated lattice constants show an increase in *a*- and a decrease in the *c*-direction (see Table S1, ESI†) and fit previous reports very well.[15,31] The TF-samples (Fig. S2, ESI†) showed equivalent results, proving that nanoparticulate and thin film MZO photoanodes of varying Mg-content were successfully fabricated.

In order to study the effect of Mg^{2+} incorporation on the band gap of ZnO, optical absorption of the MZO NPs and TFs was measured and is presented in the form of Tauc-plots characteristic for direct band gaps, allowing the determination of the band gap (Table S2, ESI†). Both in the case of thin films (Fig. 3a) and of nanoparticles (Fig. S4, ESI†) a significant increase in the band gap of MZO with increasing

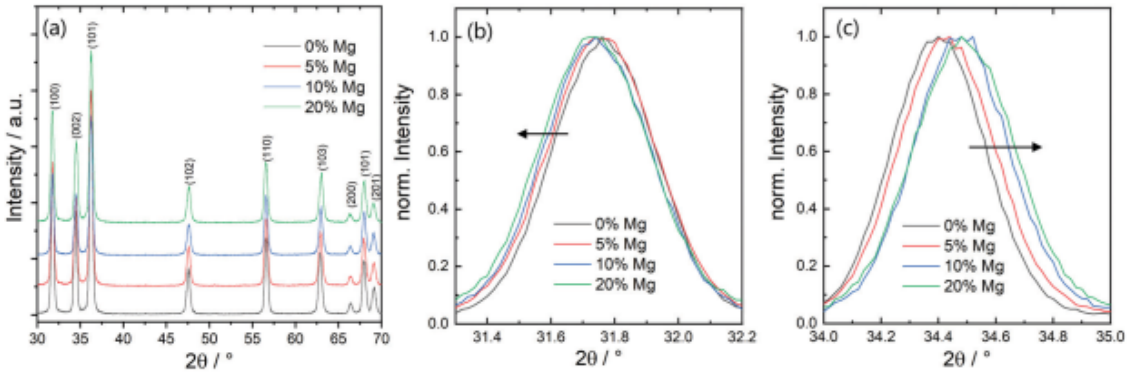

Fig. 2 XRD of MZO nanoparticles. (a) overview of MZO NP with 0, 5, 10 and 20% Mg. The typical ZnO wurtzite reflexes are indexed. (b) Details of the (100) and (c) (002) reflexes with a shift of the reflex position indicated for increasing Mg-content.

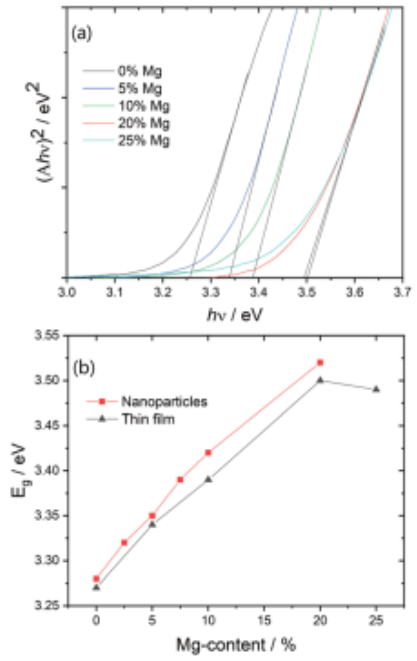

Fig. 3 (a) Tauc-plot of the optical absorption spectra and fits to the linear part of MZO thin films with different Mg-concentrations. (b) Band gaps of MZO thin films and nanoparticles for different Mg-concentrations with lines to guide the eye.

Mg-concentration is revealed (Fig. 3b). A linear, almost identical increase was obtained for both kinds of prepared MZO up to a Mg-content of 20%, but saturation occurred at higher concentrations. Similar increases in the band gap have previously been reported for MZO.[15,18,23] The stagnation of the band gap for Mg-contents higher than 20% was reported to be caused by reaching the solubility limit of Mg^{2+} in ZnO.[32]

It was previously assumed that the increase in the band gap directly affects the position of the conduction band edge E_{CB}, while the valence band edge E_{VB} was found to stay practically unaffected.[23,33,34] However, recent reports indicated that E_{CB} only exhibits a small shift in position, and the increased band gap is mainly caused by a lower E_{VB}.[26] Nevertheless, a shift in the Fermi energy level E_F of the semiconductor towards the conduction band was reported, similar in size to the increase of the band gap.[17,21] Density functional theory (DFT) calculations confirm the increase of the band gap by the incorporation of Mg into the ZnO lattice by substitution of Zn up to 5% Mg and by interstitial doping above 5% Mg, lifting the energy of the conduction band, introducing new energy levels below the conduction band and raising the charge carrier concentration.[29] Such additional levels may very well give rise to the increased Urbach tail as indicated in Fig. 3a and are discussed below in the context of the observed increased recombination.

I–V characteristics were measured for all three photoanode types sensitized with the indoline dye DN 216 and are presented in Fig. 4 and Table 1. All cell types exhibit the same trend of increased V_{OC} and FF with higher Mg-concentration, remedying the serious shortcomings of ZnO-based DSSCs significantly and proving the validity of the strategy outlined above. This increase of the V_{OC} can be well explained by the increase of the band gap and the related shift in the quasi Fermi-level energy $E_{F,n}$ of the semiconductor. The measured values of up to 777 mV for the NP-cell type and 760 mV for the TF-cell type with 20% Mg-concentration are among the highest ever reported V_{OC} for the commonly used iodide redox couple and surpass the voltages reported in high-efficiency TiO_2-based DSSCs.[35]

The increase of V_{OC} with the Mg-content, however, is generally lower for CS cells compared to the other cell types, most likely caused by partial access of the electrolyte to the underlying undoped ZnO. The alternative assumption of an $E_{F,n}$ shifted from the position in the corresponding TF samples would require Mg diffusion from the shell into the underlying undoped core, which was observed to occur above 800 °C only,[36] a temperature considerably higher than the present 300 °C.

For higher Mg-concentrations, a general trend of decreasing J_{SC} was observed, which leads to strongly decreased PCE. This decrease in J_{SC} with increased Mg-content was seen in earlier reports, lacks detailed understanding and is studied in

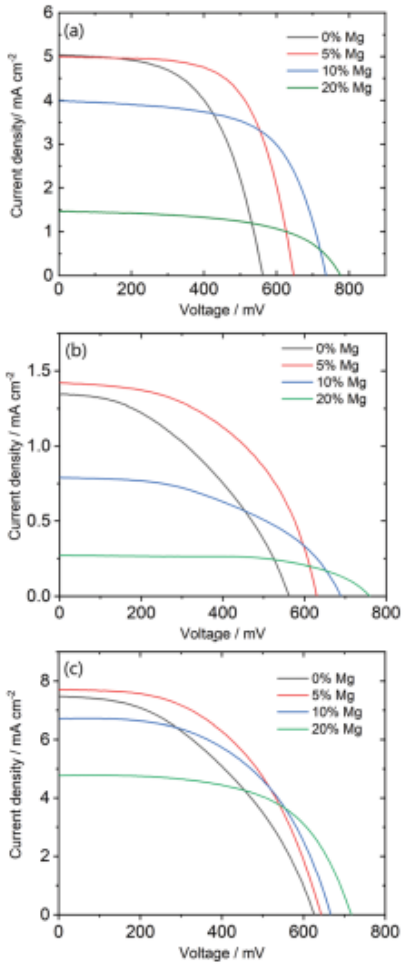

Fig. 4 I–V curves of (a) NP type cells, (b) TF type cells and (c) CS type cells for different Mg-concentrations.

Table 1 Photovoltaic characteristics of all three prepared cell types with varying Mg-concentration

Type	Mg-Content/%	J_{SC}/mA cm^{-2}	V_{OC}/mV	FF	PCE/%
NP	0	4.99	562	0.57	1.59
	5	4.95	647	0.64	2.07
	10	3.95	736	0.62	1.82
	20	1.45	777	0.64	0.56
TF	0	1.34	562	0.42	0.31
	5	1.42	630	0.51	0.45
	10	0.79	689	0.47	0.26
	20	0.27	760	0.62	0.13
CS	0	7.47	626	0.43	2.04
	5	7.69	643	0.51	2.53
	10	6.71	666	0.53	2.36
	20	4.77	717	0.59	2.04

detail below. It is seen that this decrease is less significant for the CS-type cells compared to the NP- and TF-type cells which indicates the major benefit of the CS-type cells for higher Mg-contents and leads to their higher PCE.

Similar to the results reported for other solar cell types,[17,23,26] an initial increase in J_{SC} for a Mg-concentration of 5% can be observed for all cell types, leading to overall higher PCE of cells with up to 10% Mg. The CS-type cells generally exhibit the highest PCE of all cell types for all concentrations of Mg, which is due to a generally higher J_{SC} resulting from the highest light absorption, also when compared to the NP-type samples (Fig. 4a). Consequently, similar values were determined for the internal quantum efficiency (QE, Table S3, ESI†) for NP and CS cells at low Mg-concentration. TF cells, despite high QE showed low currents because of a small amount of adsorbed dye.

Fig. 5 shows the optical absorption spectra of all photoanodes studied. In contrast to the results shown by Kim *et al.*,[23] no clear dependence of light absorbance on the Mg-concentration of the present photoanodes can be detected. Since the absorbance is proportional to the amount of dye adsorbed on the semiconductor surface and since all presented spectra show an almost identical shape, we conclude that the adsorption of the dye to the surface has not changed by the addition of Mg in any of the presently chosen methods of synthesis. While the apparent absorption peak of DN216 on MZO for the TF-photoanodes (see Fig. 5b) shows an increase for increasing Mg-concentrations, it can be assumed that this is caused by varying degrees of light scattering because of the almost constant difference between the absorption maximum at 540 nm and the minimum at around 450 nm for all Mg-concentrations.

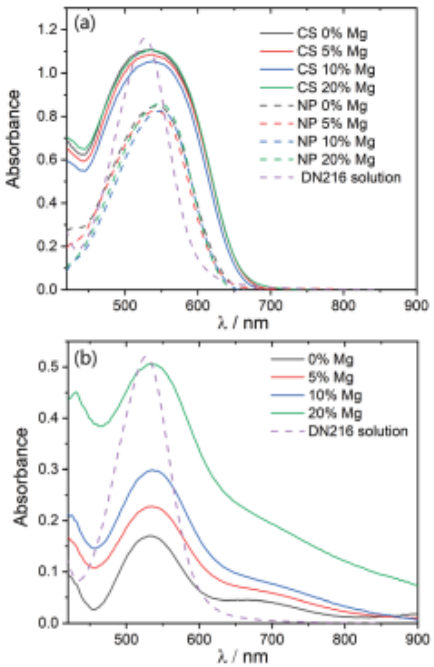

Fig. 5 UV-vis spectra of the photoanodes sensitized with DN216. (a) CS- and NP-type photoanodes show no dependence of dye adsorption on Mg-concentration. (b) TF-type photoanodes show increased light-scattering with increasing Mg-concentration.

The increase in light scattering is probably caused by a decrease in particle size with an increasing Mg-concentration (Fig. S5, ESI†). Light scattering is far less pronounced for the CS-type and NP-type photoanodes (Fig. 2a). Both these types also show no correlation between dye loading and Mg-content and show a significantly higher loading than the TF-type photoanodes, with the CS-type samples showing the highest dye loading. Since all CS samples were prepared from the same 0% NP, it can be concluded that the CS-coating process increased the surface area of the photoanodes, leading to a higher dye loading. An increased surface area of the CS films is confirmed by a direct comparison of SEM images of NP, CS and TF samples (Fig. 2).

The external quantum efficiency (EQE) under short circuit conditions (Fig. 6 and Fig. S6, S7, ESI†) directly follows the absorption spectra of the adsorbed dye for all cells studied. The EQE in DSSCs is given by the product of light-harvesting efficiency η_{lh}, electron injection efficiency η_{inj}, dye regeneration efficiency η_{reg} and electron collection efficiency η_{col}:

$$\mathrm{EQE} = \eta_{lh}\eta_{inj}\eta_{reg}\eta_{col} \quad (1)$$

In order to analyse the significant differences observed in the measured EQE spectra of the NP-type photoanodes (Fig. 6) and CS-type photoanodes (Fig. S7, ESI†) with different Mg-concentrations, η_{lh} can be assumed to be constant within a given series NP or CS because of widely identical absorbance spectra within each series (Fig. 5a). Furthermore, η_{reg} can be assumed constant among the samples since identical energy levels and concentrations of dye and electrolyte components were used. As seen below in the photoluminescence measurements, η_{inj} in a first approximation can also be assumed to be constant for all cells. Therefore, the observed differences in EQE are caused by different η_{col} values. In order to study η_{col}, we determined the corresponding electron diffusion length L_{NP} and L_{CS} (Table 2) for the NP- and CS-type photoanodes, respectively, by a model using absorbance data and film thickness (fits in Fig. 6 and Fig. S7, ESI†).[37] The measured spectra are well fit by the model, aside from fluctuations in EQE around 470 nm, which, however, did not appear in the absorption spectra and are probably caused by fluctuations in effective illumination intensity (interference, scattering) in this range. High L was found for pure ZnO and 5% MZO, while the 10% and 20% MZO samples showed a significant decrease in both L_{NP} and L_{CS}. The EQE data for the TF-type photoanodes (Fig. S6, ESI†) could not be fitted, which is due to the large errors caused by difficulties to accurately determine the film thickness and by the strong influence of light scattering on the optical absorbance spectra.

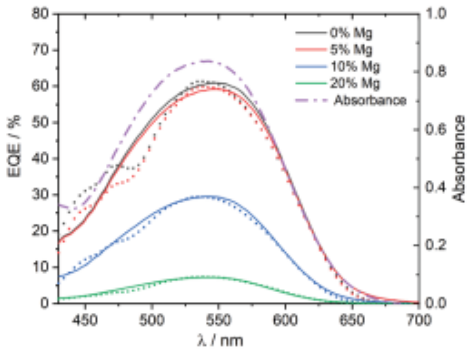

Fig. 6 Measured EQE spectra (dots) and fits according to ref. 37 (lines) of NP-type photoanodes of varying Mg-concentration. The measured absorption spectra of the pure ZnO NP-type photoanode (dashed-dotted line) has been included for comparison.

Table 2 Electron diffusion lengths in NP-type and CS-type photoanodes determined from the EQE spectra as compared to the measured film thickness of (3.0 ± 0.2) μm

Mg-content/%	L_{NP}/μm	L_{CS}/μm
0	2.7	2.8
5	2.5	2.6
10	0.85	1.8
20	0.16	0.92

The electron diffusion length L is closely related to the recombination resistance R_{rec} and the transport resistance R_{tr}[38–40]

$$L = d \cdot \sqrt{\frac{R_{rec}}{R_{tr}}} \quad (2)$$

The decreased L (Table 2) and, thereby, a decreased η_{col}, EQE and PCE (Table 1) found for higher Mg-concentrations in MZO hints at decreased R_{rec} or increased R_{tr} for increasing Mg-content. The significantly higher L_{CS} compared to L_{NP} at 10% and 20% MZO, therefore, hint at suppressed recombination or improved conductivity by utilizing pure ZnO as the core, leading to less-attenuated J_{SC} and PCE for higher Mg-content in CS- compared to NP-electrodes. The integrated EQE resulted in J_{SC} 5 to 15% lower than the values measured in the I–V curves, which is reasonable because of missing contributions below 430 nm in EQE (Fig. 6 and Fig. S6, S7, ESI†) as opposed to the AM 1.5 spectrum.

Intensity-dependent electrochemical impedance spectroscopy (EIS) measurements were performed in order to determine R_{rec} and R_{tr} quantitatively. The Nyquist-plots shown in Fig. 7 show an overall smaller impedance for the MZO with 5% Mg when compared to pure ZnO, for NP as well as CS-type cells. For larger Mg content (20%), the overall impedance increases. Furthermore, the shape of the central semicircle, dominated by properties of the photoanode (R_{rec} and/or R_{tr}) changes significantly with Mg-content, towards a strongly asymmetric shape for increasing Mg-content. These differences occur to a smaller extent for the CS- compared to the NP-type cells, indicating significantly suppressed impact of an increasing resistance in the CS-photoanodes. When trying to fit the curves with an equivalent circuit typically used for ZnO-based DSSCs,[41] we realized that this model did not fit all measured cells. For the photoanodes with 10% or 20% Mg-concentration, the overall resistance increased and the semicircle developed an asymmetric shape, especially in the high-frequency regime (Fig. 7a, inset) where a 45°-slope appears, indicative of a Gerischer impedance.[42]

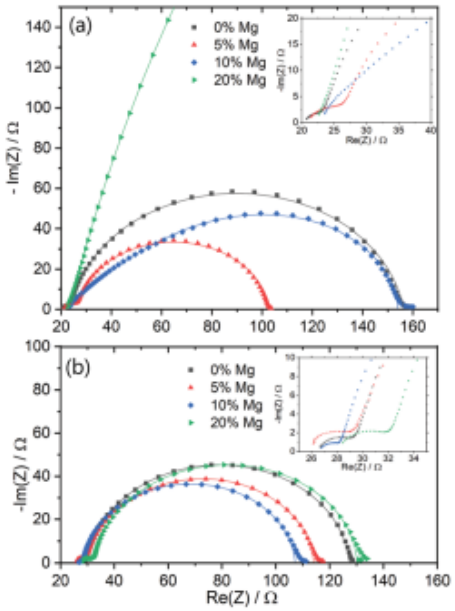

Fig. 7 Nyquist-plot of EIS measurements of (a) NP-type photoanode and (b) CS-type photoanode at 300 mW cm^{-2} illumination by a 510 nm LED. The inset shows the high-frequency region of the measurement.

This phenomenon can normally be observed in TiO_2-based DSSCs and occurs when the electron transport-time τ_{tr} exceeds the electron life time τ_n because of a high transport resistance R_{tr}.[38,43] Such influence of R_{tr} obviously is smaller in the CS-type photoanodes with their core of pure ZnO since the asymmetric deformation of the semicircle is smaller. We utilized R_{rec}/R_{tr} determined from eqn (2) and the data of L (Table 2) to fit the measured EIS spectra upon addition of a Gerischer-type impedance (Fig. S1, ESI†). A fixed ratio R_{rec}/R_{tr} is needed for such a fit since the linear dependency of both values on each other would otherwise hinder a quantitative analysis.[43,44] The corresponding capacitance was too large to assign it to a chemical capacitance but might represent a superposition with additional contributions by, *e.g.*, space charges in the cells.

The values for R_{tr} and R_{rec} extracted from the fit of the EIS data (Table 3) show the necessity of considering changes in both R_{tr} and R_{rec} to explain the present findings as opposed to earlier studies using either a decreased electron mobility[26–28] or an increased recombination probability[23,29] for MZO with a high content of Mg. R_{tr} decreases for both types of photoanodes from pure ZnO towards 5%, well in line with earlier findings of an increased mobility.[26–28] A significantly increased R_{tr} was found for higher concentrations of Mg, as also seen in those earlier studies. The R_{tr} found for the CS-type photoanodes using the pure ZnO core show a much smaller increase compared to the NP-type photoanodes, explaining the much lower drop in L (Table 2), J_{SC} and PCE (Table 1) of the CS-type compared to the NP-type as well as TF-type cells, both of which rely on conduction in fully doped MZO. Simultaneously, R_{rec} of NP- as well as CS-type photoanodes decreases monotonically with the increase in Mg-concentration leading to the observed optimum.

Intensity-modulated photovoltage spectroscopy (IMVS) was measured at open-circuit under varied light intensity to obtain a measure of the effective electron lifetime τ_n.[45,46] To compensate the obtained values of V_{OC} for different positions of the $E_{F,n}$ and obtain values of τ_n independent of the occupation of electronic states in the semiconductor and, hence, characteristic for the rate constant of recombination for the different photoanode materials, we used the observed change of E_g (Fig. 3 and Fig. S8, ESI†) relative to pure ZnO used as in ref. 17 and 21. Experimental IMVS results are shown in Fig. S9 (ESI†). The effective electron lifetimes τ_n for all three types of photoanodes are compared at V_{OC} = 400 mV (Table 4) All types exhibit the same trend of a monotonic decrease of τ_n with Mg-content. Such decrease of τ_n is expected for an increased rate constant of recombination with an increasing Mg-concentration corresponding to the decreasing R_{rec} as seen in the ESI† (see Table 3) and is also in good accordance with DFT simulations that predicted interstitial Mg^{2+} to function as recombination centres for electrons.[29]

Subsequent to the initial fast injection typically in the sub-ps range, time-resolved photoluminescence (TRPL) spectra were measured in the ps time range to study the quenching of dye luminescence by electron transfer from a relaxed excited state to energy levels in the photoanodes with different Mg-contents. As reported before, the density of accessible acceptor states in the semiconductor can be probed.[4,47] Electrons in the relaxed excited state of the dye are most sensitive to changes in the concentration of accessible acceptor states at a given energy. In similar experiments, an enhanced charge extraction in quantum dot and perovskite solar cells was found for MZO-photoanodes and attributed to a faster electron transport at a Mg concentration of 10%.[26,28,48] In the present experiments (Fig. 8 and Fig. S10, ESI†), we found emission from the excited state of the dye at monotonically increasing intensity with increasing Mg-content and, hence, a monotonically increasing efficient lifetime of the excited state, indicating a decrease in electron transfer rate from the relaxed excited state of the dye to the semiconductor. A bi-exponential fit was used to determine

Table 3 Transport and recombination resistance of the CS- and NP-type photoanodes used for fitting the measured EIS spectra

	NP		CS	
Mg-content/%	R_{tr}/Ω	R_{rec}/Ω	R_{tr}/Ω	R_{rec}/Ω
0	135	92	88	71
5	84	52	80	60
10	421	35	136	41
20	1006	23	241	39

Table 4 IMVS-derived effective electron lifetimes τ_n for all three photoanode types determined at 400 mV under red light illumination

Mg-content/%	$\tau_{n,NP}$/ms	$\tau_{n,TF}$/ms	$\tau_{n,CS}$/ms
0	114	64	370
5	75	39	186
10	35	14	69
20	6	8	22

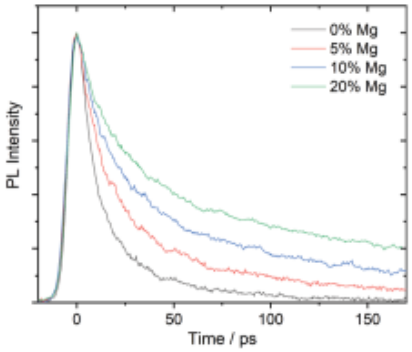

Fig. 8 Time-resolved photoluminescence (TRPL) spectra of NP-type DSSCs at varying Mg-concentrations.

Table 5 Photoluminescence decay time constants τ_{PL} for the three types of photoanodes at varying Mg-concentrations

Mg-content/%	$\tau_{PL,NP}$/ps	$\tau_{PL,TF}$/ps	$\tau_{PL,CS}$/ps
0	42	54	35
5	61	98	58
10	98	122	70
20	191	151	99

the decay time constants from the measured TRPL spectra (Fig. S10, ESI†). The shorter time constants of about 10 ps were attributed to the instrument response time and fit the instrument specifications very well.

The longer time constants τ_{PL} are shown in Table 5 for all three types of photoanodes and show a systematic increase with the Mg-content in MZO. Differences in electron transport or recombination can be excluded as the origin, since both occur in the millisecond- rather than ps-range after injection.[4,49] Instead, it can be assumed that the increased efficient life times are caused by an upward shift of the quasi-Fermi level (Fig. 9). We reported previously, that the quenching of the relaxed excited state of the dye can be significantly slowed down by applying a negative bias to the photoanode, simulating an upward shift in $E_{F,n}$.[50,51] Since similar characteristics resulted from the present experiments, we conclude that an upward shift in $E_{F,n}$ was achieved by doping of ZnO with Mg^{2+}, leading to the observed increase in efficient lifetimes. However, because the electron transfer from the relaxed excited states, representing the slowest component of electron injection, is still completed within 35 to 190 ps for all types of photoanodes and all Mg-concentrations, fast injection in the sub-ps time regime from the initially excited dye into the semiconductor can be assumed for all present electrodes as generally found for dye-sensitized photoanodes.[52–55]

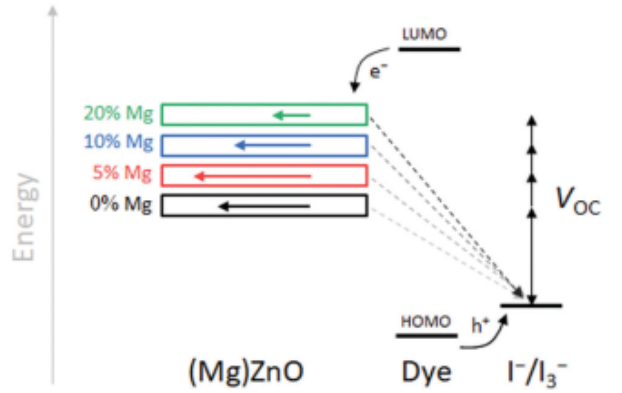

Fig. 9 Use of differently doped MZO as ETL in DSSCs. The Mg-content is shown and the semiconductor energy levels shifted according to the observed change in $E_{F,n}$. Observed differences in electron mobility are shown by differently long horizontal arrows and observed differences in recombination are shown by the intensity of the dashed arrows.

Conclusions

The performance of DSSCs was shown to be greatly influenced by using MZO-based photoanodes instead of pure ZnO. Significantly enhanced V_{OC} was obtained depending on the Mg-concentration as a consequence of the systematic tuning of the position of the quasi-Fermi energy $E_{F,n}$ in MZO. For high Mg-concentrations, however, smaller J_{SC} led to a decreased performance. Unlike earlier findings, the present extended selection of characterization methods revealed the relevance of systematic variations in both electron transport as well as electron recombination caused by Mg-doping of ZnO in order to understand the observed differences in the photocurrent. These findings are summarized in Fig. 9. For intermediate Mg-contents of about 5%, optimum cell performance was found, caused by increased V_{OC} and widely maintained or even slightly increased J_{SC}. A decreased transport resistance led to an increased electron lifetime and supported the high current, despite a slightly increased recombination rate constant caused by additional trap-levels. Detailed variation of the Mg-content in the range below 10% will yield the respective optimum for a given device application, depending on the specific relevance of recombination relative to collection. Furthermore, the core–shell-type approach has shown the potential to attenuate the effects of decreased mobility in highly doped MZO by using a pure ZnO core, thereby preserving a larger current and providing the increased voltage for higher Mg-concentrations. Such an approach might also help to increase the success in applications of MZO in other solar cell types such as organic or perovskite solar cells. Finally, the increased chemical stability of MZO compared to ZnO as recently seen in perovskite solar cells[19] may also bear some potential to increase the stability of MZO-based DSSCs compared to ZnO-based ones.

Conflicts of interest

There are no conflicts to declare.

Acknowledgements

The authors acknowledge financial support from the Deutsche Bundesstiftung Umwelt (DBU) *via* the project 20019/600, the

Japan Society for the Promotion of Science (JSPS) *via* SP19316 within the "JSPS summer school program" and the Deutsche Forschungsgemeinschaft (DFG) *via* the GRK (Research Training Group) 2204 "Substitute Materials for Sustainable Energy Technologies".

Notes and references

1 M. Grätzel and B. O'Regan, *Nature*, 1991, 737.
2 A. Hagfeldt, *Ambio*, 2012, **41**(Suppl 2), 151.
3 F. de Angelis and P. Kamat, *ACS Energy Lett.*, 2017, **2**(7), 1674.
4 A. Hagfeldt, G. Boschloo, L. Sun, L. Kloo and H. Pettersson, *Chem. Rev.*, 2010, **110**(11), 6595.
5 J. Qu, Y. Yang, Q. Wu, P. R. Coxon, Y. Liu, X. He, K. Xi, N. Yuan and J. Ding, *RSC Adv.*, 2014, **4**(22), 11430.
6 A. Omar and H. Abdullah, *Renewable Sustainable Energy Rev.*, 2014, **31**, 149.
7 A. K. Chandiran, M. Abdi-Jalebi, M. K. Nazeeruddin and M. Grätzel, *ACS Nano*, 2014, **8**(3), 2261.
8 J. Idígoras, G. Burdziński, J. Karolczak, J. Kubicki, G. Oskam, J. A. Anta and M. Ziółek, *J. Phys. Chem. C*, 2015, **119**(8), 3931.
9 T. Le Bahers, F. Labat, T. Pauporté and I. Ciofini, *Phys. Chem. Chem. Phys.*, 2010, **12**(44), 14710.
10 H. Paulsson, L. Kloo, A. Hagfeldt and G. Boschloo, *J. Electroanal. Chem.*, 2006, **586**(1), 56.
11 T. Stergiopoulos, E. Rozi, C.-S. Karagianni and P. Falaras, *Nanoscale Res. Lett.*, 2011, **6**, 307.
12 G. Boschloo, L. Häggman and A. Hagfeldt, *J. Phys. Chem. B*, 2006, **110**(26), 13144.
13 R. Ruess, S. Scarabino, A. Ringleb, K. Nonomura, N. Vlachopoulos, A. Hagfeldt, G. Wittstock and D. Schlettwein, *Phys. Chem. Chem. Phys.*, 2019, **21**(24), 13047.
14 R. Vittal and K.-C. Ho, *Renewable Sustainable Energy Rev.*, 2017, **70**, 920.
15 V. Etacheri, R. Roshan and V. Kumar, *ACS Appl. Mater. Interfaces*, 2012, **4**(5), 2717.
16 A. Ohtomo, M. Kawasaki, T. Koida, K. Masubuchi, H. Koinuma, Y. Sakurai, Y. Yoshida, T. Yasuda and Y. Segawa, *Appl. Phys. Lett.*, 1998, **72**(19), 2466.
17 B. A. MacLeod, P. Schulz, S. R. Cowan, A. Garcia, D. S. Ginley, A. Kahn and D. C. Olson, *Adv. Energy Mater.*, 2014, **4**(13), 1400073.
18 D. C. Olson, S. E. Shaheen, M. S. White, W. J. Mitchell, M. F. A. M. van Hest, R. T. Collins and D. S. Ginley, *Adv. Funct. Mater.*, 2007, **17**(2), 264.
19 S. S. Mali, J. V. Patil and C. K. Hong, *Adv. Energy Mater.*, 2020, **10**(3), 1902708.
20 Z. Yin, Q. Zheng, S.-C. Chen, D. Cai and Y. Ma, *Adv. Energy Mater.*, 2016, **6**(4), 1501493.
21 Z. Yin, Q. Zheng, S.-C. Chen, D. Cai, L. Zhou and J. Zhang, *Adv. Energy Mater.*, 2014, **4**(7), 1301404.
22 D.-B. Li, Z. Song, R. A. Awni, S. S. Bista, N. Shrestha, C. R. Grice, L. Chen, G. K. Liyanage, M. A. Razooqi, A. B. Phillips, M. J. Heben, R. J. Ellingson and Y. Yan, *ACS Appl. Energy Mater.*, 2019, **2**(4), 2896.
23 C. J. Raj, K. Prabakar, S. N. Karthick, K. V. Hemalatha, M.-K. Son and H.-J. Kim, *J. Phys. Chem. C*, 2013, **117**(6), 2600.
24 X. Guo, H. Dong, G. Niu, Y. Qiu and L. Wang, *RSC Adv.*, 2014, **4**(41), 21294.
25 C. Justin Raj, S. N. Karthick, K. V. Hemalatha, M.-K. Son, H.-J. Kim and K. Prabakar, *J. Sol–Gel Sci. Technol.*, 2012, **62**(3), 453.
26 J. Song, E. Zheng, L. Liu, X.-F. Wang, G. Chen, W. Tian and T. Miyasaka, *ChemSusChem*, 2016, **9**(18), 2640.
27 M. Caglar, Y. Caglar and S. Ilican, *Physica B*, 2016, **485**, 6.
28 X. Zhang, P. K. Santra, L. Tian, M. B. Johansson, H. Rensmo and E. M. J. Johansson, *ACS Nano*, 2017, **11**(8), 8478.
29 X. Qiu, L. Li, J. Zheng, J. Liu, X. Sun and G. Li, *J. Phys. Chem. C*, 2008, **112**(32), 12242.
30 S. Ito, P. Chen, P. Comte, M. K. Nazeeruddin, P. Liska, P. Péchy and M. Grätzel, *Prog. Photovoltaics*, 2007, **15**(7), 603.
31 M. Ghosh and A. K. Raychaudhuri, *J. Appl. Phys.*, 2006, **100**(3), 34315.
32 M. Wang, E. J. Kim, S. Kim, J. S. Chung, I.-K. Yoo, E. W. Shin, S. H. Hahn and C. Park, *Thin Solid Films*, 2008, **516**(6), 1124.
33 A. Janotti and C. G. van de Walle, *Phys. Rev. B*, 2007, **75**(12), 121201.
34 H. Chen, X. Ma, J. Zhang, Q. Li, H. Liu, Z. Chen, G. Chu and S. Chu, *Opt. Mater. Express*, 2018, **8**(4), 785.
35 J.-M. Ji, H. Zhou, Y. K. Eom, C. H. Kim and H. K. Kim, *Adv. Energy Mater.*, 2020, **10**(15), 2000124.
36 A. K. Das, P. Misra, R. S. Ajimsha, A. Bose, S. C. Joshi, S. Porwal, T. K. Sharma, S. M. Oak and L. M. Kukreja, *J. Appl. Phys.*, 2013, **114**(18), 183103.
37 S. Soedergren, A. Hagfeldt, J. Olsson and S.-E. Lindquist, *J. Phys. Chem.*, 1994, **98**(21), 5552.
38 J. Bisquert and R. A. Marcus, *Top. Curr. Chem.*, 2014, **352**, 325.
39 J. Bisquert and I. Mora-Seró, *J. Phys. Chem. Lett.*, 2010, **1**(1), 450.
40 A. B. F. Martinson, M. S. Góes, F. Fabregat-Santiago, J. Bisquert, M. J. Pellin and J. T. Hupp, *J. Phys. Chem. A*, 2009, **113**(16), 4015.
41 R. Ruess, S. Haas, A. Ringleb and D. Schlettwein, *Electrochim. Acta*, 2017, **258**, 591.
42 F. Fabregat-Santiago, G. Garcia-Belmonte, I. Mora-Seró and J. Bisquert, *Phys. Chem. Chem. Phys.*, 2011, **13**(20), 9083.
43 R. Ruess, J. Horn, A. Ringleb and D. Schlettwein, *J. Phys. Chem. C*, 2019, **123**(36), 22074.
44 Y. Liu, J. R. Jennings, Y. Huang, Q. Wang, S. M. Zakeeruddin and M. Grätzel, *J. Phys. Chem. C*, 2011, **115**(38), 18847.
45 A. Hagfeldt and L. Peter, in *Dye-sensitized Solar Cells*, ed. K. Kalyanasundaram, EPFL Press, Lausanne, 2010.
46 L. M. Peter and K. G. U. Wijayantha, *Electrochim. Acta*, 2000, **45**, 4543.
47 I. Meyenburg, J. Falgenhauer, N. W. Rosemann, S. Chatterjee, D. Schlettwein and W. Heimbrodt, *J. Appl. Phys.*, 2016, **120**(21), 215502.
48 X. Zhang, K. Welch, L. Tian, M. B. Johansson, L. Häggman, J. Liu and E. M. J. Johansson, *J. Mater. Chem. C*, 2017, **5**(42), 11111.

49 S. Ardo and G. J. Meyer, *Chem. Soc. Rev.*, 2009, **38**(1), 115.
50 I. Meyenburg, N. Hofeditz, R. Ruess, M. Rudolph, D. Schlettwein and W. Heimbrodt, *AIP Adv.*, 2018, **8**(5), 55218.
51 S. E. Koops, B. C. O'Regan, P. R. F. Barnes and J. R. Durrant, *J. Am. Chem. Soc.*, 2009, **131**(13), 4808.
52 E. Rohwer, I. Minda, G. Tauscher, C. Richter, H. Miura, D. Schlettwein and H. Schwoerer, *ChemPhysChem*, 2015, **16**(5), 943.
53 E. Rohwer, C. Richter, N. Heming, K. Strauch, C. Litwinski, T. Nyokong, D. Schlettwein and H. Schwoerer, *ChemPhysChem*, 2013, **14**(1), 132.
54 G. Ramakrishna, D. A. Jose, D. K. Kumar, A. Das, D. K. Palit and H. N. Ghosh, *J. Phys. Chem. B*, 2005, **109**(32), 15445.
55 G. Benkö, J. Kallioinen, J. E. I. Korppi-Tommola, A. P. Yartsev and V. Sundström, *J. Am. Chem. Soc.*, 2002, **124**(3), 489.

Supplementary Information for

Influence of Mg-doping in ZnO Photoanodes on their Characteristics in Dye-Sensitized Solar Cells

Andreas Ringleb [a], Raffael Ruess [b], Nico Hofeditz [c], Wolfram Heimbrodt [c], Tsukasa Yoshida [d] and Derck Schlettwein [a,]*

[a] Institute of Applied Physics and Center for Materials Research, Justus-Liebig-University Heinrich-Buff-Ring 16, D-35392 Giessen, Germany

[b] Institute of Physical Chemistry, Justus-Liebig-University Giessen,

Heinrich-Buff-Ring 16, 35392 Giessen, Germany

[c] Department of Physics and Materials Science Centre, Philipps-University of Marburg

Renthof 5, 35032 Marburg, Germany

[d] Department of Chemistry and Chemical Engineering, Faculty of Engineering, Yamagata University, Jonan 4-3-16, Yonezawa, Yamagata 992-8510, Japan

Table S1 - Mg-concentration in the precursor solution [Mg_{sol}] compared to that measured in the thin films [Mg_{TF}] by energy-dispersive X-ray spectroscopy (EDX) and the corresponding lattice parameters determined from XRD.

[Mg_{sol}]/ %	[Mg_{TF}] / %	c / Å	a / Å
0	0	5.2115	3.2476
5	5.2	5.2074	3.2538
10	11.5	5.2034	3.2554
20	18.1	5.1979	3.2559

Table S2 - Extrapolated band gaps from Tauc-plots for nanoparticulate and thin film MZO depending on the Mg-concentration.

	Band gap / eV	
Mg-content / %	NP	TF
0	3.28	3.27
5	3.35	3.34
10	3.42	3.39
20	3.52	3.50

Table S3 - Absorbance maximum and the calculated values for the quantum efficiency (QE) in the maximum.

	NP		TF		CS	
Mg	abs_{max}	QE_{max} / %	abs_{max}	QE_{max} / %	abs_{max}	QE_{max} / %
0	0.84	71.4	0.16	97.5	1.1	63.5
5	0.83	74.2	0.15	114	1.08	62.5
10	0.83	35.8	0.18	67.9	1.05	56.7
20	0.86	8.8	0.17	24.6	1.11	39.7

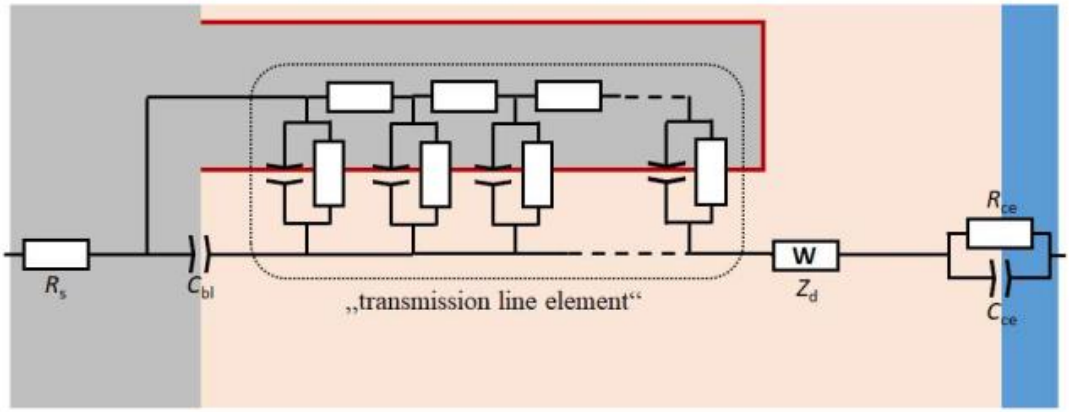

Figure S1 - Equivalent electrical circuit used for the fitting of the EIS data.

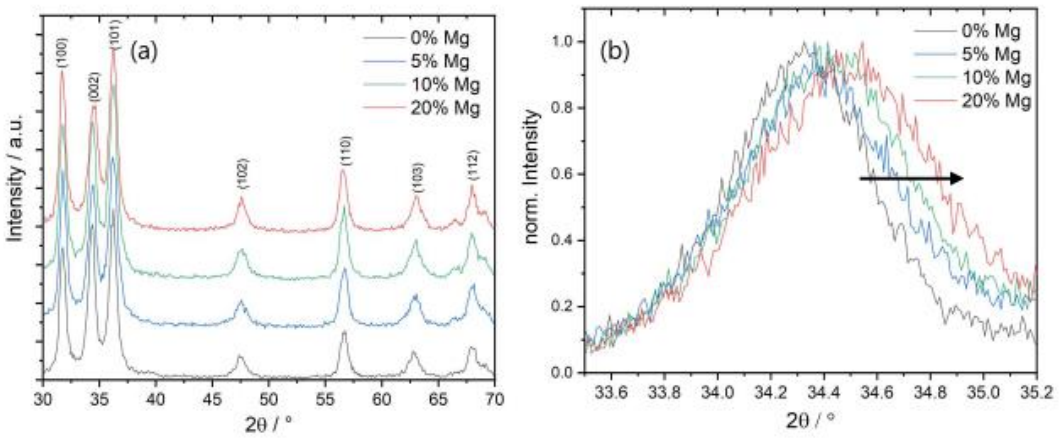

Figure S2 - XRD of MZO TF samples of varying Mg-concentration. (a) overview of MZO TF with 0, 5, 10 and 20% Mg. The typical ZnO wurtzite reflexes are indexed. (b) detail of the (002) reflex and the shift upon Mg-doping towards larger angles is indicated by the arrow.

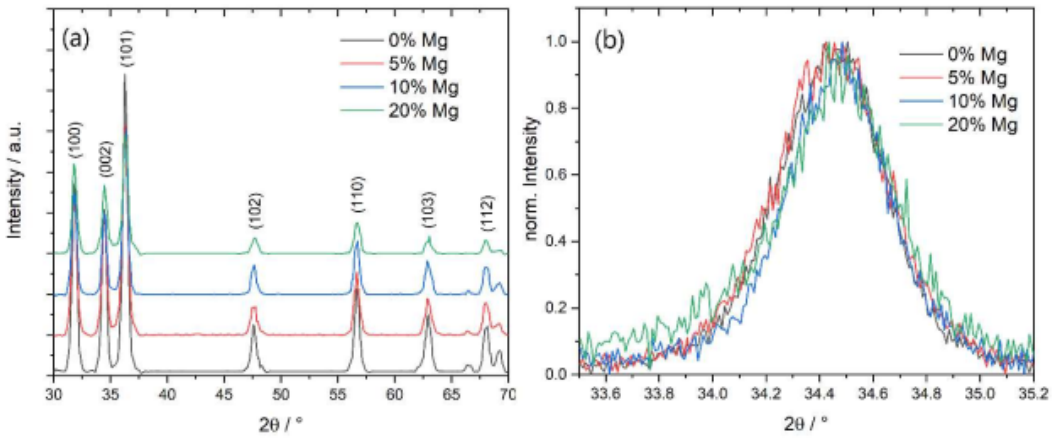

Figure S3 - XRD of MZO CS samples of varying Mg-concentration. (a) overview of MZO CS with 0, 5, 10 and 20% Mg. The typical ZnO wurtzite reflexes are indexed. (b) detail of the (002) reflex which was found at constant angle because it is dominated by the large amount of the undoped ZnO core compared to small contributions by the thin MZO shell.

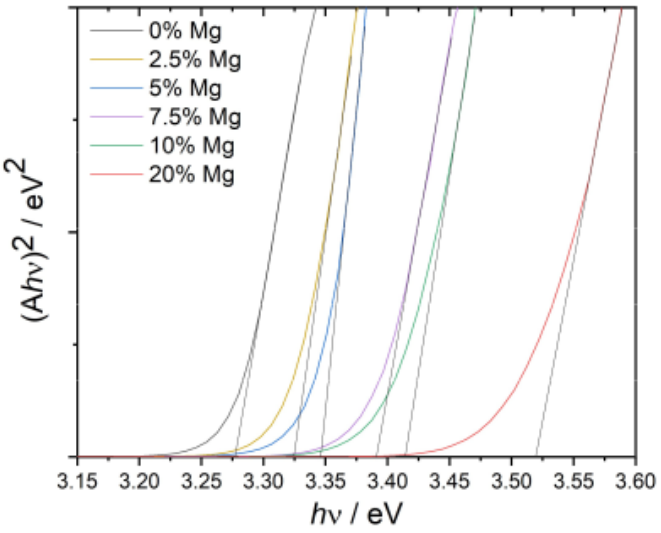

Figure S4 - Tauc-plot of the optical absorption spectra of MZO nanoparticles with varying Mg-concentration with fits to the linear part.

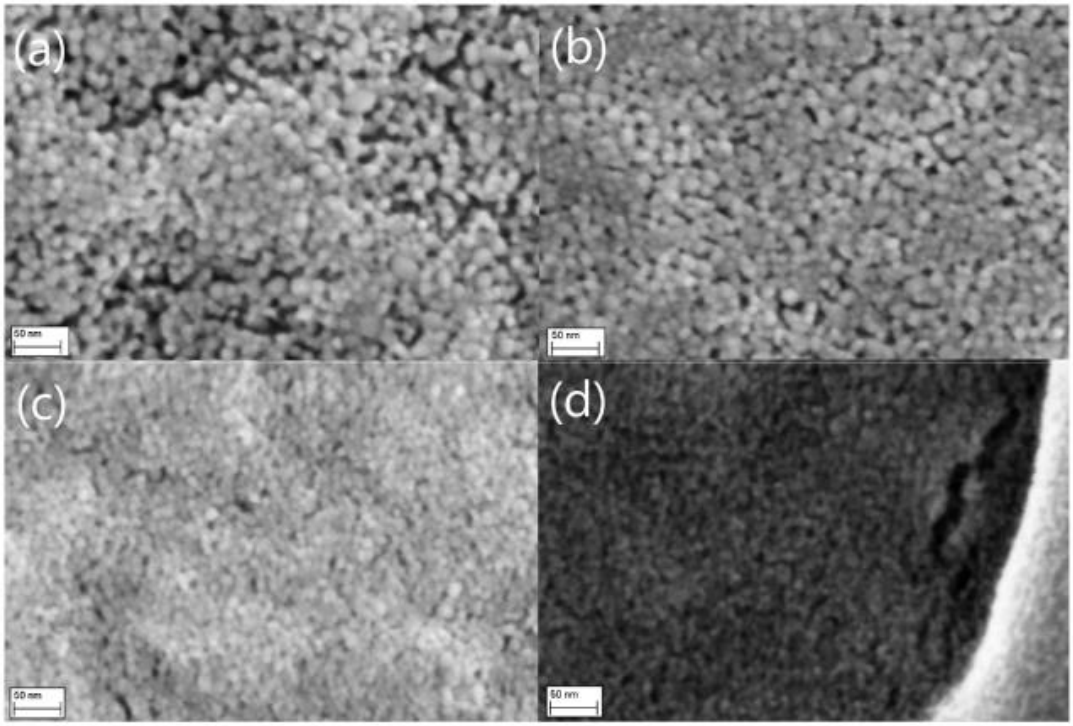

Figure S5 - SEM images of MZO thin films (TF) including (a) 0% Mg, (b) 5% Mg, (c) 10% Mg and (d) 20% Mg at 200k times magnification.

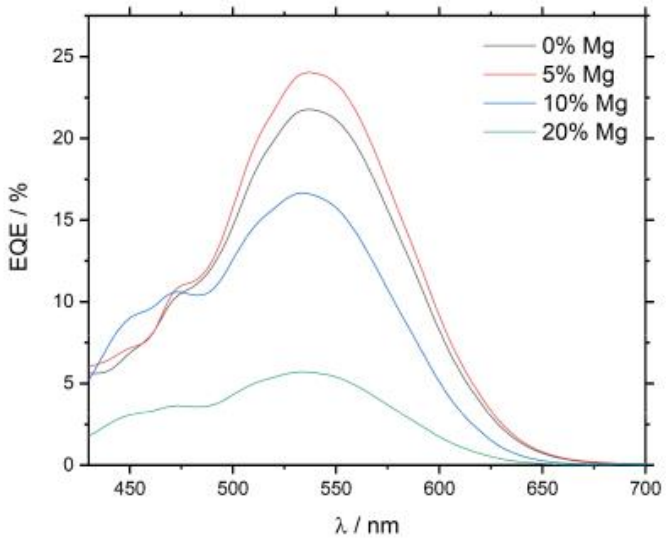

Figure S6 - EQE spectra of TF-type photoanodes of varying Mg-concentrations.

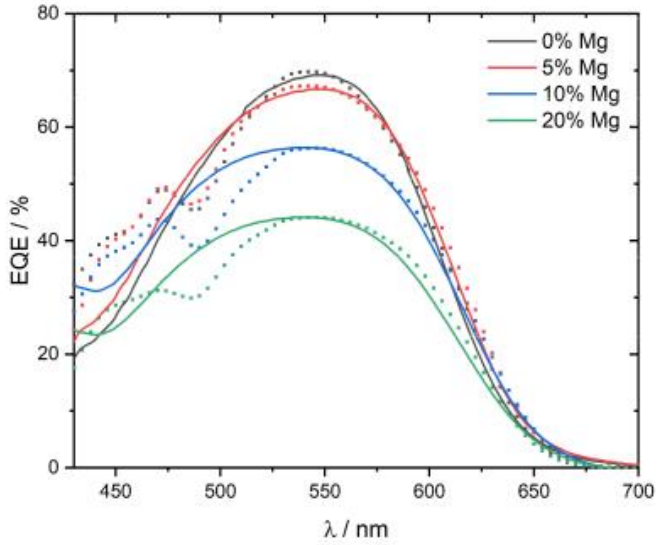

Figure S7 - EQE spectra (dots) and fits (lines) of CS-type photoanodes of varying Mg-concentration.

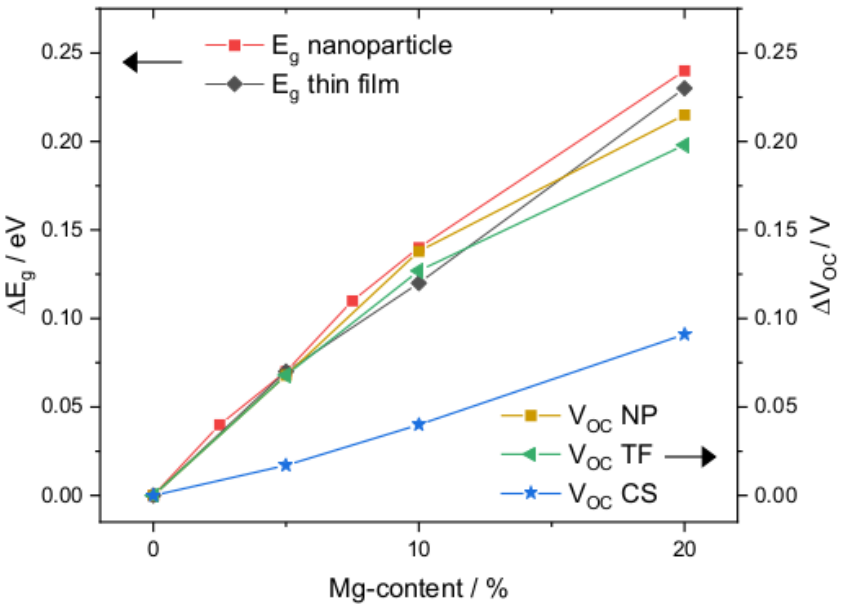

Figure S8 - Comparison between the increase in the band gap ΔE_g determined from optical spectroscopy and the increase in open-circuit voltage ΔV_{OC} caused by Mg-doping compared to pure ZnO.

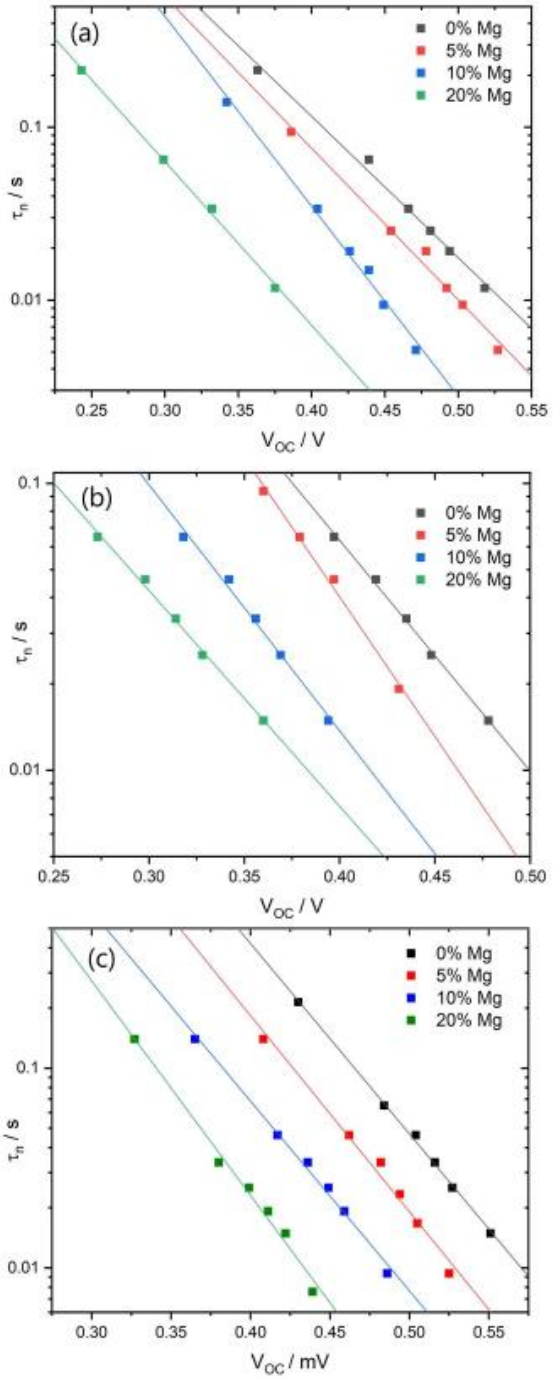

Figure S9 - Electron lifetimes τ_n derived from IMVS measurements at various light intensities for (a) NP-, (b) TF- and (c) CS-type photoanodes. The experimental data for the 5%, 10% and 20% MZO photoanodes has been normalized relative to pure ZnO by the increase of the band gap ΔE_g, as discussed in the text.

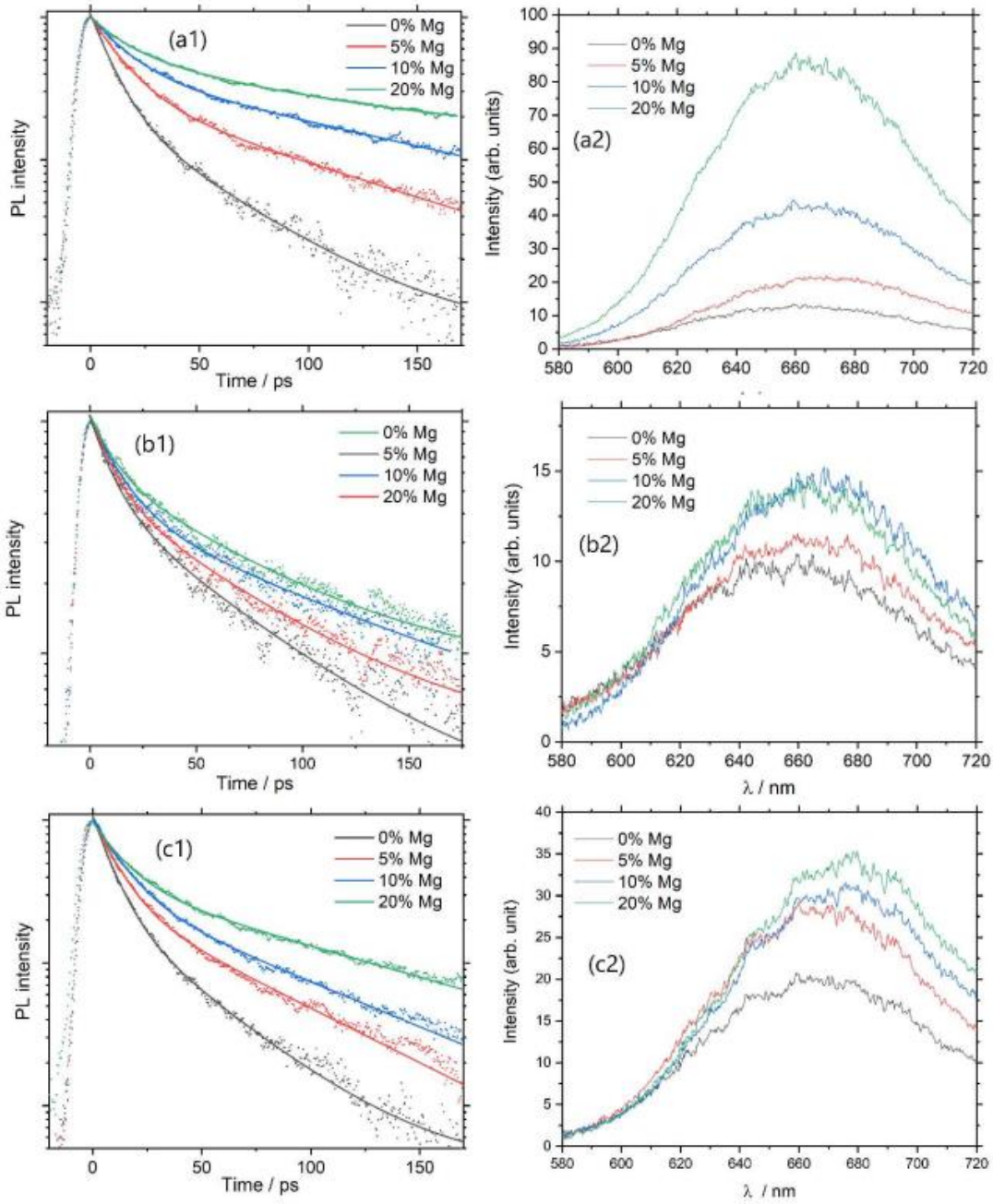

Figure S10 - Bi-exponential fits of the measured TRPL spectra for (a1) NP-, (b1) TF- and (c1) CS-type photoanodes, as well as the integrated PL spectra for (a2) NP-, (b2) TF- and (c2) CS-type photoanodes.

3.1.4 Main Results of Publication (I) in the Context of This Thesis

Publication (I) is divided into two different but intrinsically connected segments. The first part focuses on the fabrication of photoanodes based on MZO. Following the results shown in 3.1.1, MZO nanoparticles with Mg content between 0 and 20% were synthesized through an oxalate intermediate. XRD showed no additional phases appearing after adding Mg^{2+}, highlighting the successful integration into the ZnO wurtzite lattice. As previously shown in the literature, the integration of Mg^{2+} resulted in subtle shifts of the (100) reflex towards lower angles, while the (002) reflex shifted towards higher angles.[157,160] This correlates with changes in the lattice constants in a- and c-direction, directly resulting from the partial replacement of Zn^{2+} by Mg^{2+}. Similar results could be obtained after spin-coating a solution containing the Zn- and Mg-precursor and ethanol amine as a stabilizer and calcinating it at 300 °C. As determined by UV-vis measurements, the resulting MZO thin films exhibited a linear increase in the optical band gap, for Mg concentrations up to 20%. Near identical results could be obtained from the MZO nanoparticles after determining their optical absorbance through diffuse reflectance spectroscopy. Figure **12** showcases the direct connection between the optical band gap determined from Tauc plots and the shifting peak positions of the (100) and (002) reflexes, highlighting the correlation between the structural and optical properties of MZO. Lines between the measurement points in Figure **12** and all following figures are only meant to guide the reader's eye and do not relate to any fits of the data.

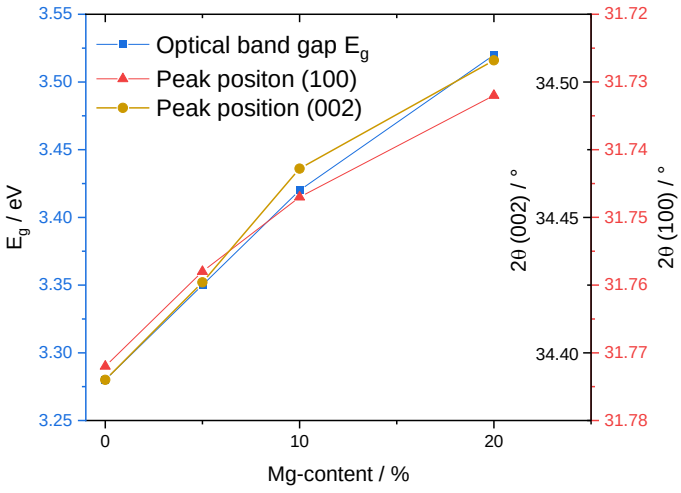

Figure 12. Correlation between structural and optical changes. *Direct comparison between the optical band gap and the positions of the (002) and (100) reflexes of MZO depending on the Mg content, highlighting the correlation between the structural and optical properties of MZO.*

Photoanodes were prepared from pastes, containing the nanoparticles (NP) prepared by wet-chemical synthesis and as thin films (TF) through the drop-casted sol-gel approach. A third type of photoanode was prepared in the form of core-shell particles (CS) with a pure ZnO core and an MZO shell by drop-casting the same precursor solution used to prepare the TF photoanodes on top of already sintered NP-type photoanodes, combining both of the previous approaches. SEM images showed that this approach did not result in a conformal MZO layer, as desired, but rather in a coating of MZO nanoparticles with a size of 1 – 5 nm. While the resulting MZO could not fully cover the surface and prevent contact between the underlying ZnO and the redox electrolyte, it increased the surface area of the photoanode and resulted in higher dye loading after sensitization.

The second part of Publication (I) focused on the photoelectrochemical analysis of the DSSCs, which were prepared from the three types of photoanodes. *I-V* measurements were used to determine the photovoltaic characteristics of DSSCs, including MZO (summarized in Table **1** of Publication (I)). A comparison between the increase in the optical band gap determined from Tauc plots and the increase in V_{OC} of the DSSCs based on the various types of photoanodes is shown in Figure S8 of the electronic supplementary information of Publication (I). For Mg concentrations up to 10%, both values increased nearly identically for the NP and TF architectures, while Mg-concentrations of 20% led to a lower ΔV_{OC} than the respective ΔE_g. Analysis of the results received from EIS measurements indicates that this is caused by a decrease in recombination resistance and subsequent increase in recombination rate with increasing Mg concentration, leading to a deviation from the maximum possible V_{OC}. This result is well in line with previous reports on increased recombination rates in MZO due to increased trap densities and interstitial Mg^{2+} functioning as recombination centers.[32,125] For the DSSCs containing a CS-photoanode, an overall lower increase in V_{OC} was detected. This is primarily the result of the observed inhomogeneous and incomplete coverage of the ZnO surface with MZO.

While the V_{OC}, as expected, increased for all three types of photoanodes, J_{SC} decreased significantly for Mg concentrations above 5%, particularly for the NP- and TF-type cells. Determination of the electron transport resistance R_{tr} through the fitting of the EIS spectra revealed that electron transport was enhanced for cells containing 5% Mg, leading to an overall increased PCE through the addition of Mg to the ZnO-photoanode. Including an element representing R_{tr} in the equivalent electrical circuit is standard for TiO_2-based DSSCs, but typically not needed for ZnO-based DSSCs, due to the much faster electron transport. However, cells with higher Mg content showed significantly increased R_{tr}, slowing electron diffusion

through the porous semiconductor network. This becomes especially visible in the asymmetric shapes of the semicircle attributed to recombination for Mg concentrations above 5% (Figure **7**, Publication (I)). In combination with the increased recombination rates, this led to significantly decreased electron diffusion lengths L and effective electron lifetimes τ_n inside the semiconductor and strongly suppressed J_{SC}. This also highlighted the need to observe both charge transfer processes, electron transport, and recombination, instead of attributing the observed effects to either one or the other, as was done in literature preceding Publication (I).

A possible solution to the significant losses in J_{SC} observed for NP- and TF-type DSSCs was presented in form of the CS-type cells. Since most of the electron transport occurred in the pure ZnO core, R_{tr} was affected to a much lesser degree by the addition of MZO. This resulted in a higher retention of current even at Mg-concentrations above 5% and allowed the cells of the CS-type, in combination with the increased V_{OC}, to increase their PCE considerably (in case of 5% and 10% Mg) or retain it (in case of 20%). While both R_{tr} and R_{rec} were still clearly affected by the addition of MZO to the photoanode, the effect was much diminished compared to the NP-type cells. This is further showcased by the electron diffusion lengths, which increased nearly six-fold for the CS-type cells compared to the NP-type cells.

Time-resolved photoluminescence (TRPL) spectroscopy was performed in the ps time range in collaboration with Marburg University to study the influence of an upward shift of the quasi-Fermi energy E_{fn} on electron injection from the dye to accessible acceptor states in the semiconductor (see Figure **3**). Similar to results observed on simulated shifts of E_{fn}[67,68], all three types of photoanodes showed increased efficient lifetimes of relaxed excited dye states as a result of Mg-doping. However, while electron transfer from these relaxed excited states is most susceptible to shifts of E_{fn} and represents the slowest component of electron injection, it was still completed within 200 ps. Since the majority of electrons are injected faster, in the sub-ps range, it was judged that the influence of Mg-doping on electron injection, and therefore the J_{SC}, was neglectable in comparison to the effects on transport and recombination.[205–207]

3.2 Publication (II): Harnessing the Potential of Porous ZnO Photoanodes in Dye-Sensitized Solar Cells by Atomic Layer Deposition of Mg-doped ZnO

3.2.1 Conclusions from Publication (I) and context for Publication (II)

Publication (I) highlighted the advantages and limitations of the approach to increase the efficiency of ZnO-based DSSCs through doping of the photoanode with Mg. Doping with low concentrations of Mg led to a moderate increase in V_{OC} while retaining or even slightly improving the J_{SC}, resulting in an increased *PCE* overall. Further increasing the doping concentration led to a significant increase in V_{OC}, thus reaching the original goal of this work, but suppressed J_{SC} by up to 75% due to decreased recombination and increased transport resistance. Publication (I) also included a possible solution to this limitation of MZO in the form of a core-shell structure of a pure ZnO core and a doped MZO shell. However, the core-shell structure prepared through sol-gel synthesis did not fully cover the ZnO surface, leading to contact with the redox electrolyte and reduced V_{OC} gains. Publication (II) directly follows the findings of Publication (I) and presents a promising advanced approach to prepare conformal MZO layers inside the porous ZnO structure by the use of atomic layer deposition (ALD).[168] After determination of the growth parameters, ALD enabled precise control over the thickness and composition of the MZO layer through layer-by-layer growth. For the same reasons as described earlier and to highlight the improvements that can be achieved through this approach, the identical dye and redox electrolyte as in Publication (I) were chosen.

ALD of MZO layers was primarily performed by Philipp Klement in the group of Prof. S. Chatterjee. Philipp Klement also performed the determination of ALD growth parameters through XRR, while I characterized the structural and optical properties through XRD, EDS and UV-vis. I prepared DSSCs from the modified photoanodes and performed their photoelectrochemical analysis.

3.2.2 Publication (II)

ACS APPLIED ENERGY MATERIALS

www.acsaem.org Article

Harnessing the Potential of Porous ZnO Photoanodes in Dye-Sensitized Solar Cells by Atomic Layer Deposition of Mg-Doped ZnO

Andreas Ringleb, Philip Klement, Jörg Schörmann, Sangam Chatterjee, and Derck Schlettwein*

Cite This: https://doi.org/10.1021/acsaem.2c02236 Read Online

ACCESS | Metrics & More | Article Recommendations | Supporting Information

ABSTRACT: Mg-doped ZnO (MZO) photoanodes in dye-sensitized solar cells (DSSCs) are intended to increase the open-circuit voltage V_{OC} and boost the power conversion efficiency. However, unintended side effects of the Mg incorporation into ZnO, such as increased transport resistance and recombination rate, commonly outweigh the benefits by reducing the short-circuit current J_{SC}. In this work, we resolve this issue by synergizing the large band-gap energy of MZO with the fast electron transport of ZnO, thus significantly increasing the power conversion efficiency. Atomic Layer Deposition enables the successful fabrication of the required core−shell structures consisting of pure nanoparticulate ZnO films as cores with homogeneous MZO shells. We find a significant increase of the open-circuit voltage, while largely avoiding losses of the short-circuit current. The transport resistance in the cells slightly decreases up to 10 at. % Mg in the shells, and it increases only slightly for Mg concentrations as high as 20 at. %. Our work demonstrates the advantages of mixed architectures consisting of a pure matrix modified by a well-controlled thin active layer. Optimization of cells with such high photovoltages offers a promising pathway toward significantly improved concepts for DSSCs.

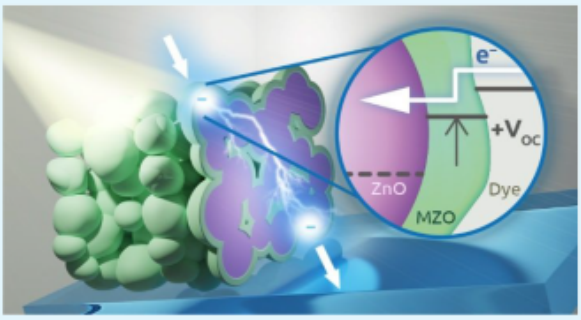

KEYWORDS: *dye-sensitized solar cells, porosity, porous structure, core−shell structure, photovoltaic, MgZnO, MZO, atomic layer deposition*

INTRODUCTION

Dye-sensitized solar cells (DSSCs) have been established as a low-cost alternative for the conversion of solar energy.[1] They are highly efficient under low-intensity illumination while exhibiting lower power conversion efficiencies (PCEs) compared to traditional semiconductor photovoltaics under standard AM1.5G conditions.[2] Breakthroughs in the development of new sensitizers and electrolytes have led to a steady improvement in PCEs.[3,4] To date, TiO_2 represents the most-studied n-type semiconductor for the mesoporous electron transport layer (ETL). ZnO is a viable alternative as ETL, in particular, due to its low processing temperatures for porous crystalline films and its comparably high electron mobility.[5] Although the high electron mobility in ZnO allows for higher photocurrents, ZnO-based DSSCs generally tail TiO_2-based cells in open-circuit voltage V_{OC} and fill factor FF. Even though V_{OC} can be increased in TiO_2-based cells by additives to the redox electrolyte such as Li^+ and *tert*-butylpyridine (TBP),[6−8] such additives are less efficient in ZnO-based cells. So far, no efficient alternatives have been developed.[9,10] Moreover, ternary metal oxides such as $ZnTiO_3$,[11] $SrTiO_3$,[12] and Zn_2SnO_4[13] have been considered, aiming to combine the advantages of the respective binary metal oxides. However, these attempts mainly led to additional complications caused by significant differences in the crystal structures.

In contrast to that, Mg-doped ZnO (MZO) is based on the cationic substitution of Zn^{2+} ions with Mg^{2+} ions within the ZnO crystal structure. High-quality MZO can be prepared by means of various approaches, including radio frequency sputtering,[14] molecular-beam epitaxy,[15] pulsed-laser deposition,[16] chemical-vapor deposition,[17] or atomic layer deposition (ALD).[18,19] Through atomic-level thickness control, high uniformity, and high conformity, the latter allows for the layer-by-layer growth of thin films.[20] The ALD process relies on the alternate and sequential exposure of the substrate to two or more vapor-phase precursors that react in self-limiting surface reactions between the functional groups on the substrate and the vapor-phase precursors. Coating of complex inner surfaces, even in porous thin films and nanocomposites, renders ALD superior compared to competing coating

Received: July 15, 2022
Accepted: November 8, 2022

methods.[21,22] Those advantages have led to widespread applications in photovoltaics where ALD is used for the growth of passivation layers, passivating contacts, transparent conductive oxides in collectors, and protective layers in perovskite solar cells,[23−25] tandem solar cells,[26−28] and DSSCs[29−34] as well as other applications.[35−38] One approach for expanding the regular two-step ALD cycle toward advanced materials like ternary oxides consists of the use of supercycles. In this approach, two regular two-step ALD cycles are alternated and repeated to produce multilayered or mixed, multinary thin films. The cycle ratio and the sequence of cycles tune the composition of the material. In this way, homogeneous MZO thin films can be prepared by a regular alternation of MgO and ZnO ALD cycles.[18,19] Up to 33 at. % (shortened to % from here on) Mg^{2+} ions can be integrated while retaining the wurtzite crystal structure of ZnO based on the similar ionic radii of Mg^{2+} (0.60 Å) and Zn^{2+} (0.57 Å).[39] Though the difference in size may be small, it nevertheless results in subtle changes of the lattice constants between ZnO and MZO, leading to a near-linear increase of the optical band gap energy with increasing Mg content. This is largely caused by an upward shift of the conduction band edge energy E_{CB}.[40] The tunable band structure of MZO sets it apart from other transition metal doped ZnO layers deposited by ALD, such as Co-, Ni-, or Fe-doped ZnO, which have shown promise in photocatalytic applications.[38] The increased band gap of MZO has led to its use as ETL in photovoltaic cells, notably perovskite solar cells,[41,42] quantum dot solar cells,[43] and organic solar cells.[44,45] Despite the different band position, MZO did not affect the V_{OC} in these cells but rather served to increase the J_{SC} for Mg concentrations of up to 25%.[46] In DSSCs, however, the shift of E_{CB} and the related quasi-Fermi energy $E_{F,n}$ translates into a significant increase in V_{OC}.[46,47] Additionally, low Mg concentrations of up to 5% result in an increase in J_{SC} based on low transport resistance.[46] While higher Mg concentrations of up to 20% still leads to greatly improved V_{OC} compared to pure ZnO, they cause a sharp increase in transport resistance and electron recombination, leading to a reduced J_{SC}, offsetting the advantage gained by greatly increased V_{OC}. Experiments with a shell of MZO nanoparticles on ZnO cores show reduced losses of J_{SC} compared to homogeneously doped nanoparticles, while, however, featuring a smaller increase of V_{OC}.[46]

In this work, we synergize the large band gap energy of MZO with the fast electron transport of ZnO. We improve the conventional core−shell approach by the first reported instance of a photoanode prepared from homogeneous and conformal MZO ALD coating of a porous ZnO layer. The prepared core−shell structure represents a novel approach to increase performance in ZnO-based DSSC through the combination of pure and doped ZnO. The precise control of the ALD process enables MZO layers with well-defined thicknesses and Mg concentrations to optimize cell performance. V_{OC} is higher than previous results on ZnO- or even TiO_2-based DSSCs. We show a significant increase in V_{OC} compared to previously reported cells based on solution-processed ZnO-MZO. Furthermore, any losses in J_{SC} caused by an increased transport resistance are minimized, leading to overall increased PCEs when ALD-processed MZO shells are used. Our work demonstrates the advantages of mixed architectures consisting of a pure matrix modified by a well-controlled thin active layer. Optimization of cells with such high photovoltages offers a promising pathway toward significantly improved concepts for DSSCs.

EXPERIMENTAL SECTION

Fluorine-doped tin oxide (FTO, Kaivo, <15 Ω cm^{-2}) glass substrates were subsequently cleaned with RBS solution (Roth), acetone, and isopropanol in an ultrasonic bath for 15 min each. The ZnO paste was prepared by mixing ZnO nanoparticles (14 nm, PlasmaChem), α-terpineol, ethylcellulose, and ethanol at a weight ratio of 2:7:1:9. The paste was screen-printed onto the cleaned FTO substrate in the shape of round spots with a radius of 3 mm and subsequently annealed at 420 °C for 60 min in air.

MZO thin films were deposited on the ZnO nanoparticulate films in a commercial thermal ALD system (PicoSun R200 Standard) at a reactor temperature of 200 °C. Bis(ethylcyclopentadienyl)magnesium ($(EtCp_2)Mg$, min 98%, Dockweiler Chemicals), Diethylzinc (DEZ, min 95%, Strem Chemicals), and deionized water (DI-H_2O) were used as Mg, Zn, and O sources, respectively. $(EtCp_2)Mg$ was heated to 130 °C to increase its vapor pressure, while DEZ was kept at room temperature. Each ALD cycle followed a [metal precursor−purge−H_2O−purge] timing sequence. For a single optimized MgO ALD cycle, and $(EtCp_2)Mg$ and DI-H_2O were pulsed for 0.1 and 0.2 s, respectively, while each precursor pulse was followed by 5 s of purging with Ar. For a single optimized ZnO ALD cycle, DEZ and DI-H_2O were pulsed for 0.2 and 2.0 s, each, both followed by 5 s of Ar purging. MZO thin films were deposited by combining individual MgO and ZnO ALD cycles to a supercycle of the form $[y((EtCp_2)Mg + H_2O) + z(DEZ + H_2O)]$. The ratio of y/z controls the Mg and Zn contents, while the total number of supercycles determines the film thickness; y ranged 0−3 integer, and z ranged 0−12. The growths-per-cycle of MgO and ZnO were 1.04 and 1.79 Å $cycle^{-1}$, respectively. For example, a supercycle with $y = 3$ and $z = 7$ yields Mg and Zn contents of 0.2 and 0.8, respectively, and the growth-per-supercycle is 15.7 Å/supercycle.

We determine the MZO film thickness through comparison with a reference film grown on a Si substrate (⟨100⟩ with a 275 nm thick wet-thermal oxide layer) that was placed in the ALD reaction chamber, together with the nanoparticulate ZnO film. The film thickness results from the X-ray reflectivity (XRR) measured with a Siemens/Bruker D5000 X-ray diffraction system and a subsequent fit of the reflectivity, as described in ref 48. X-ray diffraction (XRD) of the 50 nm thick MZO layers of varying Mg content deposited on silicon wafers was performed by use of Cu Kα radiation (X'Pert Pro MRD). Optical absorption spectra were recorded in ambient air in transmission by a PerkinElmer Lambda 365 spectrophotometer. Scanning electron microscopy (SEM) images were taken on a Zeiss MERLIN microscope with an acceleration voltage of 3 kV and an emission current of 100 pA. Energy-dispersive X-ray spectroscopy (EDS) mapping was performed with an X-Max 50 detector at 10 kV and 2 nA.

Before sensitization, all samples were heated to 420 °C in air for 30 min. They were subsequently immersed in a 0.5 mM solution of the indoline dye DN216 (Chemicrea) and 0.2 mM lithocholic acid in 1:9 (v/v) ethanol/chloroform for 60 min. Platinized counter electrodes were prepared by drop-casting a 5 mM solution of chloroplatinic acid in ethanol onto a cleaned FTO substrate and heating it to 420 °C for 15 min. Both electrodes were connected and sealed by a hot-melting spacer (Surlyn, 25 μm). The electrolyte was injected through a predrilled hole in the counter electrode, which was then sealed by UV-light curing glue (ThreeBond 3035B) and a glass coverslip. The electrolyte consisted of 0.5 M PMII (3-propyl-1-methylimidazolium iodide) and 0.05 M I_2 in acetonitrile. Four specimens were prepared for each cell configuration. All chemicals and solvents were used as received from Sigma-Aldrich unless mentioned otherwise.

UV−vis spectra of the sensitized photoanodes were measured in reflection, using an integrating sphere (getProbe, 5393 SET, getAMO) and a Tec5 diode array spectrometer. Photoelectrochemical characterization was carried out for one given set of samples using an IM6 potentiostat and a CIMPSpcs system (Zahner Elektrik). $I-V$

https://doi.org/10.1021/acsaem.2c02236
ACS Appl. Energy Mater. XXXX, XXX, XXX−XXX

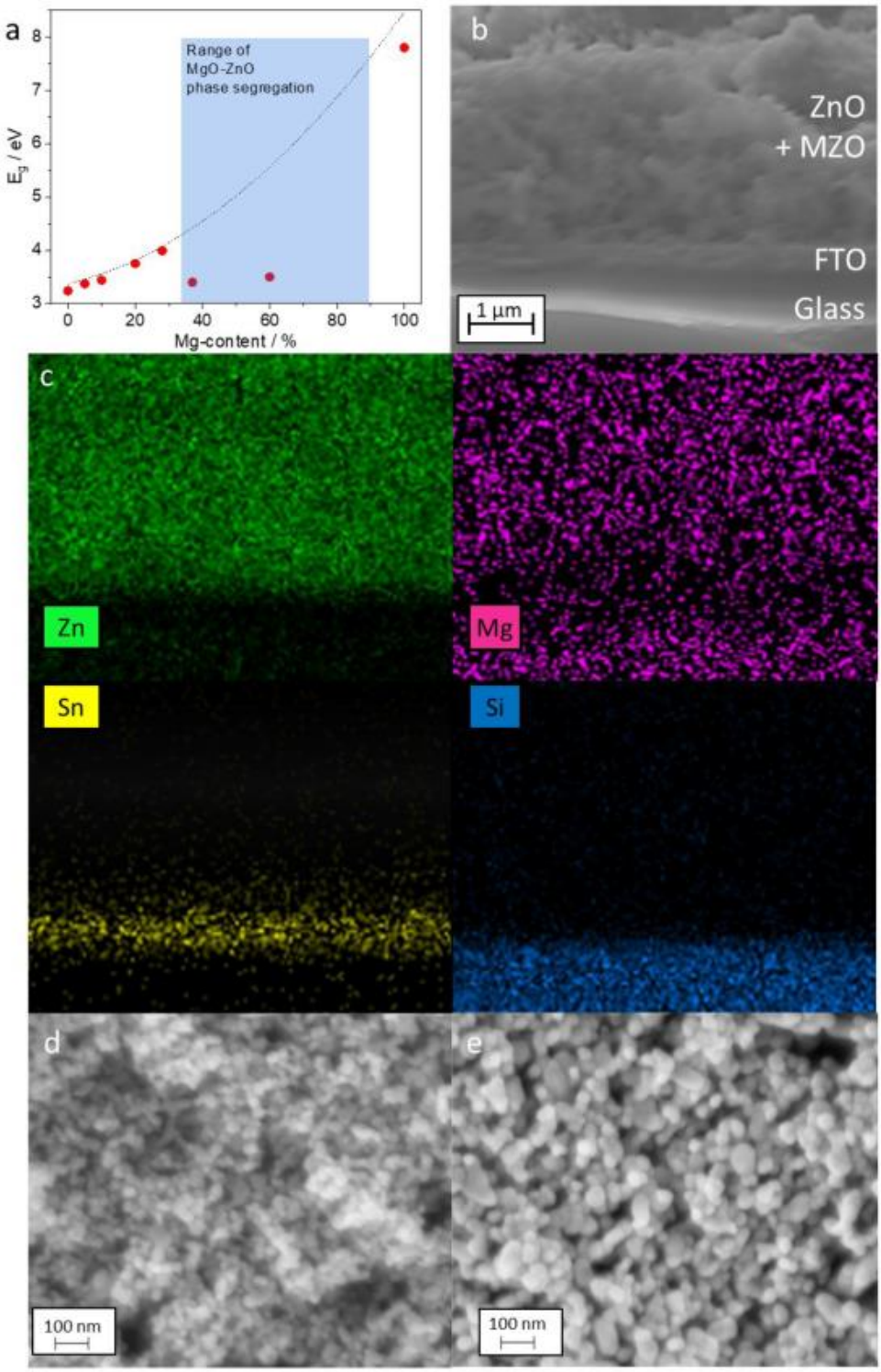

Figure 1. (a) Band-gap energies determined from Tauc plots for 50 nm thick ALD-deposited MZO layers of varying Mg content on FTO. (b) Cross-section SEM image and (c) corresponding EDS maps of a nanoparticulate ZnO layer on FTO-coated glass after deposition of 5 nm MZO with an Mg concentration of 20%. (d) Top-view SEM images of nanoparticulate ZnO films before and (e) after ALD deposition of a MZO layer with 5% Mg and a thickness of 5 nm.

curves were measured in the dark and under simulated solar light provided by an LS0106 xenon arc lamp with an LSZ189 AM 1.5G filter with an intensity set to 100 mW cm^{-2} on a calibrated ML-020VM pyranometer (EKO Instruments). External quantum

https://doi.org/10.1021/acsaem.2c02236
ACS Appl. Energy Mater. XXXX, XXX, XXX−XXX

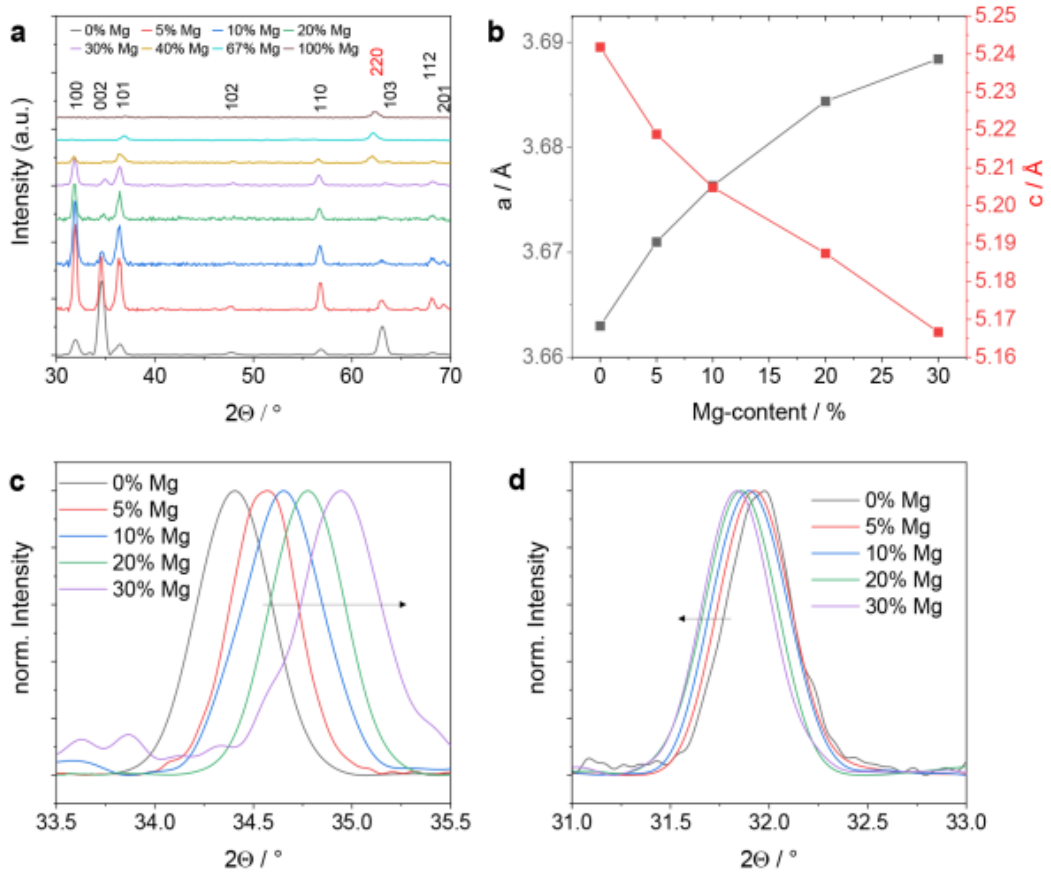

Figure 2. (a) XRD patterns of ALD-deposited MZO layers with varying Mg concentration. The reflexes *hkl* characteristic of the lattice planes (*hkl*) of wurtzite ZnO (black) and cubic MgO (red) are indicated. (b) Lattice constants in *a*- and *c*-directions calculated from peak positions. Detailed XRD patterns of the 002 (c) and 100 (d) peaks of MZO layers. The peak position shifts due to changes in the lattice constants with increasing Mg content.

efficiency (EQE) yielding the product of wavelength-dependent light-harvesting, electron injection, dye regeneration,, and electron collection efficiencies was measured under illumination by a white-light source and a monochromator (TLS02, Zahner Elektrik) at a fixed intensity of 10 mW cm^{-2} with an amplitude of 100 mA at a frequency of 1 Hz. Electrochemical impedance spectroscopy (EIS) was performed with an amplitude of 0.05 V in a frequency range of 1 MHz to 0.5 Hz under illumination by a 510 nm LED at 30 mW cm^{-2}, while the DSSCs were kept at open-circuit bias. The resulting impedance spectra were analyzed with RelaxIS 3 (rhd instruments). Intensity-modulated photocurrent spectroscopy (IMPS) was performed at short circuit under illumination by a 510 nm LED at intensities between 30 and 1 mW cm^{-2}.

RESULTS AND DISCUSSION

We initially optimized the respective MgO and ZnO ALD processes on SiO_2/Si substrates to ensure self-limiting surface reactions with precise thickness control and optimal uniformity[20] and conformity (Supporting Information (SI) Figures S1–S3) before transferring this set of process parameters to the porous nanoparticulate ZnO electrodes. Therefore, we assessed the function of the supercycle approach by depositing 50 nm thick MZO films with varying Mg concentrations on glass substrates and determined the band-gap energies from UV–vis measurements (see SI Figures S4 and S5). The measured band gap energies prove the successful incorporation of Mg into ZnO and validate the calculated Mg concentrations from the supercycle approach. MZO thin films (Figure 1a) range in Mg concentrations of 0–28% with band gap energies ranging from 3.24 (ZnO) to 3.99 eV ($Mg_{0.28}Zn_{0.72}O$). The latter follows the trend predicted by Grundmann et al.[49] with a miscibility gap between Mg contents of 33–85%. Phase segregation into wurtzite ZnO and cubic MgO is well-known to occur in this gap, explaining the reduction in band-gap energy beyond 28%.[39,50,51] It has previously been reported that the increase is achieved largely through a shift of the conduction band edge E_{CB}, while the valence band edge E_{VB} is affected to a much lesser degree.[52,53] We observed that the band-gap energy of the deposited MZO is solely dependent on the Mg concentration and shows only minor changes after subsequent annealing (Figure S5, SI). This suggests that the optical properties of MZO and, hence, the short-range order of the material in the intended mixture is already established during MgO and ZnO growth at 200 °C. Moreover, we observed a blue shift of the band gap of ALD-deposited MZO compared to homogeneously doped nanoparticles of similar size[46] (15–20 nm), which we attribute to the improved purity of the material. EDS mapping shows the superior conformity of ALD (Figure 1b). The cross-section of the nanoparticulate ZnO layer after deposition of 5 nm of MZO shows the homogeneous distribution of Mg throughout the entire layer. As expected for commercial glass samples, Mg

https://doi.org/10.1021/acsaem.2c02236
ACS Appl. Energy Mater. XXXX, XXX, XXX–XXX

is also detected in the FTO-coated glass substrate (Figure 1c). ALD homogeneously coats the entire porous ZnO structure with MZO without agglomerations or holes, which represents a significant improvement over solution-based approaches. This is important as it prevents the electrical contact of the liquid electrolyte with the underlying ZnO. SEM images of the photoanodes before and after MZO deposition additionally display the homogeneous MZO coating of the ZnO nanoparticles. While the average nanoparticle diameter initially (Figure 1 d) fits the expected 14 nm, it increases significantly as a consequence of a conformal deposition of a 5 nm thick MZO layer (Figure 1e). This also leads to a merge of several particles to form connected nanoparticles and, thereby, slightly decreases the overall sample surface area due to a lower pore volume. However, the particle shape is preserved as ALD reproduces the surface shape, which is in stark contrast to solution-based approaches. The latter typically results in the deposition of many, much smaller nanoparticles on the substrate surface, making dense coatings difficult to achieve.[46]

XRD measurements reveal the crystal structure of MZO layers deposited by ALD. All reflexes shown in Figure 2a only appear after the additional annealing step at 420 °C for 60 min. This indicates an amorphous state after ALD, which transitions to a microcrystalline state after annealing. The overview XRD patterns of samples containing 0−30% Mg exhibit all the characteristic reflexes of hexagonal wurtzite ZnO (ICDD 36-1451). However, layers of pure ZnO display a strongly preferred orientation with their *c*-plane (characterized by 002) parallel to the substrate surface. This preferred orientation changes toward an orientation of crystals with (100) parallel to the substrate surface with increasing Mg concentration.[46] The size of the crystalline domains calculated from the 100 and 002 peaks using the Scherrer equation is approximately 20 nm for samples with up to 30% Mg. For samples containing 40% Mg and higher, an additional peak is found at 62°. This perfectly fits the 220 reflex of cubic MgO (ICDD 78-0430). The change in relative peak intensities and the decrease in overall intensity with increasing Mg concentration as well as the low signal of the cubic MgO phase match previous reports in the literature.[18,19,54]

The normalized XRD patterns of the 002 (Figure 2c) and 100 (Figure 2d) reflexes reveal the effect of Mg^{2+} integration into the hexagonal ZnO lattice. The small difference in size between the Mg^{2+} and the Zn^{2+} ions leads to a change in the lattice constants in the *a*- and *c*-directions (Figure 2b), which can be calculated from the shift of the respective XRD peaks with increasing Mg content.[39,40,46,55] This confirms that Mg^{2+} is integrated into the ZnO lattice during the deposition and leads to the desired lattice distortion. The constant fwhm of the reflexes in Figure 2c,d indicates one given lattice constant and, hence, one given homogeneous Mg concentration in each of the MZO layers. XRD patterns of combined MZO-ZnO core−shell layers after annealing (Figure S6, SI) are dominated by ZnO signals, independent of the Mg concentration of the deposited MZO layer. This indicates that no significant amounts of Mg have diffused into the ZnO core during the heat treatment, which fits previous reports that Mg diffusion only starts to occur at temperatures above 800 °C.[56]

Photoanodes of nanoparticulate ZnO with an MZO layer thickness of 5 nm and varying Mg concentrations were prepared and used in DSSCs in conjunction with the iodide/triiodide electrolyte. The working principle of the cells is shown in Figure 3. Following light absorption by the dye

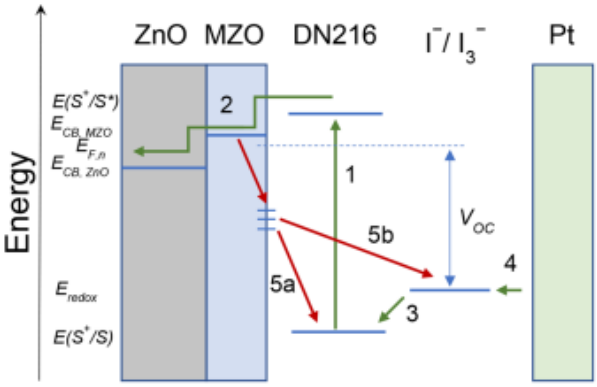

Figure 3. Schematic energy level diagram indicating the main electron pathways. An electron is excited in the dye DN216 upon absorption of a photon (1). It is injected into the MZO and diffuses through the shell into the ZnO core (2). The dye is regenerated by the iodide electrolyte (3), which is reduced at the Pt counter electrode (4). Recombination can occur through surface trap states into the dye (5a) or the electrolyte (5b). The V_{OC} of the cell is limited by the difference of the redox energy level of the electrolyte and the quasi-Fermi energy level of the MZO.

(process 1), electrons are injected to the MZO layer (process 2), defining the photovoltage V_{OC}. These electrons are then transported into ZnO and to the back electrode. Dye regeneration by hole transfer to the redox mediator (process 3) and reduction of the latter (process 4) completes the circuit. Recombination reactions of injected electrons (presumably relaxed into trap states) to either the dye (process 5a) or the redox mediator (process 5b) have to be considered as main loss processes. Additives to the electrolyte, such as Li ions and 4-*tert*-butylpyridine (TBP), which are commonly used to suppress recombination and to increase V_{OC}, were purposely not used in this study. These additives show significantly different results in ZnO-based DSSCs compared to TiO_2-based DSSCs and their interaction with MZO has not yet been studied. We avoided such uncontrolled influences to not blemish the effect of Mg-doping.

Figure 4a shows the expected characteristics of well-functioning DSSCs. The prepared DSSCs containing MZO-covered ZnO exhibit a significant increase in V_{OC} with increasing Mg content. This is the result of an upward shift in the quasi-Fermi level $E_{F,n}$, similar to results previously reported for fully doped MZO nanoparticles and a solution-based core−shell approach.[46] Between the DSSCs containing an ALD-deposited pure ZnO layer (V_{OC} = 577 mV) and the cells containing 20% Mg (V_{OC} = 740 mV), an overall increase in V_{OC} (ΔV_{OC} = 163 mV) is achieved. This increase is significantly higher than that for the solution-based core−shell approach (ΔV_{OC} = 91 mV),[42] showing that a homogeneous conformal coating is much more beneficial for establishing the full potential difference between MZO and the electrolyte redox potential by avoiding leaks through exposed uncoated ZnO. The inset in Figure 4a shows the dark currents after correction by the observed difference in V_{OC}, revealing increasing recombination currents with increasing Mg concentration, which will be analyzed in detail. We observe a slight decrease in J_{SC} after deposition of a pure ZnO thin film on the ZnO nanoparticles. This is caused by a decrease in surface area and, subsequently, a decrease in dye loading on the photoanode (see Figure S8, SI). All other cell parameters

https://doi.org/10.1021/acsaem.2c02236
ACS Appl. Energy Mater. XXXX, XXX, XXX−XXX

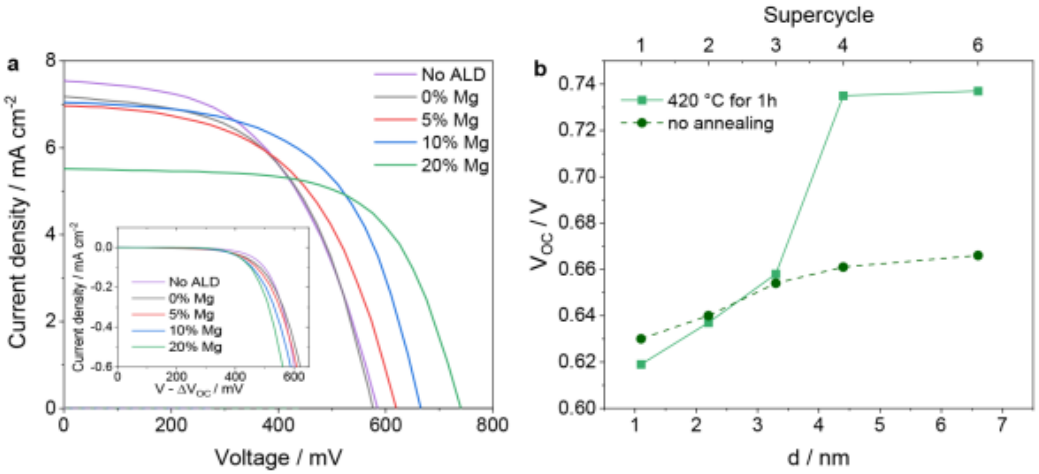

Figure 4. (a) $I-V$ curves of DSSCs with photoanodes containing a 5 nm thick MZO shell of varying Mg content around pure ZnO nanoparticles. The inset shows the respective dark currents plotted against the voltage corrected by the observed difference in V_{OC}. (b) Thickness dependence of V_{OC} on the thickness d of the deposited MZO layer with 20% Mg content before and after annealing.

of these two cell types are similar (see Table 1). Therefore, the subsequent photoelectrochemical analysis focuses on DSSCs containing ALD layers of different Mg contents.

Table 1. Photovoltaic Characteristics of the DSSCs after Deposition of 5 nm MZO Layers of Varying Mg Contents

Mg Content/%	J_{SC}/(mA cm^{-2})	V_{OC}/mV	FF	PCE/%
No ALD	7.54	580	0.52	2.27
0	7.18	577	0.54	2.24
5	6.97	620	0.54	2.33
10	7.05	665	0.56	2.63
20	5.52	740	0.63	2.57

We deposited layers with varying numbers of supercycles on pure ZnO nanoparticles to determine the minimum layer thickness d of the deposited MZO layer needed to provide the optimum increase of V_{OC}. This series was performed for DSSCs containing 20% Mg because these are most strongly affected by the Mg doping. The V_{OC} of the respective DSSCs prepared from these photoanodes are shown in Figure 4b. The corresponding $I-V$ curves are given in Figure S9, SI. V_{OC} starts to increase already after 1 supercycle but 4 supercycles (4.4 nm) are needed to fully establish the electrode kinetics characteristic for the covering layer of MZO. Therefore, a thickness of about 5 nm (Table S2, SI) was chosen for all subsequent experiments. A quantum-sized effect toward an increased band gap at smaller thickness as perhaps expected based on earlier work on nanocrystals[57,58] cannot be claimed from the present data since it should lead to an opposite trend in V_{OC} to that observed here. The observed increase of V_{OC} occurs following an annealing step at 420 °C in air after the deposition of MZO by ALD, and the V_{OC} values are considerably smaller without this heat-treatment step (Figure 4b). As previously shown, the optical band gap energy of the deposited MZO layer is not affected by this heating step, unlike the long-range order inside the layer which increases by thermal annealing. This increase in crystallinity of the MZO is highly beneficial for the V_{OC}, likely through the reduction of surface trap states which would result in less recombination. Further, the increase in the V_{OC} will always be smaller than the observed increase in the optical band gap, due to a partial shift also of the valence band, recombination of electrons to the redox electrolyte, and, hence, a position of $E_{F,n}$ below E_{CB}. In addition to the increasing V_{OC}, the $I-V$ curves (Figure 4a) reveal a stable J_{SC} of around 7 mA cm^{-2} for all cells up to an Mg concentration of 10%. Only the cell containing 20% Mg shows a drop in J_{SC} to 5.52 mA cm^{-2} (Table 1). This is a remarkable improvement compared to previous reports of DSSCs including MZO, in which already small Mg concentrations above only 5% resulted in a significant loss of current.[46,47] This loss was attributed to changes in the transport resistance in MZO which decreased for up to 5% Mg content but strongly increases with the addition of more Mg^{2+}. Here, thanks to a homogeneous coating by ALD, J_{SC} remains stable for 10% Mg, and the loss even at 20% Mg is significantly reduced, indicating that the use of pure ZnO as a core for electron transport is very promising. The observed increase in FF, especially for the cell containing 20% Mg, is likely a result of the decreasing J_{SC} and not directly related to the increased Mg concentration.

We measured the external quantum efficiency (EQE) of the DSSCs under short-circuit conditions, often also referred to as incident-photon-to-current efficiency (IPCE). It largely follows the absorption spectrum of the adsorbed dye (Figure S8, SI), apart from deviations around 480 nm, which are likely caused by fluctuations in the effective illumination intensity (interference, scattering) in this range. With a peak of 78% EQE around 540 nm for the cell without Mg, 76% for the cells including 5% or 10% Mg, and 59% for the cell including 20% Mg (see Figure 5), the integrated J_{SC} match the J_{SC} measured in the $I-V$ curves (Figure 4).

A reduced EQE and J_{SC} as found for the DSSC containing 20% Mg can be caused by either reduced light harvesting, slower electron injection, slower dye regeneration, or a decreased electron collection efficiency. In the present case, a lower light-harvesting efficiency can be excluded as a possible cause as all cells show a near-identical UV–vis absorption spectrum independent of the respective Mg concentrations (Figure S8, SI). Changes in the injection efficiency can be excluded as the main reason since most charge carriers are injected sufficiently fast into MZO, despite subtle changes in

https://doi.org/10.1021/acsaem.2c02236
ACS Appl. Energy Mater. XXXX, XXX, XXX−XXX

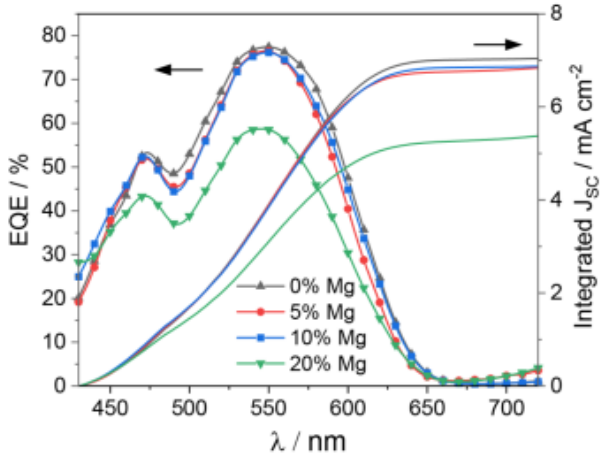

Figure 5. External quantum efficiency (EQE) of the DSSCs containing varying Mg concentration in a 5 nm thick MZO shell. The solid lines show the corresponding integrated photocurrent calculated from the EQE.

the injection kinetics from relaxed excited dye states.[46,59] While injection from relaxed excited states into the semiconductor was slowed in the 100 ps range, the majority of charge carriers was injected in the low- or sub-ps range.[60] Differences in dye regeneration efficiency can also be neglected since all cells contained the identical dye and redox electrolyte. A reduced collection efficiency is, thereby, identified as the most relevant origin of the observed decrease in current. Electron transport and recombination were, therefore, studied in detail and will be discussed in the following.

We studied the charge-transfer processes inside the DSSCs by electrochemical impedance spectroscopy (EIS). Remarkably, we found none of the typical indicators of an increased transport resistance,[61−63] such as a 45° slope in the high-frequency range or an asymmetry of the corresponding semicircle in the Nyquist plot of the measured spectra (Figure 6). A rather basic electrical equivalent circuit (Figure 6) fits the measured spectra. It consists of the series resistance R_S, the recombination resistance R_{rec}, the trap capacitance C_t, the charge-transfer resistance R_{CE}, and capacitance C_{CE} representing the counter electrode. The model is free of transport resistance which is typically needed in the transmission line model for TiO_2-based DSSCs as well as in earlier studies of MZO-based nanoparticulate cells.[46,64,65] Additionally, there is no diffusion resistance of the electrolyte, which is often the case for I^-/I_3^--based redox electrolytes, since we find no corresponding semicircle at low frequencies (Figure 6, right). The resulting series resistance (R_S), recombination resistance (R_{rec}), and electron-transfer resistance at the counter electrode (R_{CE}) fitting the measured EIS spectra are given in Table 2.

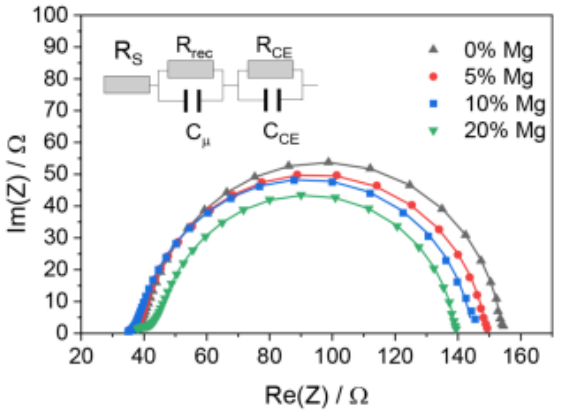

Figure 6. Nyquist plot of the electrochemical impedance spectroscopy (EIS) measurements of DSSCs with a varying Mg concentration (symbols) and the corresponding fits (lines) at 30 mW cm^{-2} illumination by a 510 nm LED. The inset shows the equivalent electrical circuit used to fit the measured spectra.

Table 2. Series Resistance (R_S), Recombination Resistance (R_{rec}), Trap Capacitance (C_t), and Electron-Transfer Resistance (R_{CE}) and Capacitance (C_{CE}) at the Counter Electrode Resulting from Fitting the Measured EIS Spectra

Mg Content /%	R_S/Ω	R_{rec}/Ω	C_t/μF	R_{CE}/Ω	C_{CE}/mF
0	34.84	110.82	162	15.45	3.55
5	35.27	106.69	366	14.71	3.50
10	34.29	101.67	426	12.41	3.97
20	38.01	91.88	552	12.97	3.93

As expected, all cells show R_S, R_{CE} and C_{CE} independent of the Mg content of the photoanode, speaking in favor of a uniform fit quality. R_S is increased from the resistance of the FTO surface (<15 Ω cm^{-2}) due to nonideal contacting of the electrode. The Nyquist plots (Figure 6) are dominated by the semicircles corresponding to the recombination resistances R_{rec}, which decrease with increasing Mg concentrations. This is exactly in line with previous findings of an increased recombination probability in DSSCs containing MZO.[46,47] It is attributed largely to the incorporation of Mg^{2+} ions at interstitial sites, which act as traps and recombination centers.[66] This is further supported by the findings of increasing C_t with increasing Mg concentration at the probed $E_{F,n}$, seen in Table 2. An increased recombination rate also fits a less pronounced increase in V_{OC} with increasing Mg concentration, compared to the observed increase in the optical band gap. Fitting the data by a model in which the R_{rec} − C_t element is explicitly substituted by a transmission line including a transport resistance R_{tr} leads to results similar to those in Table 2. Significant values for R_{tr} cannot be obtained since possible small contributions of the electron transport in the semiconductor are masked by the counter-electrode impedance R_{CE}. This test confirms the facile electron transport in the semiconductor layer provided by the pure ZnO core.

Intensity-modulated photocurrent spectroscopy (IMPS, Figure 7) measurements performed at short circuit under varied light intensities yield the electron transport time τ_{tr} as a quantitative measure of electron transport in the nanoparticulate photoanodes.[67] It describes the time needed for a generated electron to reach the back layer of the anode given by the electron mobility in the semiconductor and is influenced by the competing recombination of an electron with the oxidized form of the redox shuttle.[43,67,68] Due to the significant thickness of the MZO layer, a significant length of the electron transport to the FTO substrate still occurs within MZO. The cells containing MZO with 5 and 10% Mg even exhibit a slightly decreased τ_{tr} compared to cells of pure ZnO. This is in line with the positive effect of small Mg contents on the electron mobility that has previously been observed in other solar cell types.[41,42] Electron mobility is directly

https://doi.org/10.1021/acsaem.2c02236
ACS Appl. Energy Mater. XXXX, XXX, XXX−XXX

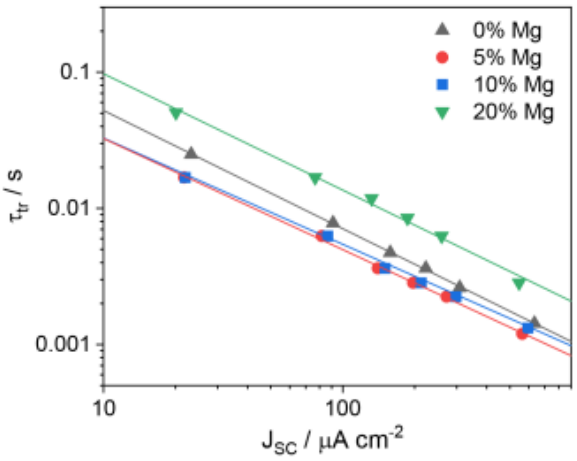

Figure 7. Electron transport times τ_{tr} of DSSCs with varying Mg content calculated from IMPS measurements under a 510 nm LED at different light intensities.

connected to the electron transport in DSSCs by the multitrapping (MT) model.[69−71] The model describes electron diffusion through both the MZO layer and the ZnO core, while electrons undergo constant trapping and thermally activated detrapping from localized trap states. Utilizing ALD to deposit thin layers of MZO in these DSSCs provides the first reported instance of photoanodes where such faster electron transport is achieved in thicker layers beyond the nm scale.

The cell containing MZO with an Mg concentration of 20% shows an increase in τ_{tr} compared to pure ZnO. While recombination is largely suppressed under short-circuit conditions, an increased trap concentration as shown by a decreasing R_{rec} for higher Mg contents (Table 2) has often been discussed to increase electron transport times and decrease electron mobility.[72,73] Earlier measurements of electron mobility of MZO showed increasing electron mobility for MZO layers with 5 and 10% Mg but decreasing mobility for MZO with 20%, in good agreement with the transport times found in Figure 7.[41,42] A reduced collection efficiency is, thereby, confirmed to cause the observed loss in EQE and J_{SC} for the cells containing 20% Mg (Figures 4 and 5).

CONCLUSIONS

In conclusion, we successfully synergized the large band gap energy of MZO with the fast electron transport of ZnO to significantly increase the open-circuit photovoltage of DSSCs. We used ALD on nanoparticulate ZnO to deposit homogeneous layers of Mg-doped ZnO that show the well-known changes in the lattice constants of wurtzite ZnO. The optical band gap energy increases significantly as a function of Mg concentration, corroborating the successful Mg incorporation into ZnO. These core−shell structures were used as photoanodes in DSSCs. V_{OC} increases significantly as a result of the shifted position of the conduction band edge E_{CB} and the quasi-Fermi level $E_{F,n}$. This surpasses earlier reports for samples prepared from solution-based approaches due to the superior conformity and uniformity of dense ALD coatings. Additionally, J_{SC} does not decrease for Mg concentrations up to 10%, leading to significantly enhanced power conversion efficiency of the cells. A slight loss in J_{SC} is observed only for Mg concentrations of 20%. Further, this loss is significantly smaller than in previous DSSCs containing MZO.[46,47] While increasing Mg concentrations in the shell lead to a decrease in recombination resistance as a result of an increased concentration of surface trap states, no significant increase in the transport resistance is found. The electron transport time is largely dominated by good conductivity along the pure ZnO core; it is only slightly attenuated for high Mg concentrations. Overall, by using ALD to achieve a homogeneous MZO shell on a ZnO core, the potential of MZO to increase the V_{OC} of DSSCs is combined with the fast electron transport of pure ZnO to increase the overall solar cell performance. Consequently, this study has shown the advantages of mixed architectures consisting of a pure matrix modified by a well-controlled thin active layer and opens new pathways toward significantly improved concepts for DSSCs. Future work will have to show whether these findings and the improved understanding of the charge-transfer processes in DSSCs including MZO can be transferred to cells using modern Co- or Cu-based electrolytes that should allow for even further increased voltages and, hence, improved efficiencies.

ASSOCIATED CONTENT

Supporting Information

The Supporting Information is available free of charge at https://pubs.acs.org/doi/10.1021/acsaem.2c02236.

Optimization parameters of the ALD deposition, absorption spectra, Tauc plots, $I-V$ curves, and composition of supercycles (PDF)

AUTHOR INFORMATION

Corresponding Author

Derck Schlettwein − *Institute of Applied Physics and Center for Materials Research (ZfM/LaMa), Justus-Liebig University, D-35392 Giessen, Germany;* orcid.org/0000-0002-3446-196X; Email: schlettwein@uni-giessen.de

Authors

Andreas Ringleb − *Institute of Applied Physics and Center for Materials Research (ZfM/LaMa), Justus-Liebig University, D-35392 Giessen, Germany;* orcid.org/0000-0002-6730-8806

Philip Klement − *Institute of Experimental Physics I and Center for Materials Research (ZfM/LaMa), Justus-Liebig University, D-35392 Giessen, Germany;* orcid.org/0000-0001-7044-713X

Jörg Schörmann − *Institute of Experimental Physics I and Center for Materials Research (ZfM/LaMa), Justus-Liebig University, D-35392 Giessen, Germany;* orcid.org/0000-0001-7244-2201

Sangam Chatterjee − *Institute of Experimental Physics I and Center for Materials Research (ZfM/LaMa), Justus-Liebig University, D-35392 Giessen, Germany;* orcid.org/0000-0002-0237-5880

Complete contact information is available at: https://pubs.acs.org/10.1021/acsaem.2c02236

Funding

This work is funded by the German Research Foundation (DFG) via the GRK 2204 "Substitute Materials for sustainable Energy Technologies" and the collaborative research center SFB 1083 (Project-ID 223848855). A.R. acknowledges

financial support by the Deutsche Bundesstiftung Umwelt (DBU) via Project 20019/600.

Notes

The authors declare no competing financial interest.

REFERENCES

(1) Grätzel, M.; O'Regan, B. A low-cost, high-efficiency solar cell based on dye-sensitized colloidal TiO2 films. *Nature* **1991**, *353*, 737−740.

(2) Zhang, D.; Stojanovic, M.; Ren, Y.; Cao, Y.; Eickemeyer, F. T.; Socie, E.; Vlachopoulos, N.; Moser, J.-E.; Zakeeruddin, S. M.; Hagfeldt, A.; Grätzel, M. A molecular photosensitizer achieves a Voc of 1.24 V enabling highly efficient and stable dye-sensitized solar cells with copper(II/I)-based electrolyte. *Nat. Commun.* **2021**, *12* (1), 1777.

(3) Devadiga, D.; Selvakumar, M.; Shetty, P.; Santosh, M. S. Recent progress in dye sensitized solar cell materials and photo-supercapacitors: A review. *J. Power Sources* **2021**, *493*, 229698.

(4) Rondán-Gómez, V.; Montoya De Los Santos, I.; Seuret-Jiménez, D.; Ayala-Mató, F.; Zamudio-Lara, A.; Robles-Bonilla, T.; Courel, M. Recent advances in dye-sensitized solar cells. *Appl. Phys. A* **2019**, *125* (12), 836.

(5) Law, M.; Greene, L. E.; Johnson, J. C.; Saykally, R.; Yang, P. Nanowire dye-sensitized solar cells. *Nat. Mater.* **2005**, *4* (6), 455−459.

(6) Boschloo, G.; Häggman, L.; Hagfeldt, A. Quantification of the effect of 4-tert-butylpyridine addition to I-/I3- redox electrolytes in dye-sensitized nanostructured TiO2 solar cells. *J. Phys. Chem. B* **2006**, *110* (26), 13144−13150.

(7) Le Bahers, T.; Labat, F.; Pauporté, T.; Ciofini, I. Effect of solvent and additives on the open-circuit voltage of ZnO-based dye-sensitized solar cells: a combined theoretical and experimental study. *Phys. Chem. Chem. Phys.* **2010**, *12* (44), 14710−14719.

(8) Paulsson, H.; Kloo, L.; Hagfeldt, A.; Boschloo, G. Electron transport and recombination in dye-sensitized solar cells with ionic liquid electrolytes. *J. Electroanal. Chem.* **2006**, *586* (1), 56−61.

(9) Idígoras, J.; Burdziński, G.; Karolczak, J.; Kubicki, J.; Oskam, G.; Anta, J. A.; Ziółek, M. The Impact of the Electrical Nature of the Metal Oxide on the Performance in Dye-Sensitized Solar Cells: New Look at Old Paradigms. *J. Phys. Chem. C* **2015**, *119* (8), 3931−3944.

(10) Ruess, R.; Scarabino, S.; Ringleb, A.; Nonomura, K.; Vlachopoulos, N.; Hagfeldt, A.; Wittstock, G.; Schlettwein, D. Diverging surface reactions at TiO2- or ZnO-based photoanodes in dye-sensitized solar cells. *Phys. Chem. Chem. Phys.* **2019**, *21* (24), 13047−13057.

(11) Sarkar, K.; Braden, E. V.; Fröschl, T.; Hüsing, N.; Müller-Buschbaum, P. Spray-deposited zinc titanate films obtained via sol-gel synthesis for application in dye-sensitized solar cells. *J. Mater. Chem. A* **2014**, *2* (36), 15008−15014.

(12) Burnside, S.; Moser, J.-E.; Brooks, K.; Grätzel, M.; Cahen, D. Nanocrystalline Mesoporous Strontium Titanate as Photoelectrode Material for Photosensitized Solar Devices: Increasing Photovoltage through Flatband Potential Engineering. *J. Phys. Chem. B* **1999**, *103* (43), 9328−9332.

(13) Lana-Villarreal, T.; Boschloo, G.; Hagfeldt, A. Nanostructured Zinc Stannate as Semiconductor Working Electrodes for Dye-Sensitized Solar Cells. *J. Phys. Chem. C* **2007**, *111* (14), 5549−5556.

(14) Becker, M.; Gies, M.; Polity, A.; Chatterjee, S.; Klar, P. J. Materials processing using radio-frequency ion-sources: Ion-beam sputter-deposition and surface treatment. *Review of scientific instruments* **2019**, *90* (2), 023901.

(15) Laumer, B.; Schuster, F.; Wassner, T. A.; Stutzmann, M.; Rohnke, M.; Schörmann, J.; Eickhoff, M. ZnO/(ZnMg)O single quantum wells with high Mg content graded barriers. *J. Appl. Phys.* **2012**, *111* (11), 113504.

(16) Liu, C. Y.; Xu, H. Y.; Wang, L.; Li, X. H.; Liu, Y. C. Pulsed laser deposition of high Mg-content MgZnO films: Effects of substrate temperature and oxygen pressure. *J. Appl. Phys.* **2009**, *106* (7), 073518.

(17) Asahara, H.; Takamizu, D.; Inokuchi, A.; Hirayama, M.; Teramoto, A.; Saito, S.; Takahashi, M.; Ohmi, T. Characterization of MgZnO films grown by plasma enhanced metal-organic chemical vapor deposition. *Thin Solid Films* **2010**, *518* (11), 2953−2956.

(18) Peng, Q.; Mane, A. U.; Elam, J. W. Nanometer-Thick Mg x Zn (1- x) O Ternary Films for Photovoltaics. *ACS Appl. Nano Mater.* **2020**, *3* (8), 7732−7742.

(19) Wrench, J. S.; Brunell, I. F.; Chalker, P. R.; Jin, J. D.; Shaw, A.; Mitrovic, I. Z.; Hall, S. Compositional tuning of atomic layer deposited MgZnO for thin film transistors. *Appl. Phys. Lett.* **2014**, *105* (20), 202109.

(20) George, S. M. Atomic layer deposition: an overview. *Chem. Rev.* **2010**, *110* (1), 111−131.

(21) Cop, P.; Celik, E.; Hess, K.; Moryson, Y.; Klement, P.; Elm, M. T.; Smarsly, B. M. Atomic Layer Deposition of Nanometer-Sized CeO 2 Layers in Ordered Mesoporous ZrO 2 Films and Their Impact on the Ionic/Electronic Conductivity. *ACS Appl. Nano Mater.* **2020**, *3* (11), 10757−10766.

(22) Celik, E.; Cop, P.; Negi, R. S.; Mazilkin, A.; Ma, Y.; Klement, P.; Schörmann, J.; Chatterjee, S.; Brezesinski, T.; Elm, M. T. Design of Ordered Mesoporous CeO2-YSZ Nanocomposite Thin Films with Mixed Ionic/Electronic Conductivity via Surface Engineering. *ACS Nano* **2022**, *16* (2), 3182−3193.

(23) Seo, S.; Jeong, S.; Park, H.; Shin, H.; Park, N.-G. Atomic layer deposition for efficient and stable perovskite solar cells. *Chemical communications (Cambridge, England)* **2019**, *55* (17), 2403−2416.

(24) Zardetto, V.; Williams, B. L.; Perrotta, A.; Di Giacomo, F.; Verheijen, M. A.; Andriessen, R.; Kessels, W. M. M.; Creatore, M. Atomic layer deposition for perovskite solar cells: research status, opportunities and challenges. *Sustainable Energy Fuels* **2017**, *1* (1), 30−55.

(25) Wu, Y.; Yang, X.; Chen, H.; Zhang, K.; Qin, C.; Liu, J.; Peng, W.; Islam, A.; Bi, E.; Ye, F.; Yin, M.; Zhang, P.; Han, L. Highly compact TiO2 layer for efficient hole-blocking in perovskite solar cells. *Appl. Phys. Express* **2014**, *7* (5), 052301.

(26) Gu, S.; Lin, R.; Han, Q.; Gao, Y.; Tan, H.; Zhu, J. Tin and Mixed Lead-Tin Halide Perovskite Solar Cells: Progress and their Application in Tandem Solar Cells. *Adv. Mater. (Deerfield Beach, Fla.)* **2020**, *32* (27), No. 1907392.

(27) Fang, Z.; Zeng, Q.; Zuo, C.; Zhang, L.; Xiao, H.; Cheng, M.; Hao, F.; Bao, Q.; Zhang, L.; Yuan, Y.; Wu, W.-Q.; Zhao, D.; Cheng, Y.; Tan, H.; Xiao, Z.; Yang, S.; Liu, F.; Jin, Z.; Yan, J.; Ding, L. Perovskite-based tandem solar cells. *Science Bulletin* **2021**, *66* (6), 621−636.

(28) Palmstrom, A. F.; Eperon, G. E.; Leijtens, T.; Prasanna, R.; Habisreutinger, S. N.; Nemeth, W.; Gaulding, E. A.; Dunfield, S. P.; Reese, M.; Nanayakkara, S.; Moot, T.; Werner, J.; Liu, J.; To, B.; Christensen, S. T.; McGehee, M. D.; van Hest, M. F.; Luther, J. M.; Berry, J. J.; Moore, D. T. Enabling Flexible All-Perovskite Tandem Solar Cells. *Joule* **2019**, *3* (9), 2193−2204.

(29) Shanmugam, M.; Baroughi, M. F.; Galipeau, D. Effect of atomic layer deposited ultra thin HfO2 and Al2O3 interfacial layers on the performance of dye sensitized solar cells. *Thin Solid Films* **2010**, *518* (10), 2678−2682.

(30) Park, K.; Zhang, Q.; Garcia, B. B.; Zhou, X.; Jeong, Y.-H.; Cao, G. Effect of an ultrathin TiO(2) layer coated on submicrometer-sized ZnO nanocrystallite aggregates by atomic layer deposition on the performance of dye-sensitized solar cells. *Adv. Mater.* **2010**, *22* (21), 2329−2332.

(31) Martinson, A. B. F.; Elam, J. W.; Hupp, J. T.; Pellin, M. J. ZnO nanotube based dye-sensitized solar cells. *Nano Lett.* **2007**, *7* (8), 2183−2187.

(32) Kim, D. H.; Losego, M. D.; Hanson, K.; Alibabaei, L.; Lee, K.; Meyer, T. J.; Parsons, G. N. Stabilizing chromophore binding on TiO2 for long-term stability of dye-sensitized solar cells using multicomponent atomic layer deposition. *Phys. Chem. Chem. Phys.* **2014**, *16* (18), 8615−8622.

https://doi.org/10.1021/acsaem.2c02236
ACS Appl. Energy Mater. XXXX, XXX, XXX−XXX

(33) Song, W.; Gong, Y.; Tian, J.; Cao, G.; Zhao, H.; Sun, C. Novel Photoanode for Dye-Sensitized Solar Cells with Enhanced Light-Harvesting and Electron-Collection Efficiency. *ACS Appl. Mater. Interfaces* **2016**, *8* (21), 13418−13425.
(34) Kim, D. H.; Woodroof, M.; Lee, K.; Parsons, G. N. Atomic layer deposition of high performance ultrathin TiO_2 blocking layers for dye-sensitized solar cells. *ChemSusChem* **2013**, *6* (6), 1014−1020.
(35) Gao, Z.; Banerjee, P. Review Article: Atomic layer deposition of doped ZnO films. *J. Vac. Sci. Technol. A* **2019**, *37* (5), 050802.
(36) Yang, W.; Son, M.; Rossi, R.; Vrouwenvelder, J. S.; Logan, B. E. Adapting Aluminum-Doped Zinc Oxide for Electrically Conductive Membranes Fabricated by Atomic Layer Deposition. *ACS Appl. Mater. Interfaces* **2020**, *12* (1), 963−969.
(37) Hu, W.; Quang, N. D.; Majumder, S.; Park, E.; Kim, D.; Choi, H.-S.; Chang, H. S. Efficient photo charge transfer of Al-doped ZnO inverse opal shells in SnS2 photoanodes prepared by atomic layer deposition. *J. Alloys Compd.* **2020**, *819*, 153349.
(38) Paskaleva, A.; Blagoev, B. S.; Terziyska, P. T.; Mehandzhiev, V.; Tzvetkov, P.; Kovacheva, D.; Avramova, I.; Spassov, D.; Ivanova, T.; Gesheva, K. Structural, morphological and optical properties of atomic layer deposited transition metal (Co, Ni or Fe)- doped ZnO layers. *J. Mater. Sci: Mater. Electron* **2021**, *32* (6), 7162−7175.
(39) Ohtomo, A.; Kawasaki, M.; Koida, T.; Masubuchi, K.; Koinuma, H.; Sakurai, Y.; Yoshida, Y.; Yasuda, T.; Segawa, Y. MgxZn1-xO as a II-VI widegap semiconductor alloy. *Appl. Phys. Lett.* **1998**, *72* (19), 2466−2468.
(40) Etacheri, V.; Roshan, R.; Kumar, V. Mg-doped ZnO nanoparticles for efficient sunlight-driven photocatalysis. *ACS Appl. Mater. Interfaces* **2012**, *4* (5), 2717−2725.
(41) Mali, S. S.; Patil, J. V.; Hong, C. K. Simultaneous Improved Performance and Thermal Stability of Planar Metal Ion Incorporated CsPbI 2 Br All-Inorganic Perovskite Solar Cells Based on MgZnO Nanocrystalline Electron Transporting Layer. *Adv. Energy Mater.* **2020**, *10* (3), 1902708.
(42) Song, J.; Zheng, E.; Liu, L.; Wang, X.-F.; Chen, G.; Tian, W.; Miyasaka, T. Magnesium-doped Zinc Oxide as Electron Selective Contact Layers for Efficient Perovskite Solar Cells. *ChemSusChem* **2016**, *9* (18), 2640−2647.
(43) Zhang, X.; Welch, K.; Tian, L.; Johansson, M. B.; Häggman, L.; Liu, J.; Johansson, E. M. J. Enhanced charge carrier extraction by a highly ordered wrinkled MgZnO thin film for colloidal quantum dot solar cells. *J. Mater. Chem. C* **2017**, *5* (42), 11111−11120.
(44) Yin, Z.; Zheng, Q.; Chen, S.-C.; Cai, D.; Zhou, L.; Zhang, J. Bandgap Tunable Zn 1- x Mg x O Thin Films as Highly Transparent Cathode Buffer Layers for High-Performance Inverted Polymer Solar Cells. *Adv. Energy Mater.* **2014**, *4* (7), 1301404.
(45) Yin, Z.; Zheng, Q.; Chen, S.-C.; Cai, D.; Ma, Y. Controllable ZnMgO Electron-Transporting Layers for Long-Term Stable Organic Solar Cells with 8.06% Efficiency after One-Year Storage. *Adv. Energy Mater.* **2016**, *6* (4), 1501493.
(46) Ringleb, A.; Ruess, R.; Hofeditz, N.; Heimbrodt, W.; Yoshida, T.; Schlettwein, D. Influence of Mg-doping on the characteristics of ZnO photoanodes in dye-sensitized solar cells. *Phys. Chem. Chem. Phys.* **2021**, *23* (14), 8393−8402.
(47) Raj, C. J.; Prabakar, K.; Karthick, S. N.; Hemalatha, K. V.; Son, M.-K.; Kim, H.-J. Banyan Root Structured Mg-Doped ZnO Photoanode Dye-Sensitized Solar Cells. *J. Phys. Chem. C* **2013**, *117* (6), 2600−2607.
(48) Klement, P.; Anders, D.; Gümbel, L.; Bastianello, M.; Michel, F.; Schörmann, J.; Elm, M. T.; Heiliger, C.; Chatterjee, S. Surface Diffusion Control Enables Tailored-Aspect-Ratio Nanostructures in Area-Selective Atomic Layer Deposition. *ACS Appl. Mater. Interfaces* **2021**, *13* (16), 19398−19405.
(49) Schmidt, R.; Rheinländer, B.; Schubert, M.; Spemann, D.; Butz, T.; Lenzner, J.; Kaidashev, E. M.; Lorenz, M.; Rahm, A.; Semmelhack, H. C.; Grundmann, M. Dielectric functions (1 to 5 eV) of wurtzite MgxZn1-xO (x≤0.29) thin films. *Appl. Phys. Lett.* **2003**, *82* (14), 2260−2262.
(50) Sharma, A. K.; Narayan, J.; Muth, J. F.; Teng, C. W.; Jin, C.; Kvit, A.; Kolbas, R. M.; Holland, O. W. Optical and structural properties of epitaxial MgxZn1-xO alloys. *Appl. Phys. Lett.* **1999**, *75* (21), 3327−3329.
(51) Su, L.; Zhu, Y.; Zhang, Q.; Chen, M.; Ji, X.; Wu, T.; Gui, X.; Pan, B.; Xiang, R.; Tang, Z. Solar-blind wurtzite MgZnO alloy films stabilized by Be doping. *J. Phys. D: Appl. Phys.* **2013**, *46* (24), 245103.
(52) Janotti, A.; van de Walle, C. G. Absolute deformation potentials and band alignment of wurtzite ZnO, MgO, and CdO. *Phys. Rev. B* **2007**, *75* (12), 12120.
(53) Chen, H.; Ma, X.; Zhang, J.; Li, Q.; Liu, H.; Chen, Z.; Chu, G.; Chu, S. Avalanche solar blind photodetectors with high responsivity based on MgO/MgZnO heterostructures. *Opt. Mater. Express* **2018**, *8* (4), 785.
(54) Armstrong, J. C.; Cui, J. B.; Chen, T. P. ALD processed MgZnO buffer layers for Cu(In,Ga)S2 solar cells. *2014 IEEE 40th Photovoltaic Specialist Conference (PVSC)*; IEEE, 2014; pp 304−307. DOI: 10.1109/PVSC.2014.6924919.
(55) Ghosh, M.; Raychaudhuri, A. K. Structural and optical properties of Zn1-xMgxO nanocrystals obtained by low temperature method. *J. Appl. Phys.* **2006**, *100* (3), 034315.
(56) Das, A. K.; Misra, P.; Ajimsha, R. S.; Bose, A.; Joshi, S. C.; Porwal, S.; Sharma, T. K.; Oak, S. M.; Kukreja, L. M. Effect of Mg diffusion on photoluminescence spectra of MgZnO/ZnO bi-layers annealed at different temperatures. *J. Appl. Phys.* **2013**, *114* (18), 183103.
(57) Rossetti, R.; Ellison, J. L.; Gibson, J. M.; Brus, L. E. Size effects in the excited electronic states of small colloidal CdS crystallites. *J. Chem. Phys.* **1984**, *80* (9), 4464−4469.
(58) Monticone, S.; Tufeu, R.; Kanaev, A. V. Complex Nature of the UV and Visible Fluorescence of Colloidal ZnO Nanoparticles. *J. Phys. Chem. B* **1998**, *102* (16), 2854−2862.
(59) Meyenburg, I.; Hofeditz, N.; Ruess, R.; Rudolph, M.; Schlettwein, D.; Heimbrodt, W. Optical determination of charge transfer times from indoline dyes to ZnO in solid state dye-sensitized solar cells. *AIP Advances* **2018**, *8* (5), 055218.
(60) Minda, I.; Ahmed, E.; Sleziona, V.; Richter, C.; Beu, M.; Falgenhauer, J.; Miura, H.; Schlettwein, D.; Schwoerer, H. Identification of different pathways of electron injection in dye-sensitised solar cells of electrodeposited ZnO using an indoline sensitiser. *Physical chemistry chemical physics: PCCP* **2016**, *18* (13), 8938−8944.
(61) Bisquert, J.; Fabregat-Santiago, F. Impedance Spectroscopy: A general introduction and application to dye-sensitized solar cells. In *Dye-sensitized Solar Cells*; EPFL Press, 2010. DOI: 10.1201/b16409.
(62) Bisquert, J. Theory of the Impedance of Electron Diffusion and Recombination in a Thin Layer. *J. Phys. Chem. B* **2002**, *106* (2), 325−333.
(63) Bisquert, J.; Marcus, R. A. Device modeling of dye-sensitized solar cells. *Top. Curr. Chem.* **2013**, *352*, 325−395.
(64) Ruess, R.; Haas, S.; Ringleb, A.; Schlettwein, D. Dye-sensitized solar cells with electrodeposited ZnO and Co(bpy)3 redox electrolyte: Investigation of mass transport in the electrolyte and interfacial charge recombination. *Electrochim. Acta* **2017**, *258*, 591−598.
(65) Guerin, V. M.; Magne, C.; Pauporté, T.; Le Bahers, T.; Rathousky, J. Electrodeposited nanoporous versus nanoparticulate ZnO films of similar roughness for dye-sensitized solar cell applications. *ACS Appl. Mater. Interfaces* **2010**, *2* (12), 3677−3685.
(66) Qiu, X.; Li, L.; Zheng, J.; Liu, J.; Sun, X.; Li, G. Origin of the Enhanced Photocatalytic Activities of Semiconductors: A Case Study of ZnO Doped with Mg 2+. *J. Phys. Chem. C* **2008**, *112* (32), 12242−12248.
(67) Wong, D. K.-P.; Ku, C.-H.; Chen, Y.-R.; Chen, G.-R.; Wu, J.-J. Enhancing electron collection efficiency and effective diffusion length in dye-sensitized solar cells. *ChemPhysChem* **2009**, *10* (15), 2698−2702.
(68) Kim, G.-O.; Ryu, K.-S. Dynamic Response of Charge Transfer and Recombination at Various Electrodes in Dye-sensitized Solar Cells Investigated Using Intensity Modulated Photocurrent and

Photovoltage Spectroscopy. *Bulletin of the Korean Chemical Society* **2012**, *33* (2), 469−472.
(69) Bisquert, J. Chemical Diffusion Coefficient of Electrons in Nanostructured Semiconductor Electrodes and Dye-Sensitized Solar Cells. *J. Phys. Chem. B* **2004**, *108* (7), 2323−2332.
(70) Nissfolk, J.; Fredin, K.; Hagfeldt, A.; Boschloo, G. Recombination and transport processes in dye-sensitized solar cells investigated under working conditions. *J. Phys. Chem. B* **2006**, *110* (36), 17715−17718.
(71) Jennings, J. R.; Ghicov, A.; Peter, L. M.; Schmuki, P.; Walker, A. B. Dye-sensitized solar cells based on oriented TiO2 nanotube arrays: transport, trapping, and transfer of electrons. *J. Am. Chem. Soc.* **2008**, *130* (40), 13364−13372.
(72) Zhang, J.; Feng, J.; Hong, Y.; Zhu, Y.; Han, L. Effect of different trap states on the electron transport of photoanodes in dye sensitized solar cells. *J. Power Sources* **2014**, *257*, 264−271.
(73) Wang, K.-P.; Teng, H. Zinc-doping in TiO2 films to enhance electron transport in dye-sensitized solar cells under low-intensity illumination. *Phys. Chem. Chem. Phys.* **2009**, *11* (41), 9489−9496.

https://doi.org/10.1021/acsaem.2c02236
ACS Appl. Energy Mater. XXXX, XXX, XXX−XXX

Supporting Information for

Harnessing the Potential of Porous ZnO Photoanodes in Dye-Sensitized Solar Cells by Atomic Layer Deposition of Mg-doped ZnO

Andreas Ringleb [a], *Philip Klement* [b], *Jörg Schörmann* [b], *Sangam Chatterjee* [b], *Derck Schlettwein* [a]

[a] Institute of Applied Physics and Center for Materials Research (ZfM/LaMa), Justus-Liebig University, Heinrich-Buff-Ring 16, D-35392 Giessen, Germany

[b] Institute of Experimental Physics I and Center for Materials Research (ZfM/LaMa), Justus-Liebig University, Heinrich-Buff-Ring 16, D-35392 Giessen, Germany

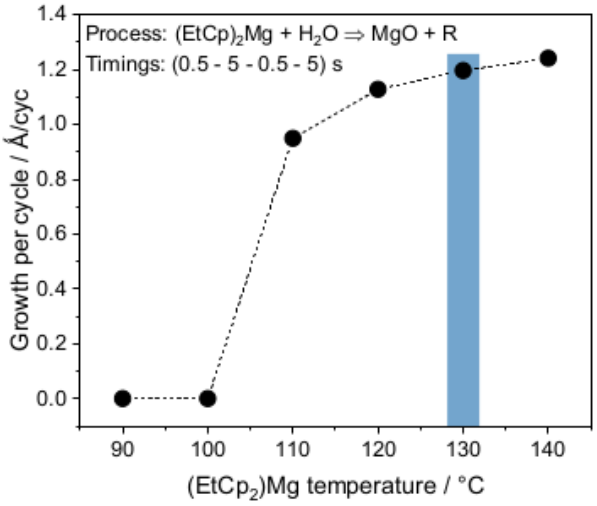

Figure S1. Growth rate of MgO on a Si substrate depending on the precursor source temperature. The optimized deposition temperature window is marked in blue.

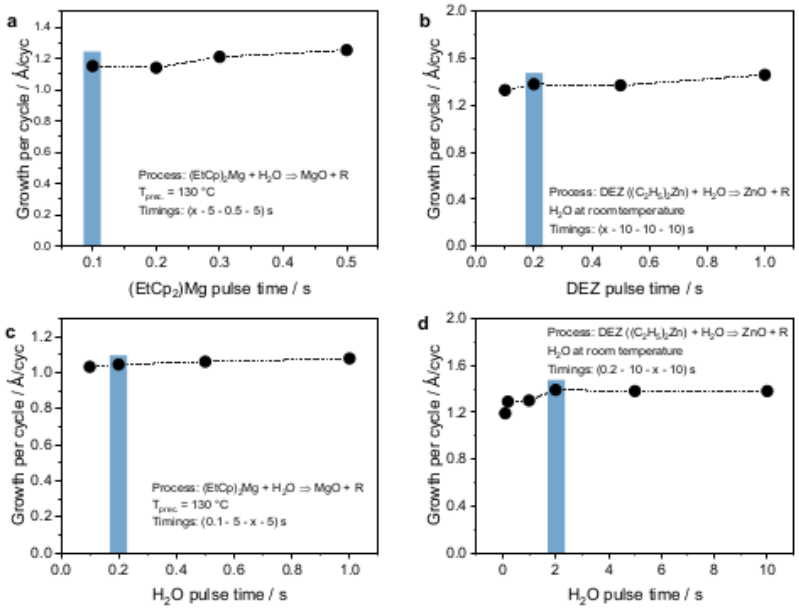

Figure S2. Growth rates of MgO and ZnO on Si substrates depending on the pulse times of the metal precursors and H_2O. (a) Variation of the Mg-precursor pulse time, (b) Variation of the Zn-precursor pulse time, (c) Variation of the H_2O pulse time in the MgO deposition, (d) Variation of the H_2O pulse time in the ZnO deposition. Marked in blue are the pulse times chosen as optimized deposition parameters.

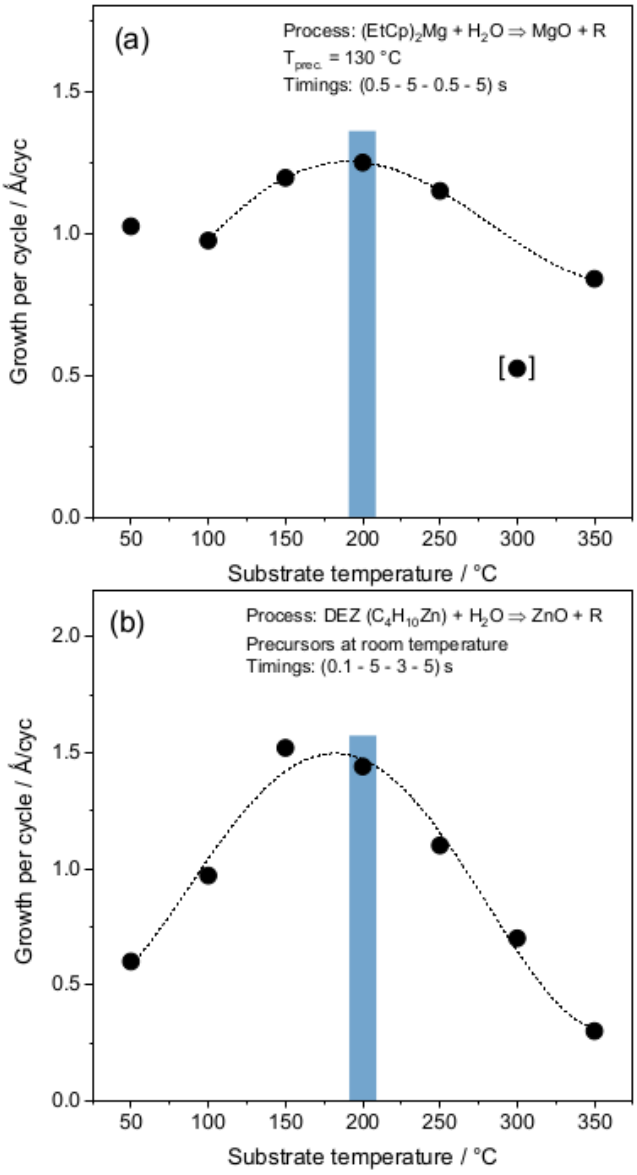

Figure S3. Growth rates of MgO (a) and ZnO (b) on Si substrates depending on the substrate temperature. Marked in blue is the substrate temperature chosen as optimized deposition parameter. The dotted line is meant to guide the eye to the observed trend.

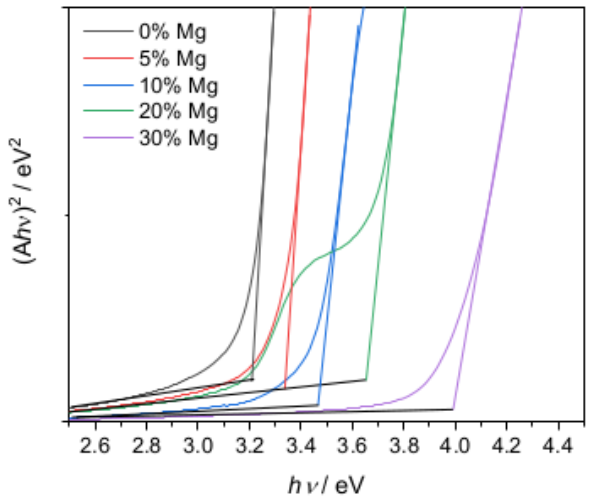

Figure S4. Tauc-plot of the optical absorption spectra and fits to the linear part of MZO thin films with different Mg-concentrations as deposited by ALD. The shoulder appearing for the 20 % sample is an indication of amorphic parts in the non-annealed sample.

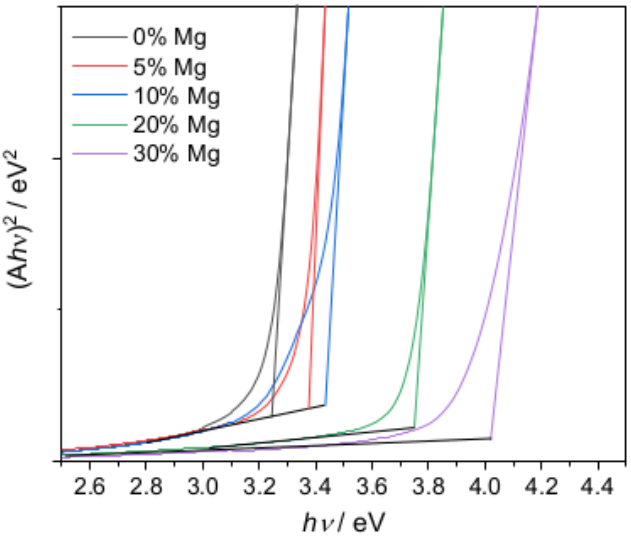

Figure S5. Tauc-plot of the optical absorption spectra and fits to the linear part of MZO films with different Mg-concentrations deposited by ALD after heat treatment at 400 °C. Minor shifts compared to Figure S4 are indicative of the partly amorphous character before annealing.

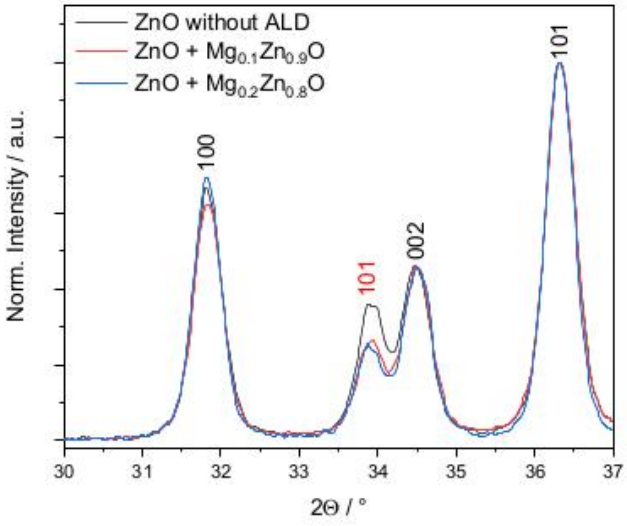

Figure S6. XRD reflexes hkl characteristic of the corresponding ZnO lattice plains (hkl) of pure ZnO nanoparticles as well as combined ZnO-MZO core-shell structures on FTO after heat treatment. No significant shift in the peak positions can be observed. The 101 reflex belonging to the underlying FTO layer has been marked in red.

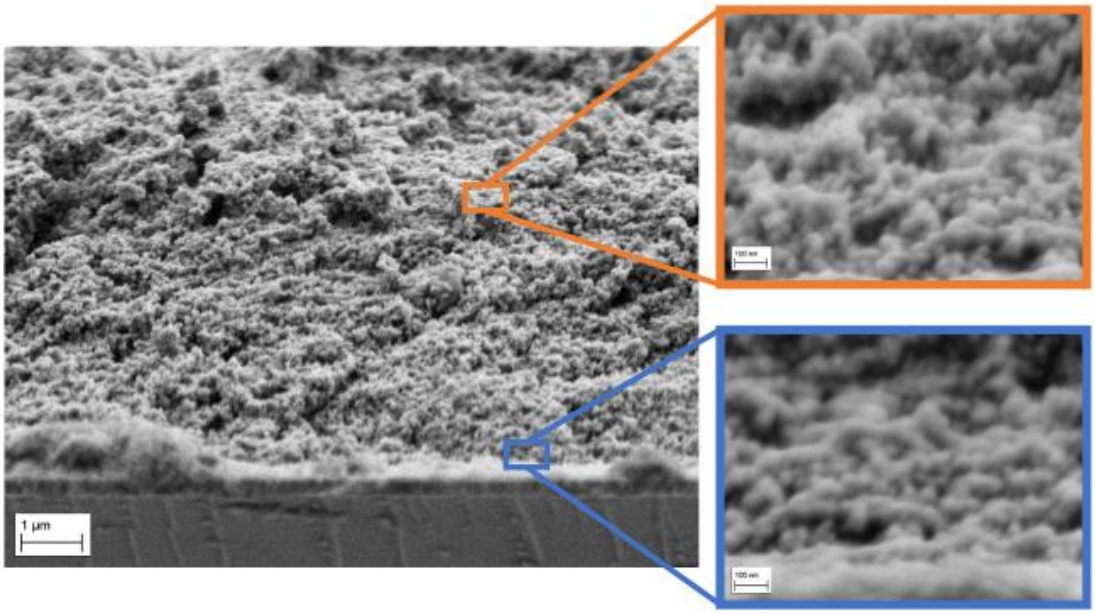

Figure S7. Cross-section SEM image of the nanoparticulate photoanode after deposition of a 5 nm thick MZO layer by ALD.

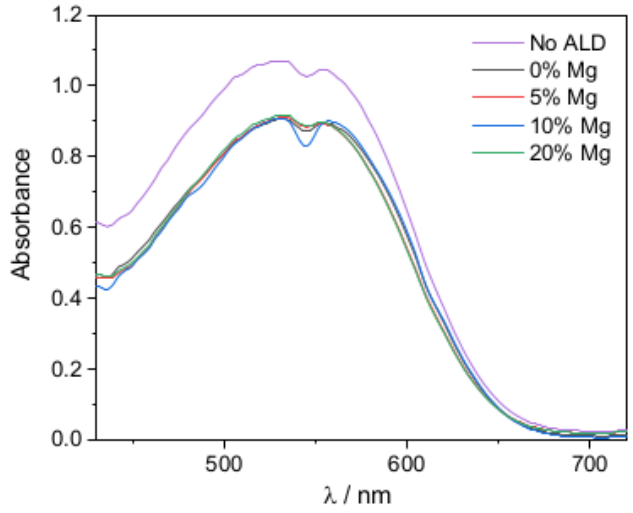

Figure S8. UV-vis spectra of the sensitized photoanodes including an MZO layer of 5 nm thickness and without the ALD deposited MZO layer. The decrease in intensity around 540 nm is due to the measurement setup.

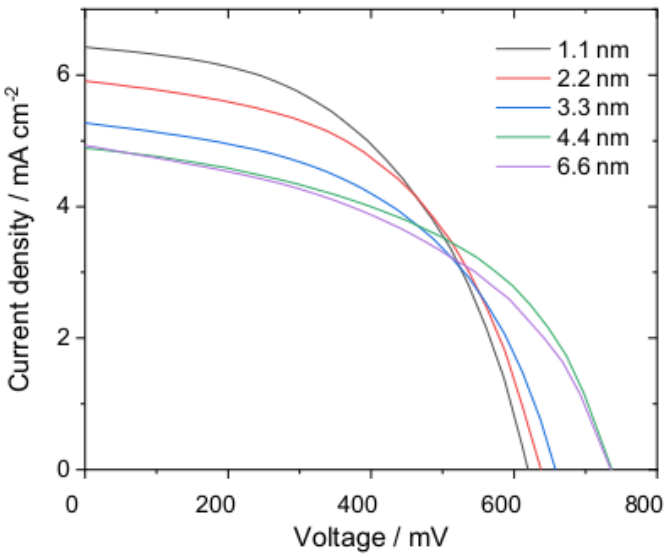

Figure S9. I-V curves DSSCs including an ALD deposited MZO layer with 20% Mg-concentration but varying thickness.

Table S1. Number of MgO and ZnO deposition cycles as well as supercycles and the resulting thickness of the MZO layers deposited on ZnO nanoparticles for the preparation of the DSSCs shown in Figure 8 and S5.

Mg-content / %	y MgO cycles / #	z ZnO cycles / #	Supercycles / #	Thickness d / nm
18.9	2	5	1	1.1
18.9	2	5	2	2.2
18.9	2	5	3	3.3
18.9	2	5	4	4.4
18.9	2	5	6	6.6

Table S2. Number of MgO and ZnO deposition cycles as well as supercycles and the resulting thickness of the MZO layers deposited on ZnO nanoparticles for the preparation of the DSSCs shown in Figure 3 ***a****.*

Mg-content / %	y MgO cycles / #	z ZnO cycles / #	Supercycles / #	Thickness d / nm
0.0	0	25	1	5.0
4.6	1	12	2	4.5
10.4	1	5	5	5.0
19.9	3	7	13	4.7

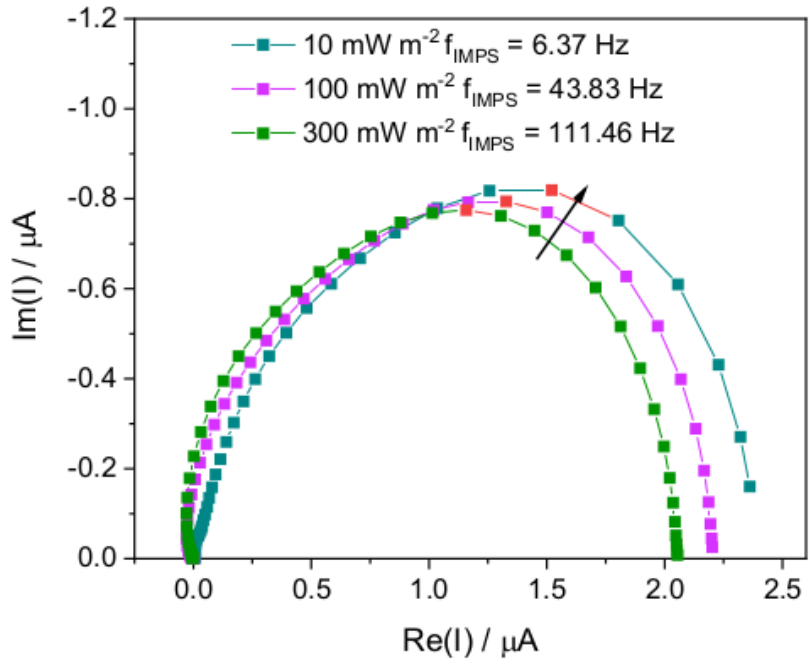

Figure S10. IMPS measurements at varying light intensities for the cell containing an ALD deposited layer of pure ZnO. The measured data at the specific frequencies f_{IMPS} *are marked in red.*

3.2.3 Main Results of Publication (II) in the Context of This Thesis

Extended studies were performed in order to confirm the validity of the super cycle ALD approach and to determine growth parameters for the Zn- and Mg-precursors. SEM pictures and EDS mapping confirmed that conformal MZO layers were grown inside mesoporous ZnO layers by alternating exposure to vapor-phase Mg- and Zn-precursors inside the ALD reactor. Mg was found to be evenly distributed throughout the entire nanoparticulate layer. MZO, in contrast to the earlier sol-gel approach, formed a conformal shell around the ZnO nanoparticles, increasing their size while preserving their shape. UV-vis measurements of as-deposited MZO layers of various Mg-concentrations revealed homogeneous compositions with an increased optical band gap after deposition at 200 °C. Diffusion between the alternating ZnO and MgO layers within the layers of a supercycle was sufficiently fast to establish the desired average composition and yield the optical properties of each given material. Long-range order, however, can only be achieved after an additional heat treatment at 420 °C. Variations in relative peak intensity were observed, depending on the Mg concentration, as was previously reported in respective literature.[164] Shifts of the (100) and (002) reflexes were observed with increasing Mg concentration, similar to the ones observed for fully doped nanoparticles in Publication (I).

While the increased optical band gap is a good indicator for the desired shift of the conduction band edge, a comparison between DSSCs, including ALD-deposited MZO layers with and without heat treatment, revealed that the influence on the V_{OC} was strongly increased after the heat treatment. Furthermore, it could be shown that the V_{OC} increased with increasing MZO film thickness up to 5 nm, but no further increase could be observed for thicker layers. Results from impedance spectroscopy indicate a decrease in recombination after annealing, likely caused by the higher order in the material and a lower concentration of trap states, leading to higher V_{OC} overall. All subsequent DSSCs were therefore prepared by depositing 5 nm of MZO, followed by a heat treatment at 420 °C, to maximize V_{OC}. *I-V* measurements of DSSCs prepared in this manner showed that CS-type photoanodes containing an ALD-deposited MZO layer could reach significantly higher V_{OC} than the ones prepared by sol-gel synthesis (see Figure **13 a**), which were shown in Publication (I). While not quite reaching the V_{OC} shown by NP- and TF-type cells, across all studied photoanodes, DSSCs containing an ALD-deposited MZO layer were able to retain the highest portion of their J_{SC} for Mg concentrations above 5% (Figure **13 b**). This was further confirmed by the integrated current determined from EQE measurements. Previously, cells containing 5% Mg were able to reach the highest *PCEs* due to a combination of moderately increased V_{OC} and stable J_{SC}. However, cells containing ALD-deposited MZO reach their highest *PCE* at a Mg concentration of 10%, very closely followed

by 20%, due to the much higher J_{SC} at these Mg concentrations. A conformal layer deposited by ALD, therefore, enabled the DSSC to fully capitalize on the V_{OC} increase, which was the goal of this work.

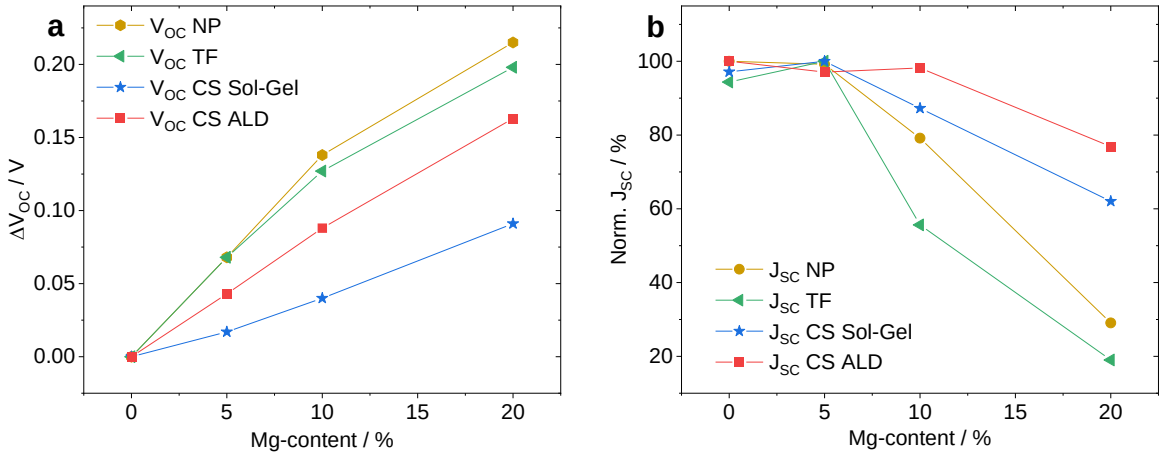

Figure 13. Effects of Mg-concentration on V_{OC} and J_{SC} for all types of photoanodes. ***a*** *Increase in V_{OC} for DSSCs prepared with ALD-deposited MZO (red square) in comparison to results shown in Publication (I). Core-shell structures prepared by ALD showed significantly higher ΔV_{OC} compared to structures prepared by sol-gel synthesis.* ***b*** *Normalized J_{SC} for all types of photoanodes from Publication (I) and (II). Photoanodes containing ALD-deposited MZO exhibit the highest retention of J_{SC} at higher Mg-concentrations.*

In contrast to the NP-type cells studied in Publication (I), no element representing R_{tr} had to be included in the equivalent electrical circuit in order to fit the EIS spectra of the DSSCs prepared with ALD-deposited MZO. The equivalent electrical circuit typically used for DSSCs based on pure ZnO proved sufficient to fit the measured spectra very closely. Attempts to forcefully include an element representing R_{tr} returned insignificantly small values for R_{tr} and did not influence the overall quality of the fit. Additionally, electron transport times τ_{tr} determined from IMPS measurements showed only minor variations within the same order of magnitude. For cells containing MZO layers with 5% and 10% Mg, τ_{tr} was found to be slightly decreased, while it was slightly increased for cells containing 20% Mg. This is perfectly in line with previous measurements of electron mobility in MZO layers in the nm-range but could now be shown for the first time in a structure in the µm-range.[203,204] Overall, electron transport was dominated by the core of pure ZnO, leading to significantly reduced losses in current compared to fully doped nanoparticles and highlighting the success of the strategy to use core-shell particles prepared by ALD.

Furthermore, EIS also showed a reduction in R_{rec} with increasing Mg concentration. This is related to the material characteristics of MZO, as shown in Publication (I), and presents a

tradeoff for the shift of E_{CB}. However, the reduction in R_{rec} was less pronounced in cells containing ALD-deposited MZO compared to NP- and CS-type cells prepared from sol-gel synthesis. This can hint at fewer trap states related to defects in the crystal lattice due to the optimized preparation and indicates an additional advantage of this method.

4. Conclusions and Outlook

The research shown in this work was directed to develop a new approach to increase V_{OC} in ZnO-based DSSCs to bridge the commonly found gap to otherwise identical TiO_2-based DSSCs, which presents the major drawback of ZnO photoanodes. Magnesium doping was used to raise the conduction band edge of ZnO depending on the Mg concentration and increase the potential difference to the redox electrolyte.

MZO nanoparticles were prepared from wet-chemical synthesis through varying reaction pathways. Optical and structural analysis confirmed the integration of up to 20% Mg into the ZnO wurtzite crystal structure when prepared through an oxalate intermediate. This resulted in a significantly increased optical band gap, which could be tuned through the Mg concentration. The popular alternative reaction pathway through hydroxide intermediate showed to limit the Mg concentration to only 5%, with additional Mg appearing as a separate phase. MZO nanoparticles of varying Mg concentrations were used to prepare mesoporous photoanodes for DSSCs. In great agreement with the stated aim of this work, these DSSCs showed significant increases in V_{OC} of up to 40%, depending on the Mg concentration. Simultaneously, J_{SC} was found to significantly decrease for Mg concentrations above 5%, limiting the overall *PCE*. Photoelectrochemical analysis of these cells provided insight into the charge-transfer processes in MZO-based photoanodes. The combined results of EQE and EIS showed the need to consider both electron transport and recombination as potential loss mechanisms. An increased trap density below the conduction band, likely caused by defects as a consequence of changes to the lattice constants for high Mg concentrations, resulted in strongly decreased diffusion lengths for electrons in the MZO photoanode.

In order to limit losses due to increased electron transport times, pure ZnO nanoparticles were coated with an MZO shell in a sol-gel approach. While DSSCs prepared from these core-shell nanoparticles showed increased retention of J_{SC} for higher Mg concentrations, the solution-based approach resulted in a non-conformal covering of the ZnO surface with smaller MZO nanoparticles. Contact between the ZnO core and the redox electrolyte resulted in smaller V_{OC} gains than the ones observed for fully doped nanoparticles. Nevertheless, analysis of EQE and EIS results showed a strongly reduced transport resistance, proving the validity of the ore-shell approach. In order to improve on this initial success, ALD was used to prepare conformal MZO coatings inside mesoporous ZnO layers through a supercycle approach. MZO deposited by ALD exhibited optical and structural properties similar to the ones prepared from solution, but

the nonequilibrium growth enabled even higher doping concentrations. DSSCs including core-shell particles with ALD-deposited MZO showed greatly increased V_{OC} gains compared to those prepared from solution. While losses due to an increased recombination rate continue to be unavoidable even when using ALD-MZO, losses due to increased transport resistance could be nearly eliminated, resulting in high retention of J_{SC} for Mg concentrations of 10% and even 20%. This enables the preparation of DSSCs based on ZnO photoanodes with V_{OC} comparable to or even surpassing TiO_2-based cells without giving up the naturally faster electron transport of ZnO.

The results shown in this work present a first successful step for using MZO in DSSC research and lay the groundwork for future studies. While a broad overview could be provided from the chemical synthesis of MZO to the detailed analysis of its application in solar cells, many options were left unexplored to follow the scope of the project. The materials in this work, in particular the dye and electrolyte, were chosen due to their well-known properties, which allowed focusing on the influence of MZO on solar cell characteristics. However, they do not present the state-of-the-art in DSSC research, limiting the overall efficiencies reached in this work. In first experiments that I performed with modern metal-based electrolytes[14], I noticed similar increase in V_{OC}. This might open the possibility for ZnO-based DSSCs with V_{OC} of up to 1.2 V. However, as previous studies showed, the interactions of these electrolytes with ZnO are far from trivial and require further study. The same holds for the introduction of additives to the electrolyte, which have previously shown differing interactions with ZnO or TiO_2. Additionally, while TRPL showed the injection of relaxed electrons to be only slightly affected in the ps range, further investigation of the injection kinetics in the fs range will show a direct comparison of relevant injection rates into MZO with different Mg content. While the original goals of this study were reached, the application of MZO in DSSCs clearly offers exciting opportunities for research and application in the future.

References

(1) United Nations. *World population to reach 8 billion on 15 November 2022*. https://www.un.org/en/desa/world-population-reach-8-billion-15-november-2022 (accessed 2022-12-06).

(2) H. Ritchie, M. Roser, P. Rosado. *Energy*:*Our World in Data*. https://ourworldindata.org/energy (accessed 2022-12-06).

(3) Bundeswahlleiter. *Bundestagswahl 2021*. https://www.bundeswahlleiter.de/bundestagswahlen/2021/ergebnisse/bund-99.html (accessed 2022-12-06).

(4) Europäisches Parlament. *Ergebnisse der Europawahl 2019: Deutschland*. https://www.europarl.europa.eu/election-results-2019/de/nationale-ergebnisse/deutschland/2019-2024/ (accessed 2022-12-06).

(5) R+V Versicherungen. *Die Ängste der Deutschen 2022*. https://www.ruv.de/newsroom/themenspezial-die-aengste-der-deutschen/grafiken-zahlen-ueberblick (accessed 2022-12-06).

(6) Suri, M.; Betak, J.; Rosina, K.; Chrkavy, D.; Suriova, N.; Cebecauer, T.; Caltik, M.; Erdelyi, B. *Global Photovoltaic Power Potential by Country (English)*. http://documents.worldbank.org/curated/en/466331592817725242/Global-Photovoltaic-Power-Potential-by-Country (accessed 2022-12-13).

(7) Dr. Simon Philipps. *Photovoltaics Report*. https://www.ise.fraunhofer.de/content/dam/ise/de/documents/publications/studies/Photovoltaics-Report.pdf.

(8) Sánchez-Pantoja, N.; Vidal, R.; Pastor, M. C. Aesthetic impact of solar energy systems. *Renew. Sustain. Energy Rev.* **2018**, *98*, 227–238. DOI: 10.1016/j.rser.2018.09.021.

(9) Zhang, D.; Stojanovic, M.; Ren, Y.; Cao, Y.; Eickemeyer, F. T.; Socie, E.; Vlachopoulos, N.; Moser, J.-E.; Zakeeruddin, S. M.; Hagfeldt, A.; Grätzel, M. A molecular photosensitizer achieves a V_{OC} of 1.24 V enabling highly efficient and stable dye-sensitized solar cells with copper(II/I)-based electrolyte. *Nat. Comm.* **2021**, *12* (1), 1777. DOI: 10.1038/s41467-021-21945-3.

(10) Grätzel, M.; O'Regan, B. A low-cost, high-efficiency solar cell based on dye-sensitized colloidal TiO_2 films. *Nature, 1991*, 737–740.

(11) Meyer, G. J. The 2010 millennium technology grand prize: dye-sensitized solar cells. *ACS nano* **2010**, *4* (8), 4337–4343. DOI: 10.1021/nn101591h.

(12) Ji, J.-M.; Zhou, H.; Eom, Y. K.; Kim, C. H.; Kim, H. K. 14.2% Efficiency Dye-Sensitized Solar Cells by Co-sensitizing Novel Thieno[3,2-*b*]indole-Based Organic Dyes with a Promising

Porphyrin Sensitizer. *Adv. Energy Mater.* **2020**, *10* (15), 2000124. DOI: 10.1002/aenm.202000124.

(13) *Exeger*. www.exeger.com (accessed 2022-12-07).

(14) Feldt, S. M.; Gibson, E. A.; Gabrielsson, E.; Sun, L.; Boschloo, G.; Hagfeldt, A. Design of organic dyes and cobalt polypyridine redox mediators for high-efficiency dye-sensitized solar cells. *J. Am. Chem. Soc.* **2010**, *132* (46), 16714–16724. DOI: 10.1021/ja1088869.

(15) Ren, Y.; Sun, D.; Cao, Y.; Tsao, H. N.; Yuan, Y.; Zakeeruddin, S. M.; Wang, P.; Grätzel, M. A Stable Blue Photosensitizer for Color Palette of Dye-Sensitized Solar Cells Reaching 12.6% Efficiency. *J. Am. Chem. Soc.* **2018**, *140* (7), 2405–2408. DOI: 10.1021/jacs.7b12348.

(16) Kurumisawa, Y.; Higashino, T.; Nimura, S.; Tsuji, Y.; Iiyama, H.; Imahori, H. Renaissance of Fused Porphyrins: Substituted Methylene-Bridged Thiophene-Fused Strategy for High-Performance Dye-Sensitized Solar Cells. *J. Am. Chem. Soc.* **2019**, *141* (25), 9910–9919. DOI: 10.1021/jacs.9b03302.

(17) Saygili, Y.; Söderberg, M.; Pellet, N.; Giordano, F.; Cao, Y.; Muñoz-García, A. B.; Zakeeruddin, S. M.; Vlachopoulos, N.; Pavone, M.; Boschloo, G.; Kavan, L.; Moser, J.-E.; Grätzel, M.; Hagfeldt, A.; Freitag, M. Copper Bipyridyl Redox Mediators for Dye-Sensitized Solar Cells with High Photovoltage. *J. Am. Chem. Soc.* **2016**, *138* (45), 15087–15096. DOI: 10.1021/jacs.6b10721.

(18) Wu, J.; Lan, Z.; Lin, J.; Huang, M.; Huang, Y.; Fan, L.; Luo, G. Electrolytes in dye-sensitized solar cells. *Chem. Rev.* **2015**, *115* (5), 2136–2173. DOI: 10.1021/cr400675m.

(19) Wang, X.; Zhao, B.; Kan, W.; Xie, Y.; Pan, K. Review on Low-Cost Counter Electrode Materials for Dye-Sensitized Solar Cells: Effective Strategy to Improve Photovoltaic Performance. *Adv. Mater. Interfaces* **2022**, *9* (2), 2101229. DOI: 10.1002/admi.202101229.

(20) He, Y.; Hu, J.; Xie, Y. High-efficiency dye-sensitized solar cells of up to 8.03% by air plasma treatment of ZnO nanostructures. *ChemComm* **2015**, *51* (90), 16229–16232. DOI: 10.1039/c5cc04567c.

(21) Chandiran, A. K.; Abdi-Jalebi, M.; Nazeeruddin, M. K.; Grätzel, M. Analysis of electron transfer properties of ZnO and TiO_2 photoanodes for dye-sensitized solar cells. *ACS nano* **2014**, *8* (3), 2261–2268. DOI: 10.1021/nn405535j.

(22) Ruess, R.; Scarabino, S.; Ringleb, A.; Nonomura, K.; Vlachopoulos, N.; Hagfeldt, A.; Wittstock, G.; Schlettwein, D. Diverging surface reactions at TiO_2- or ZnO-based photoanodes in dye-sensitized solar cells. *Phys. Chem. Chem. Phys.* **2019**, *21* (24), 13047–13057. DOI: 10.1039/c9cp01215j.

(23) Idígoras, J.; Burdziński, G.; Karolczak, J.; Kubicki, J.; Oskam, G.; Anta, J. A.; Ziółek, M. The Impact of the Electrical Nature of the Metal Oxide on the Performance in Dye-Sensitized Solar Cells: New Look at Old Paradigms. *J. Phys. Chem. C* **2015**, *119* (8), 3931–3944. DOI: 10.1021/jp512330f.

(24) Anta, J. A.; Guillén, E.; Tena-Zaera, R. ZnO-Based Dye-Sensitized Solar Cells. *J. Phys. Chem. C* **2012**, *116* (21), 11413–11425. DOI: 10.1021/jp3010025.

(25) Lu, L.; Li, R.; Peng, T.; Fan, K.; Dai, K. Effects of rare earth ion modifications on the photoelectrochemical properties of ZnO-based dye-sensitized solar cells. *Renew. Energ.* **2011**, *36* (12), 3386–3393. DOI: 10.1016/j.renene.2011.05.010.

(26) Sarkar, K.; Braden, E. V.; Fröschl, T.; Hüsing, N.; Müller-Buschbaum, P. Spray-deposited zinc titanate films obtained via sol–gel synthesis for application in dye-sensitized solar cells. *J. Mater. Chem. A* **2014**, *2* (36), 15008–15014. DOI: 10.1039/C4TA02031F.

(27) Lana-Villarreal, T.; Boschloo, G.; Hagfeldt, A. Nanostructured Zinc Stannate as Semiconductor Working Electrodes for Dye-Sensitized Solar Cells. *J. Phys. Chem. C* **2007**, *111* (14), 5549–5556. DOI: 10.1021/jp0678756.

(28) Ohtomo, A.; Kawasaki, M.; Koida, T.; Masubuchi, K.; Koinuma, H.; Sakurai, Y.; Yoshida, Y.; Yasuda, T.; Segawa, Y. $Mg_xZn_{1-x}O$ as a II–VI widegap semiconductor alloy. *Appl. Phys. Lett.* **1998**, *72* (19), 2466–2468. DOI: 10.1063/1.121384.

(29) MacLeod, B. A.; Schulz, P.; Cowan, S. R.; Garcia, A.; Ginley, D. S.; Kahn, A.; Olson, D. C. Improved Performance in Bulk Heterojunction Organic Solar Cells with a Sol-Gel MgZnO Electron-Collecting Layer. *Adv. Energy Mater.* **2014**, *4* (13), 1400073. DOI: 10.1002/aenm.201400073.

(30) Yin, Z.; Zheng, Q.; Chen, S.-C.; Cai, D.; Ma, Y. Controllable ZnMgO Electron-Transporting Layers for Long-Term Stable Organic Solar Cells with 8.06% Efficiency after One-Year Storage. *Adv. Energy Mater.* **2016**, *6* (4), 1501493. DOI: 10.1002/aenm.201501493.

(31) Yin, Z.; Zheng, Q.; Chen, S.-C.; Cai, D.; Zhou, L.; Zhang, J. Bandgap Tunable $Zn_{1-x}Mg_xO$ Thin Films as Highly Transparent Cathode Buffer Layers for High-Performance Inverted Polymer Solar Cells. *Adv. Energy Mater.* **2014**, *4* (7), 1301404. DOI: 10.1002/aenm.201301404.

(32) Raj, C. J.; Prabakar, K.; Karthick, S. N.; Hemalatha, K. V.; Son, M.-K.; Kim, H.-J. Banyan Root Structured Mg-Doped ZnO Photoanode Dye-Sensitized Solar Cells. *J. Phys. Chem. C* **2013**, *117* (6), 2600–2607. DOI: 10.1021/jp308847g.

(33) Justin Raj, C.; Karthick, S. N.; Hemalatha, K. V.; Son, M.-K.; Kim, H.-J.; Prabakar, K. Magnesium doped ZnO nanoparticles embedded ZnO nanorod hybrid electrodes for dye

sensitized solar cells. *J. Sol-Gel Sci. Technol.* **2012**, *62* (3), 453–459. DOI: 10.1007/s10971-012-2748-0.

(34) Guo, X.; Dong, H.; Niu, G.; Qiu, Y.; Wang, L. Mg doping in nanosheet-based spherical structured ZnO photoanode for quasi-solid dye-sensitized solar cells. *RSC Adv.* **2014**, *4* (41), 21294–21300. DOI: 10.1039/C4RA03188A.

(35) Hagfeldt, A.; Grätzel, M. Molecular photovoltaics. *Acc. Chem. Res.* **2000**, *33* (5), 269–277. DOI: 10.1021/ar980112j.

(36) Hagfeldt, A.; Boschloo, G.; Sun, L.; Kloo, L.; Pettersson, H. Dye-sensitized solar cells. *Chem. Rev.* **2010**, *110* (11), 6595–6663. DOI: 10.1021/cr900356p.

(37) Wu, J.; Lan, Z.; Lin, J.; Huang, M.; Huang, Y.; Fan, L.; Luo, G.; Lin, Y.; Xie, Y.; Wei, Y. Counter electrodes in dye-sensitized solar cells. *Chem. Soc. Rev.* **2017**, *46* (19), 5975–6023. DOI: 10.1039/c6cs00752j.

(38) Muñoz-García, A. B.; Benesperi, I.; Boschloo, G.; Concepcion, J. J.; Delcamp, J. H.; Gibson, E. A.; Meyer, G. J.; Pavone, M.; Pettersson, H.; Hagfeldt, A.; Freitag, M. Dye-sensitized solar cells strike back. *Chem. Soc. Rev.* **2021**, *50* (22), 12450–12550. DOI: 10.1039/d0cs01336f.

(39) Hardin, B. E.; Snaith, H. J.; McGehee, M. D. The renaissance of dye-sensitized solar cells. *Nat. Photon* **2012**, *6* (3), 162–169. DOI: 10.1038/nphoton.2012.22.

(40) Gerischer, H.; Michel-Beyerle, M. E.; Rebentrost, F.; Tributsch, H. Sensitization of charge injection into semiconductors with large band gap. *Electrochim. Acta* **1968**, *13* (6), 1509–1515. DOI: 10.1016/0013-4686(68)80076-3.

(41) Matsumura, M.; Matsudaira, S.; Tsubomura, H.; Takata, M.; Yanagida, H. Dye Sensitization and Surface Structures of Semiconductor Electrodes. *Ind. Eng. Chem. Prod. Res. Dev.* **1980**, *19* (3), 415–421. DOI: 10.1021/i360075a025.

(42) Vafaee, M.; Ghamsari, M. S. Preparation and characterization of ZnO nanoparticles by a novel sol–gel route. *Mater. Lett.* **2007**, *61* (14-15), 3265–3268. DOI: 10.1016/j.matlet.2006.11.089.

(43) Sun, H.; Sun, L.; Sugiura, T.; White, M. S.; Stadler, P.; Saricifci, N. S.; Masuhara, A.; Yoshida, T. Microwave-assisted Hydrothermal Synthesis of Structure-controlled ZnO Nanocrystals and Their Properties in Dye-sensitized Solar Cells. *Electrochemistry* **2017**, *85* (5), 253–261. DOI: 10.5796/electrochemistry.85.253.

(44) Rudolph, M.; Yoshida, T.; Schlettwein, D. Influence of indoline dye and coadsorbate molecules on photovoltaic performance and recombination in dye-sensitized solar cells based

on electrodeposited ZnO. *J. Electroanal. Chem.* **2013**, *709*, 10–18. DOI: 10.1016/j.jelechem.2013.09.028.

(45) Kim, D. H.; Losego, M. D.; Peng, Q.; Parsons, G. N. Atomic Layer Deposition for Sensitized Solar Cells: Recent Progress and Prospects. *Adv. Mater. Interfaces* **2016**, *3* (21), 1600354. DOI: 10.1002/admi.201600354.

(46) Panepinto, A.; Michiels, M.; Dürrschnabel, M. T.; Molina-Luna, L.; Bittencourt, C.; Cormier, P.-A.; Snyders, R. Synthesis of Anatase (Core)/Rutile (Shell) Nanostructured TiO_2 Thin Films by Magnetron Sputtering Methods for Dye-Sensitized Solar Cell Applications. *ACS Appl. Energy Mater.* **2020**, *3* (1), 759–767. DOI: 10.1021/acsaem.9b01910.

(47) Zhang, Q.; Dandeneau, C. S.; Zhou, X.; Cao, G. ZnO Nanostructures for Dye-Sensitized Solar Cells. *Adv. Mater.* **2009**, *21* (41), 4087–4108. DOI: 10.1002/adma.200803827.

(48) Chen, X.; Mao, S. S. Titanium dioxide nanomaterials: synthesis, properties, modifications, and applications. *Chem. Rev.* **2007**, *107* (7), 2891–2959. DOI: 10.1021/cr0500535.

(49) Feng, X.; Shankar, K.; Varghese, O. K.; Paulose, M.; Latempa, T. J.; Grimes, C. A. Vertically aligned single crystal TiO_2 nanowire arrays grown directly on transparent conducting oxide coated glass: synthesis details and applications. *Nano Lett.* **2008**, *8* (11), 3781–3786. DOI: 10.1021/nl802096a.

(50) Bendall, J. S.; Etgar, L.; Tan, S. C.; Cai, N.; Wang, P.; Zakeeruddin, S. M.; Grätzel, M.; Welland, M. E. An efficient DSSC based on ZnO nanowire photo-anodes and a new D-π-A organic dye. *Energy Environ. Sci.* **2011**, *4* (8), 2903. DOI: 10.1039/c1ee01254a.

(51) Martinson, A. B. F.; Góes, M. S.; Fabregat-Santiago, F.; Bisquert, J.; Pellin, M. J.; Hupp, J. T. Electron Transport in Dye-Sensitized Solar Cells Based on ZnO Nanotubes: Evidence for Highly Efficient Charge Collection and Exceptionally Rapid Dynamics †. *J. Phys. Chem. A* **2009**, *113* (16), 4015–4021. DOI: 10.1021/jp810406q.

(52) Yi, Z.; Zeng, Y.; Wu, H.; Chen, X.; Fan, Y.; Yang, H.; Tang, Y.; Yi, Y.; Wang, J.; Wu, P. Synthesis, surface properties, crystal structure and dye-sensitized solar cell performance of TiO_2 nanotube arrays anodized under different parameters. *Results Phys.* **2019**, *15*, 102609. DOI: 10.1016/j.rinp.2019.102609.

(53) Lin, C.-Y.; Lai, Y.-H.; Chen, H.-W.; Chen, J.-G.; Kung, C.-W.; Vittal, R.; Ho, K.-C. Highly efficient dye-sensitized solar cell with a ZnO nanosheet-based photoanode. *Energy Environ. Sci.* **2011**, *4* (9), 3448. DOI: 10.1039/c0ee00587h.

(54) Laskova, B.; Zukalova, M.; Kavan, L.; Chou, A.; Liska, P.; Wei, Z.; Bin, L.; Kubat, P.; Ghadiri, E.; Moser, J. E.; Grätzel, M. Voltage enhancement in dye-sensitized solar cell using

(001)-oriented anatase TiO_2 nanosheets. *J Solid State Electrochem* **2012**, *16* (9), 2993–3001. DOI: 10.1007/s10008-012-1729-0.

(55) Ako, R. T.; Peiris, D.; Ekanayake, P.; Tan, A. L.; Young, D. J.; Zheng, Z.; Chellappan, V. DSSCs with ZnO@TiO_2 core–shell photoanodes showing improved V: Modification of energy gradients and potential barriers with Cd and Mg ion dopants. *Sol. Energy Mater. Sol. Cells* **2016**, *157*, 18–27. DOI: 10.1016/j.solmat.2016.05.009.

(56) Law, M.; Greene, L. E.; Radenovic, A.; Kuykendall, T.; Liphardt, J.; Yang, P. ZnO-Al_2O_3 and ZnO-TiO_2 core-shell nanowire dye-sensitized solar cells. *J. Phys. Chem. B* **2006**, *110* (45), 22652–22663. DOI: 10.1021/jp0648644.

(57) Hamann, T. W. The end of iodide? Cobalt complex redox shuttles in DSSCs. *Dalt. Trans.* **2012**, *41* (11), 3111–3115. DOI: 10.1039/c2dt12362b.

(58) Michaels, H.; Benesperi, I.; Edvinsson, T.; Muñoz-Garcia, A.; Pavone, M.; Boschloo, G.; Freitag, M. Copper Complexes with Tetradentate Ligands for Enhanced Charge Transport in Dye-Sensitized Solar Cells. *Inorganics* **2018**, *6* (2), 53. DOI: 10.3390/inorganics6020053.

(59) Bisquert, J.; Cahen, D.; Hodes, G.; Ruehle, S.; Zaban, A. Physical Chemical Principles of Photovoltaic Conversion with Nanoparticulate, Mesoporous Dye-Sensitized Solar Cells. *ChemInform* **2004**, *35* (36). DOI: 10.1002/chin.200436269.

(60) O'Regan, B. C.; Durrant, J. R. Kinetic and energetic paradigms for dye-sensitized solar cells: moving from the ideal to the real. *Acc. Chem. Res.* **2009**, *42* (11), 1799–1808. DOI: 10.1021/ar900145z.

(61) Nazeeruddin, M. K.; Kay, A.; Rodicio, I.; Humphry-Baker, R.; Mueller, E.; Liska, P.; Vlachopoulos, N.; Graetzel, M. Conversion of light to electricity by cis-X_2bis(2,2'-bipyridyl-4,4'-dicarboxylate)ruthenium(II) charge-transfer sensitizers (X = Cl^-, Br^-, I^-, CN^-, and SCN^-) on nanocrystalline titanium dioxide electrodes. *J. Am. Chem. Soc.* **1993**, *115* (14), 6382–6390. DOI: 10.1021/ja00067a063.

(62) Dürr, M.; Yasuda, A.; Nelles, G. On the origin of increased open circuit voltage of dye-sensitized solar cells using 4- tert -butyl pyridine as additive to the electrolyte. *Appl. Phys. Lett.* **2006**, *89* (6), 61110. DOI: 10.1063/1.2266386.

(63) Le Bahers, T.; Labat, F.; Pauporté, T.; Ciofini, I. Effect of solvent and additives on the open-circuit voltage of ZnO-based dye-sensitized solar cells: a combined theoretical and experimental study. *Phys. Chem. Chem. Phys.* **2010**, *12* (44), 14710–14719. DOI: 10.1039/c004358c.

(64) Boschloo, G.; Häggman, L.; Hagfeldt, A. Quantification of the effect of 4-tert-butylpyridine addition to I^-/I_3^- redox electrolytes in dye-sensitized nanostructured TiO^2 solar cells. *J. Phys. Chem. B* **2006**, *110* (26), 13144–13150. DOI: 10.1021/jp0619641.

(65) Kashif, M. K.; Axelson, J. C.; Duffy, N. W.; Forsyth, C. M.; Chang, C. J.; Long, J. R.; Spiccia, L.; Bach, U. A new direction in dye-sensitized solar cells redox mediator development: in situ fine-tuning of the cobalt(II)/(III) redox potential through Lewis base interactions. *J. Am. Chem. Soc.* **2012**, *134* (40), 16646–16653. DOI: 10.1021/ja305897k.

(66) Jennings, J. R.; Wang, Q. Influence of Lithium Ion Concentration on Electron Injection, Transport, and Recombination in Dye-Sensitized Solar Cells. *J. Phys. Chem. C* **2010**, *114* (3), 1715–1724. DOI: 10.1021/jp9104129.

(67) Meyenburg, I.; Hofeditz, N.; Ruess, R.; Rudolph, M.; Schlettwein, D.; Heimbrodt, W. Optical determination of charge transfer times from indoline dyes to ZnO in solid state dye-sensitized solar cells. *AIP Adv.* **2018**, *8* (5), 55218. DOI: 10.1063/1.5025777.

(68) Koops, S. E.; O'Regan, B. C.; Barnes, P. R. F.; Durrant, J. R. Parameters Influencing the Efficiency of Electron Injection in Dye-Sensitized Solar Cells. *J. Am. Chem. Soc.* **2009**, *131* (13), 4808–4818. DOI: 10.1021/ja8091278.

(69) El-Zohry, A.; Orthaber, A.; Zietz, B. Isomerization and Aggregation of the Solar Cell Dye D149. *J. Phys. Chem. C* **2012**, *116* (50), 26144–26153. DOI: 10.1021/jp306636w.

(70) Beer. Bestimmung der Absorption des rothen Lichts in farbigen Flüssigkeiten. *Ann. Phys. Chem.* **1852**, *162* (5), 78–88. DOI: 10.1002/andp.18521620505.

(71) Luther, R.; Nikolopulos, A. Über die Beziehungen zwischen den Absorptionsspektren und der Konstitution der komplexen Kobaltamminsalze. *Z. Phys. Chem.* **1913**, *82U* (1), 361–384. DOI: 10.1515/zpch-1913-8229.

(72) Rong, Y.; Liu, L.; Mei, A.; Li, X.; Han, H. Beyond Efficiency: the Challenge of Stability in Mesoscopic Perovskite Solar Cells. *Adv. Energy Mater.* **2015**, *5* (20), 1501066. DOI: 10.1002/aenm.201501066.

(73) Gundlach, L.; Willig, F. Ultrafast photoinduced electron transfer at electrodes: the general case of a heterogeneous electron-transfer reaction. *ChemPhysChem* **2012**, *13* (12), 2877–2881. DOI: 10.1002/cphc.201200151.

(74) Marcus, R. A. On the Theory of Electron-Transfer Reactions. VI. Unified Treatment for Homogeneous and Electrode Reactions. *J. Chem. Phys.* **1965**, *43* (2), 679–701. DOI: 10.1063/1.1696792.

(75) Gerischer, H. Kinetics of oxidation-reduction reactions on metals and semiconductors:General remarks on the electron transition between a solid body and a reduction-oxidation electrolyte. *Z. Phys. Chem. NF* **1960** (26), 223.

(76) Ardo, S.; Meyer, G. J. Photodriven heterogeneous charge transfer with transition-metal compounds anchored to TiO_2 semiconductor surfaces. *Chem. Soc. Rev.* **2009**, *38* (1), 115–164. DOI: 10.1039/B804321N.

(77) Filipič, M.; Berginc, M.; Smole, F.; Topič, M. Analysis of electron recombination in dye-sensitized solar cell. *Curr. Appl. Phys.* **2012**, *12* (1), 238–246. DOI: 10.1016/j.cap.2011.06.011.

(78) Rudolph, M. Pholoelectrochemical Characterization of Dye-Sensitzed Solar Cells Based on ZnO and Organic Dyes. Dissertation, Justus-Liebig-Universität, Gießen, 2015.

(79) Haque, S. A.; Palomares, E.; Cho, B. M.; Green, A. N. M.; Hirata, N.; Klug, D. R.; Durrant, J. R. Charge Separation versus Recombination in Dye-Sensitized Nanocrystalline Solar Cells: the Minimization of Kinetic Redundancy. *J. Am. Chem. Soc.* **2005**, *127* (10), 3456–3462. DOI: 10.1021/ja0460357.

(80) Peter, L. M. Dye-sensitized nanocrystalline solar cells. *Phys. Chem. Chem. Phys.* **2007**, *9* (21), 2630–2642. DOI: 10.1039/b617073k.

(81) Peter, L. M.; Wijayantha, K. G. U. Electron transport and back reaction in dye sensitized nanocrystalline photovoltaic cells. *Electrochim. Acta* **2000** (45), 4543–4551. DOI: 10.1016/S0013-4686(00)00605-8.

(82) Oekermann, T.; Yoshida, T.; Boeckler, C.; Caro, J.; Minoura, H. Capacitance and field-driven electron transport in electrochemically self-assembled nanoporous ZnO/dye hybrid films. *J. Phys. Chem. B* **2005**, *109* (25), 12560–12566. DOI: 10.1021/jp051394p.

(83) Quintana, M.; Edvinsson, T.; Hagfeldt, A.; Boschloo, G. Comparison of Dye-Sensitized ZnO and TiO_2 Solar Cells: Studies of Charge Transport and Carrier Lifetime. *J. Phys. Chem. C* **2007**, *111* (2), 1035–1041. DOI: 10.1021/jp065948f.

(84) Nakade, S.; Kanzaki, T.; Kubo, W.; Kitamura, T.; Wada, Y.; Yanagida, S. Role of electrolytes on charge recombination in dye-sensitized TiO_2 solar cell: the case of solar cells using the I^-/I_3^- redox couple. *J. Phys. Chem. B* **2005**, *109* (8), 3480–3487. DOI: 10.1021/jp0460036.

(85) Kopidakis, N.; Schiff, E. A.; Park, N.-G.; van de Lagemaat, J.; Frank, A. J. Ambipolar Diffusion of Photocarriers in Electrolyte-Filled, Nanoporous TiO_2. *J. Phys. Chem. B* **2000**, *104* (16), 3930–3936. DOI: 10.1021/jp9936603.

(86) Gangotri, P.; Gangotri, K. M. Studies of the Micellar Effect on Photogalvanics: Solar Energy Conversion and Storage in EDTA−safranine O−Tween-80 System. *Energy Fuels* **2009**, *23* (5), 2767–2772. DOI: 10.1021/ef9000709.

(87) Góes, M. S.; Joanni, E.; Muniz, E. C.; Savu, R.; Habeck, T. R.; Bueno, P. R.; Fabregat-Santiago, F. Impedance Spectroscopy Analysis of the Effect of TiO_2 Blocking Layers on the Efficiency of Dye Sensitized Solar Cells. *J. Phys. Chem. C* **2012**, *116* (23), 12415–12421. DOI: 10.1021/jp301694r.

(88) Jennings, J. R.; Ghicov, A.; Peter, L. M.; Schmuki, P.; Walker, A. B. Dye-sensitized solar cells based on oriented TiO_2 nanotube arrays: transport, trapping, and transfer of electrons. *J. Am. Chem. Soc.* **2008**, *130* (40), 13364–13372. DOI: 10.1021/ja804852z.

(89) Tang, H.; Prasad, K.; Sanjinès, R.; Schmid, P. E.; Lévy, F. Electrical and optical properties of TiO_2 anatase thin films. *J. Appl. Phys.* **1994**, *75* (4), 2042–2047. DOI: 10.1063/1.356306.

(90) Hunklinger, S.; Enss, C. *Solid State Physics*; De Gruyter Textbook; De Gruyter, 2022. DOI: 10.1515/9783110666502.

(91) Bisquert, J.; Vikhrenko, V. S. Interpretation of the Time Constants Measured by Kinetic Techniques in Nanostructured Semiconductor Electrodes and Dye-Sensitized Solar Cells. *J. Phys. Chem. B* **2004**, *108* (7), 2313–2322. DOI: 10.1021/jp035395y.

(92) Oekermann, T.; Yoshida, T.; Minoura, H.; Wijayantha, K. G. U.; Peter, L. M. Electron Transport and Back Reaction in Electrochemically Self-Assembled Nanoporous ZnO/Dye Hybrid Films. *J. Phys. Chem. B* **2004**, *108* (24), 8364–8370. DOI: 10.1021/jp037831m.

(93) Boschloo, G.; Fitzmaurice, D. Spectroelectrochemical Investigation of Surface States in Nanostructured TiO_2 Electrodes. *J. Phys. Chem. B* **1999**, *103* (12), 2228–2231. DOI: 10.1021/jp984414e.

(94) Murakami, T. N.; Koumura, N.; Kimura, M.; Mori, S. Structural effect of donor in organic dye on recombination in dye-sensitized solar cells with cobalt complex electrolyte. *Langmuir* **2014**, *30* (8), 2274–2279. DOI: 10.1021/la4047808.

(95) Marinado, T.; Nonomura, K.; Nissfolk, J.; Karlsson, M. K.; Hagberg, D. P.; Sun, L.; Mori, S.; Hagfeldt, A. How the nature of triphenylamine-polyene dyes in dye-sensitized solar cells affects the open-circuit voltage and electron lifetimes. *Langmuir* **2010**, *26* (4), 2592–2598. DOI: 10.1021/la902897z.

(96) Li, G.; Liang, M.; Wang, H.; Sun, Z.; Wang, L.; Wang, Z.; Xue, S. Significant Enhancement of Open-Circuit Voltage in Indoline-Based Dye-Sensitized Solar Cells via Retarding Charge Recombination. *Chem. Mater.* **2013**, *25* (9), 1713–1722. DOI: 10.1021/cm400196w.

(97) Saygili, Y.; Stojanovic, M.; Michaels, H.; Tiepelt, J.; Teuscher, J.; Massaro, A.; Pavone, M.; Giordano, F.; Zakeeruddin, S. M.; Boschloo, G.; Moser, J.-E.; Grätzel, M.; Muñoz-García, A. B.; Hagfeldt, A.; Freitag, M. Effect of Coordination Sphere Geometry of Copper Redox Mediators on Regeneration and Recombination Behavior in Dye-Sensitized Solar Cell Applications. *ACS Appl. Energy Mater.* **2018**, *1* (9), 4950–4962. DOI: 10.1021/acsaem.8b00957.

(98) Soman, S.; Pradhan, S. C.; Yoosuf, M.; Vinayak, M. V.; Lingamoorthy, S.; Gopidas, K. R. Probing Recombination Mechanism and Realization of Marcus Normal Region Behavior in DSSCs Employing Cobalt Electrolytes and Triphenylamine Dyes. *J. Phys. Chem. C* **2018**, *122* (25), 14113–14127. DOI: 10.1021/acs.jpcc.8b01325.

(99) Yang, K.; Yang, X.; Zhang, L.; An, J.; Wang, H.; Deng, Z. Copper redox mediators with alkoxy groups suppressing recombination for dye-sensitized solar cells. *Electrochim. Acta* **2021**, *368*, 137564. DOI: 10.1016/j.electacta.2020.137564.

(100) Ondersma, J. W.; Hamann, T. W. Recombination and redox couples in dye-sensitized solar cells. *Coord. Chem. Rev.* **2013**, *257* (9-10), 1533–1543. DOI: 10.1016/j.ccr.2012.09.010.

(101) Bisquert, J.; Zaban, A.; Salvador, P. Analysis of the Mechanisms of Electron Recombination in Nanoporous TiO_2 Dye-Sensitized Solar Cells. Nonequilibrium Steady-State Statistics and Interfacial Electron Transfer via Surface States. *J. Phys. Chem. B* **2002**, *106* (34), 8774–8782. DOI: 10.1021/jp026058c.

(102) Bisquert, J. Theory of the Impedance of Electron Diffusion and Recombination in a Thin Layer. *J. Phys. Chem. B* **2002**, *106* (2), 325–333. DOI: 10.1021/jp011941g.

(103) Bisquert, J.; Mora-Seró, I. Simulation of Steady-State Characteristics of Dye-Sensitized Solar Cells and the Interpretation of the Diffusion Length. *J. Phys. Chem. Lett.* **2010**, *1* (1), 450–456. DOI: 10.1021/jz900297b.

(104) Bailes, M.; Cameron, P. J.; Lobato, K.; Peter, L. M. Determination of the density and energetic distribution of electron traps in dye-sensitized nanocrystalline solar cells. *J. Phys. Chem. B* **2005**, *109* (32), 15429–15435. DOI: 10.1021/jp050822o.

(105) Feldt, S. M.; Lohse, P. W.; Kessler, F.; Nazeeruddin, M. K.; Grätzel, M.; Boschloo, G.; Hagfeldt, A. Regeneration and recombination kinetics in cobalt polypyridine based dye-sensitized solar cells, explained using Marcus theory. *Phys. Chem. Chem. Phys.* **2013**, *15* (19), 7087–7097. DOI: 10.1039/c3cp50997d.

(106) Liu, Y.; Jennings, J. R.; Huang, Y.; Wang, Q.; Zakeeruddin, S. M.; Grätzel, M. Cobalt Redox Mediators for Ruthenium-Based Dye-Sensitized Solar Cells: A Combined Impedance

Spectroscopy and Near-IR Transmittance Study. *J. Phys. Chem. C* **2011**, *115* (38), 18847–18855. DOI: 10.1021/jp204519s.

(107) Srivishnu, K. S.; Prasanthkumar, S.; Giribabu, L. Cu(II/I) redox couples: potential alternatives to traditional electrolytes for dye-sensitized solar cells. *Mater. Adv.* **2021**, *2* (4), 1229–1247. DOI: 10.1039/D0MA01023E.

(108) Yang, W.; Vlachopoulos, N.; Hao, Y.; Hagfeldt, A.; Boschloo, G. Efficient dye regeneration at low driving force achieved in triphenylamine dye LEG4 and TEMPO redox mediator based dye-sensitized solar cells. *Phys. Chem. Chem. Phys.* **2015**, *17* (24), 15868–15875. DOI: 10.1039/c5cp01880c.

(109) Boschloo, G.; Hagfeldt, A. Characteristics of the iodide/triiodide redox mediator in dye-sensitized solar cells. *Acc. Chem. Res.* **2009**, *42* (11), 1819–1826. DOI: 10.1021/ar900138m.

(110) Robson, K. C. D.; Hu, K.; Meyer, G. J.; Berlinguette, C. P. Atomic level resolution of dye regeneration in the dye-sensitized solar cell. *J. Am. Chem. Soc.* **2013**, *135* (5), 1961–1971. DOI: 10.1021/ja311640f.

(111) Li, B.; Wang, L.; Kang, B.; Wang, P.; Qiu, Y. Review of recent progress in solid-state dye-sensitized solar cells. *Sol. Energy Mater. Sol. Cells* **2006**, *90* (5), 549–573. DOI: 10.1016/j.solmat.2005.04.039.

(112) Bui, T.-T.; Goubard, F. Recent advances in small molecular, non-polymeric organic hole transporting materials for solid-state DSSC. *EPJ Photovolt.* **2013**, *4*, 40402. DOI: 10.1051/epjpv/2013024.

(113) Ruess, R.; Haas, S.; Ringleb, A.; Schlettwein, D. Dye-sensitized solar cells with electrodeposited ZnO and $Co(bpy)_3$ redox electrolyte: Investigation of mass transport in the electrolyte and interfacial charge recombination. *Electrochim. Acta* **2017**, *258*, 591–598. DOI: 10.1016/j.electacta.2017.11.102.

(114) Nelson, J. J.; Amick, T. J.; Elliott, C. M. Mass Transport of Polypyridyl Cobalt Complexes in Dye-Sensitized Solar Cells with Mesoporous TiO_2 Photoanodes. *J. Phys. Chem. C* **2008**, *112* (46), 18255–18263. DOI: 10.1021/jp806479k.

(115) Klahr, B. M.; Hamann, T. W. Performance Enhancement and Limitations of Cobalt Bipyridyl Redox Shuttles in Dye-Sensitized Solar Cells. *J. Phys. Chem. C* **2009**, *113* (31), 14040–14045. DOI: 10.1021/jp903431s.

(116) Cao, Y.; Liu, Y.; Zakeeruddin, S. M.; Hagfeldt, A.; Grätzel, M. Direct Contact of Selective Charge Extraction Layers Enables High-Efficiency Molecular Photovoltaics. *Joule* **2018**, *2* (6), 1108–1117. DOI: 10.1016/j.joule.2018.03.017.

(117) Wei, W.; Wang, H.; Hu, Y. H. A review on PEDOT-based counter electrodes for dye-sensitized solar cells. *Int. J. Energy Res.* **2014**, *38* (9), 1099–1111. DOI: 10.1002/er.3178.

(118) Borysiewicz, M. A. ZnO as a Functional Material, a Review. *Crystals* **2019**, *9* (10), 505. DOI: 10.3390/cryst9100505.

(119) Frederickson, C. J.; Koh, J.-Y.; Bush, A. I. The neurobiology of zinc in health and disease. *Nat. Rev. Neurosci.* **2005**, *6* (6), 449–462. DOI: 10.1038/nrn1671.

(120) Moezzi, A.; McDonagh, A. M.; Cortie, M. B. Zinc oxide particles: Synthesis, properties and applications. *Chem. Eng. J.* **2012**, *185-186*, 1–22. DOI: 10.1016/j.cej.2012.01.076.

(121) Zhang, P.; Wu, J.; Zhang, T.; Wang, Y.; Liu, D.; Chen, H.; Ji, L.; Liu, C.; Ahmad, W.; Chen, Z. D.; Li, S. Perovskite Solar Cells with ZnO Electron-Transporting Materials. *Adv. Mater.* **2018**, *30* (3), 1703737. DOI: 10.1002/adma.201703737.

(122) Hagiwara, Y.; Nakada, T.; Kunioka, A. Improved J_{SC} in CIGS thin film solar cells using a transparent conducting ZnO:B window layer. *Sol. Energy Mater. Sol. Cells* **2001**, *67* (1-4), 267–271. DOI: 10.1016/S0927-0248(00)00291-9.

(123) Huang, J.; Yin, Z.; Zheng, Q. Applications of ZnO in organic and hybrid solar cells. *Energy Environ. Sci.* **2011**, *4* (10), 3861. DOI: 10.1039/c1ee01873f.

(124) Lee, K. M.; Lai, C. W.; Ngai, K. S.; Juan, J. C. Recent developments of zinc oxide based photocatalyst in water treatment technology: A review. *Water Res.* **2016**, *88*, 428–448. DOI: 10.1016/j.watres.2015.09.045.

(125) Qiu, X.; Li, L.; Zheng, J.; Liu, J.; Sun, X.; Li, G. Origin of the Enhanced Photocatalytic Activities of Semiconductors: A Case Study of ZnO Doped with Mg^{2+}. *J. Phys. Chem. C* **2008**, *112* (32), 12242–12248. DOI: 10.1021/jp803129e.

(126) Tian, C.; Zhang, Q.; Wu, A.; Jiang, M.; Liang, Z.; Jiang, B.; Fu, H. Cost-effective large-scale synthesis of ZnO photocatalyst with excellent performance for dye photodegradation. *ChemComm* **2012**, *48* (23), 2858–2860. DOI: 10.1039/c2cc16434e.

(127) Zhang, X. Q.; Suemune, I.; Kumano, H.; Yao, Z. G.; Huang, S. H. Room temperature ultraviolet lasing action in high-quality ZnO thin films. *J. Lumin.* **2007**, *122-123*, 828–830. DOI: 10.1016/j.jlumin.2006.01.300.

(128) Djurišić, A. B.; Ng, A.; Chen, X. Y. ZnO nanostructures for optoelectronics: Material properties and device applications. *Prog. Quantum. Electron.* **2010**, *34* (4), 191–259. DOI: 10.1016/j.pquantelec.2010.04.001.

(129) Kara, R.; Mentar, L.; Azizi, A. Synthesis and characterization of Mg-doped ZnO thin-films electrochemically grown on FTO substrates for optoelectronic applications. *RSC Adv.* **2020**, *10* (66), 40467–40479. DOI: 10.1039/D0RA06541B.

(130) Emanetoglu, N.; Gorla, C.; Liu, Y.; Liang, S.; Lu, Y. Epitaxial ZnO piezoelectric thin films for saw filters. *Mater. Sci. Semicond. Process* **1999**, *2* (3), 247–252. DOI: 10.1016/S1369-8001(99)00022-0.

(131) Gullapalli, H.; Vemuru, V. S. M.; Kumar, A.; Botello-Mendez, A.; Vajtai, R.; Terrones, M.; Nagarajaiah, S.; Ajayan, P. M. Flexible piezoelectric ZnO-paper nanocomposite strain sensor. *Small* **2010**, *6* (15), 1641–1646. DOI: 10.1002/smll.201000254.

(132) Kumar, B.; Kim, S.-W. Energy harvesting based on semiconducting piezoelectric ZnO nanostructures. *Nano Energy* **2012**, *1* (3), 342–355. DOI: 10.1016/j.nanoen.2012.02.001.

(133) Hongsith, N.; Viriyaworasakul, C.; Mangkorntong, P.; Mangkorntong, N.; Choopun, S. Ethanol sensor based on ZnO and Au-doped ZnO nanowires. *Ceram. Int.* **2008**, *34* (4), 823–826. DOI: 10.1016/j.ceramint.2007.09.099.

(134) Mitra, P.; Chatterjee, A. P.; Maiti, H. S. ZnO thin film sensor. *Mat. Lett.* **1998**, *35* (1-2), 33–38. DOI: 10.1016/S0167-577X(97)00215-2.

(135) Zhu, L.; Zeng, W. Room-temperature gas sensing of ZnO-based gas sensor: A review. *Sens. Actuator A Phys.* **2017**, *267*, 242–261. DOI: 10.1016/j.sna.2017.10.021.

(136) Thomas, D. G. The exciton spectrum of zinc oxide. *J. Phys. Chem. Solids* **1960**, *15* (1-2), 86–96. DOI: 10.1016/0022-3697(60)90104-9.

(137) Özgür, Ü.; Alivov, Y. I.; Liu, C.; Teke, A.; Reshchikov, M. A.; Doğan, S.; Avrutin, V.; Cho, S.-J.; Morkoç, H. A comprehensive review of ZnO materials and devices. *J. Appl. Phys.* **2005**, *98* (4), 41301. DOI: 10.1063/1.1992666.

(138) Gao, W.; Li, Z. ZnO thin films produced by magnetron sputtering. *Ceram. Int.* **2004**, *30* (7), 1155–1159. DOI: 10.1016/j.ceramint.2003.12.197.

(139) Paraguay D., F.; Estrada L., W.; Acosta N., D. R.; Andrade, E.; Miki-Yoshida, M. Growth, structure and optical characterization of high quality ZnO thin films obtained by spray pyrolysis. *Thin Solid Films* **1999**, *350* (1-2), 192–202. DOI: 10.1016/S0040-6090(99)00050-4.

(140) O'Brien, S.; Koh, L.; Crean, G. M. ZnO thin films prepared by a single step sol–gel process. *Thin Solid Films* **2008**, *516* (7), 1391–1395. DOI: 10.1016/j.tsf.2007.03.160.

(141) Zhao, J.-L.; Li, X.-M.; Bian, J.-M.; Yu, W.-D.; Gao, X.-D. Structural, optical and electrical properties of ZnO films grown by pulsed laser deposition (PLD). *J. Cryst. Growth* **2005**, *276* (3-4), 507–512. DOI: 10.1016/j.jcrysgro.2004.11.407.

(142) Tynell, T.; Karppinen, M. Atomic layer deposition of ZnO: a review. *Semicond. Sci. Technol.* **2014**, *29* (4), 43001. DOI: 10.1088/0268-1242/29/4/043001.

(143) Liu, Y.; Gorla, C. R.; Liang, S.; Emanetoglu, N.; Lu, Y.; Shen, H.; Wraback, M. Ultraviolet detectors based on epitaxial ZnO films grown by MOCVD. *J. Electron. Mater.* **2000**, *29* (1), 69–74. DOI: 10.1007/s11664-000-0097-1.

(144) Ellmer, K.; Bikowski, A. Intrinsic and extrinsic doping of ZnO and ZnO alloys. *J. Phys. D: Appl. Phys.* **2016**, *49* (41), 413002. DOI: 10.1088/0022-3727/49/41/413002.

(145) Janotti, A.; van de Walle, C. G. Absolute deformation potentials and band alignment of wurtzite ZnO, MgO, and CdO. *Phys. Rev. B* **2007**, *75* (12). DOI: 10.1103/PhysRevB.75.121201.

(146) Chen, H.; Ma, X.; Zhang, J.; Li, Q.; Liu, H.; Chen, Z.; Chu, G.; Chu, S. Avalanche solar blind photodetectors with high responsivity based on MgO/MgZnO heterostructures. *Opt. Mater. Express* **2018**, *8* (4), 785. DOI: 10.1364/OME.8.000785.

(147) Wang, X.; Saito, K.; Tanaka, T.; Nishio, M.; Guo, Q. Lower temperature growth of single phase MgZnO films in all Mg content range. *J. Alloys Compd.* **2015**, *627*, 383–387. DOI: 10.1016/j.jallcom.2014.12.128.

(148) Park, W. I.; Yi, G.-C.; Jang, H. M. Metalorganic vapor-phase epitaxial growth and photoluminescent properties of $Zn_{1-x}Mg_xO$ ($0 \leqslant x \leqslant 0.49$) thin films. *Appl. Phys. Lett.* **2001**, *79* (13), 2022–2024. DOI: 10.1063/1.1405811.

(149) Ghosh, R.; Basak, D. Composition dependence of electrical and optical properties in sol-gel $Mg_xZn_{1-x}O$ thin films. *J. Appl. Phys.* **2007**, *101* (2), 23507. DOI: 10.1063/1.2426380.

(150) Pradeev Raj, K.; Sadaiyandi, K.; Kennedy, A.; Sagadevan, S.; Chowdhury, Z. Z.; Johan, M. R. B.; Aziz, F. A.; Rafique, R. F.; Thamiz Selvi, R.; Rathina Bala, R. Influence of Mg Doping on ZnO Nanoparticles for Enhanced Photocatalytic Evaluation and Antibacterial Analysis. *Nanoscale Res. Lett.* **2018**, *13* (1), 229. DOI: 10.1186/s11671-018-2643-x.

(151) Hornsby, P. R.; Wang, J.; Rothon, R.; Jackson, G.; Wilkinson, G.; Cossick, K. Thermal decomposition behaviour of polyamide fire-retardant compositions containing magnesium hydroxide filler. *Polym. Degrad. Stab* **1996**, *51* (3), 235–249. DOI: 10.1016/0141-3910(95)00181-6.

(152) Oh, J.-Y.; Lim, S.-C.; Ahn, S. D.; Lee, S. S.; Cho, K.-I.; Koo, J. B.; Choi, R.; Hasan, M. Facile one-step synthesis of magnesium-doped ZnO nanoparticles: optical properties and their device applications. *J. Phys. D: Appl. Phys.* **2013**, *46* (28), 285101. DOI: 10.1088/0022-3727/46/28/285101.

(153) Sharma, S.; Vyas, R.; Sharma, N.; Singh, V.; Singh, A.; Kataria, V.; Gupta, B. K.; Vijay, Y. K. Highly efficient green light harvesting from Mg doped ZnO nanoparticles: Structural and optical studies. *J. Alloys Compd.* **2013**, *552*, 208–212. DOI: 10.1016/j.jallcom.2012.10.084.

(154) Kasi, G.; Seo, J. Influence of Mg doping on the structural, morphological, optical, thermal, and visible-light responsive antibacterial properties of ZnO nanoparticles synthesized via co-precipitation. *Mater. Sci. Eng. C* **2019**, *98*, 717–725. DOI: 10.1016/j.msec.2019.01.035.

(155) Raj, C. J.; Paramesh, G.; Prakash, B. S.; Meher, K. P.; Varma, K. Origin of giant dielectric constant and conductivity behavior in $Zn_{1-x}Mg_xO$ ($0 \leq x \leq 0.1$) ceramics. *Physica E Low Dimens. Syst. Nanostruct.* **2016**, *74*, 1–8. DOI: 10.1016/j.materresbull.2015.10.006.

(156) Samanta, A.; Goswami, M. N.; Mahapatra, P. K. Optical properties and enhanced photocatalytic activity of Mg-doped ZnO nanoparticles. *Physica E: Low-dimensional Systems and Nanostructures* **2018**, *104*, 254–260. DOI: 10.1016/j.physe.2018.07.042.

(157) Ghosh, M.; Raychaudhuri, A. K. Structural and optical properties of $Zn_{1-x}Mg_xO$ nanocrystals obtained by low temperature method. *J. Appl. Phys.* **2006**, *100* (3), 34315. DOI: 10.1063/1.2227708.

(158) Wang, H.; Liu, Q.; Ma, X.; Liu, H.; Zhang, X. Wurtzite $Mg_{0.3}Zn_{0.7}O$ film and UV detector. *J. Mater. Sci.: Mater. Electron.* **2018**, *29* (15), 13052–13057. DOI: 10.1007/s10854-018-9427-z.

(159) Kılınç, N.; Arda, L.; Öztürk, S.; Öztürk, Z. Z. Structure and electrical properties of Mg-doped ZnO nanoparticles. *Cryst. Res. Technol.* **2010**, *45* (5), 529–538. DOI: 10.1002/crat.200900662.

(160) Etacheri, V.; Roshan, R.; Kumar, V. Mg-doped ZnO nanoparticles for efficient sunlight-driven photocatalysis. *ACS Appl. Mater. Interfaces* **2012**, *4* (5), 2717–2725. DOI: 10.1021/am300359h.

(161) Angermann, A.; Töpfer, J. Synthesis of nanocrystalline Mn–Zn ferrite powders through thermolysis of mixed oxalates. *Ceram. Int.* **2011**, *37* (3), 995–1002. DOI: 10.1016/j.ceramint.2010.11.019.

(162) Vladimirova, E.; Vassiliev, V.; Nossov, A. Synthesis of $La_{1-x}Pb_xMnO_3$ colossal magnetoresistive ceramics from co-precipitated oxalate precursors. *J. Mater. Sci.* **2001**, *36* (6), 1481–1486. DOI: 10.1023/A:1017548813705.

(163) Choy, J.-H.; Han, Y.-S.; Kim, S.-J. Oxalate coprecipitation route to the piezoelectric $Pb(Zr,Ti)O_3$ oxide. *J. Mater. Chem.* **1997**, *7* (9), 1807–1813. DOI: 10.1039/a700391i.

(164) Peng, Q.; Mane, A. U.; Elam, J. W. Nanometer-Thick $Mg_xZn_{1-x}O$ Ternary Films for Photovoltaics. *ACS Appl. Nano Mater.* **2020**, *3* (8), 7732–7742. DOI: 10.1021/acsanm.0c01309.

(165) Wrench, J. S.; Brunell, I. F.; Chalker, P. R.; Jin, J. D.; Shaw, A.; Mitrovic, I. Z.; Hall, S. Compositional tuning of atomic layer deposited MgZnO for thin film transistors. *Appl. Phys. Lett.* **2014**, *105* (20), 202109. DOI: 10.1063/1.4902389.

(166) George, S. M. Atomic layer deposition: an overview. *Chem. Rev.* **2010**, *110* (1), 111–131. DOI: 10.1021/cr900056b.

(167) Mackus, A. J. M.; Schneider, J. R.; MacIsaac, C.; Baker, J. G.; Bent, S. F. Synthesis of Doped, Ternary, and Quaternary Materials by Atomic Layer Deposition: A Review. *Chem. Mater.* **2019**, *31* (4), 1142–1183. DOI: 10.1021/acs.chemmater.8b02878.

(168) Andreas Ringleb; Philip Klement; Jörg Schörmann; Sangam Chatterjee; and Derck Schlettwein. Harnessing the Potential of Porous ZnO Photoanodes in Dye-Sensitized Solar Cells by Atomic Layer Deposition of Mg-Doped ZnO. *ACS Appl. Energy Mater.* **2022**, *5* (12), 14825–14835. DOI: 10.1021/acsaem.2c02236.s001.

(169) Cop, P.; Celik, E.; Hess, K.; Moryson, Y.; Klement, P.; Elm, M. T.; Smarsly, B. M. Atomic Layer Deposition of Nanometer-Sized CeO_2 Layers in Ordered Mesoporous ZrO_2 Films and Their Impact on the Ionic/Electronic Conductivity. *ACS Appl. Nano Mater.* **2020**, *3* (11), 10757–10766. DOI: 10.1021/acsanm.0c02060.

(170) Hagfeldt, A.; Boschloo, G.; Lindström, H.; Figgemeier, E.; Holmberg, A.; Aranyos, V.; Magnusson, E.; Malmqvist, L. A system approach to molecular solar cells. *Coord. Chem. Rev.* **2004**, *248* (13-14), 1501–1509. DOI: 10.1016/j.ccr.2004.04.012.

(171) Birkholz, M.; Fewster, P. F.; Genzel, C. *Thin film analysis by X-ray scattering*, 2nd reprint; Wiley-VCH, 2009. DOI: 10.1002/3527607595.

(172) Che, M.; Védrine, J. C. *Characterization of solid materials and heterogeneous catalysts*; Wiley-VCH-Verl., (2012). DOI: 10.1002/9783527645329.

(173) BRAGG, W. L. The Specular Reflection of X-rays. *Nature* **1912**, *90* (2250), 410. DOI: 10.1038/090410b0.

(174) Kirk Othmer. *Encyclopedia of chemical technology*, 5. ed.; Wiley, 2004. DOI: 10.1002/0471238961.

(175) Perkampus, H.-H. *UV-VIS Spectroscopy and Its Applications*; Springer Lab Manuals; Springer Berlin Heidelberg, 1992.

(176) Akash, M. S. H.; Rehman, K. Ultraviolet-Visible (UV-VIS) Spectroscopy. In *Essentials of Pharmaceutical Analysis*; Rehman, K., Akash, M. S. H., Eds.; Springer, 2020; pp 29–56. DOI: 10.1007/978-981-15-1547-7_3.

(177) Mayerhöfer, T. G.; Pahlow, S.; Popp, J. The Bouguer-Beer-Lambert Law: Shining Light on the Obscure. *ChemPhysChem* **2020**, *21* (18), 2029–2046. DOI: 10.1002/cphc.202000464.

(178) Ian Mills, Tomislav Cvitas, Klaus Homann, Nikola Kallay, Kozo Kuchitsu. *Quantities, Units and Symbols in Physical Chemistry*, 2nd; Blackwell Science, 1993.

(179) Torrent, J.; Barrón, V. Diffuse Reflectance Spectroscopy. In *Methods of Soil Analysis: Part 5-Mineralogical Methods*; Ulery, A. L., Drees, R., Eds.; SSSA Book Series; SSSA, 2008; pp 367–385. DOI: 10.2136/sssabookser5.5.c13.

(180) Mirabella, F. M., Ed. *Modern techniques in applied molecular spectroscopy*; Techniques in analytical chemistry series; John Wiley & Sons, 1998.

(181) Tauc, J. Optical properties and electronic structure of amorphous Ge and Si. *Mater. Res. Bull.* **1968**, *3* (1), 37–46. DOI: 10.1016/0025-5408(68)90023-8.

(182) Tauc, J.; Grigorovici, R.; Vancu, A. Optical Properties and Electronic Structure of Amorphous Germanium. *Phys. Status Solidi B* **1966**, *15* (2), 627–637. DOI: 10.1002/pssb.19660150224.

(183) Makuła, P.; Pacia, M.; Macyk, W. How To Correctly Determine the Band Gap Energy of Modified Semiconductor Photocatalysts Based on UV-Vis Spectra. *J. Phys. Chem. Lett.* **2018**, *9* (23), 6814–6817. DOI: 10.1021/acs.jpclett.8b02892.

(184) Hagfeldt, A.; Peter, L. M. Characterization and Modeling of Dye-Sensitized Solar Cells: A Toolbox Approach. In *Dye-sensitized Solar Cells*.

(185) Fabregat-Santiago, F.; Garcia-Belmonte, G.; Mora-Seró, I.; Bisquert, J. Characterization of nanostructured hybrid and organic solar cells by impedance spectroscopy. *Phys. Chem. Chem. Phys.* **2011**, *13* (20), 9083–9118. DOI: 10.1039/c0cp02249g.

(186) Soedergren, S.; Hagfeldt, A.; Olsson, J.; Lindquist, S.-E. Theoretical Models for the Action Spectrum and the Current-Voltage Characteristics of Microporous Semiconductor Films in Photoelectrochemical Cells. *J. Phys. Chem.* **1994**, *98* (21), 5552–5556. DOI: 10.1021/j100072a023.

(187) Bisquert, J.; Fabregat-Santiago, F. Impedance Spectroscopy: A general introduction and application to dye-sensitized solar cells. In *Dye-sensitized Solar Cells.* DOI: 10.1201/b16409.

(188) Bisquert, J. Chemical capacitance of nanostructured semiconductors: its origin and significance for nanocomposite solar cells. *Phys. Chem. Chem. Phys.* **2003**, *5* (24), 5360. DOI: 10.1039/b310907k.

(189) Bisquert, J.; Marcus, R. A. Device modeling of dye-sensitized solar cells. *Top. Curr. Chem.* **2014**, *352*, 325–395. DOI: 10.1007/128_2013_471.

(190) Bisquert, J.; Garcia-Belmonte, G.; Fabregat-Santiago, F.; Bueno, P. R. Theoretical models for ac impedance of finite diffusion layers exhibiting low frequency dispersion. *J. Electroanal. Chem.* **1999**, *475* (2), 152–163. DOI: 10.1016/S0022-0728(99)00346-0.

(191) Halme, J.; Miettunen, K.; Lund, P. Effect of Nonuniform Generation and Inefficient Collection of Electrons on the Dynamic Photocurrent and Photovoltage Response of

Nanostructured Photoelectrodes. *J. Phys. Chem. C* **2008**, *112* (51), 20491–20504. DOI: 10.1021/jp806512k.

(192) Halme, J. Linking optical and electrical small amplitude perturbation techniques for dynamic performance characterization of dye solar cells. *Phys. Chem. Chem. Phys.* **2011**, *13* (27), 12435–12446. DOI: 10.1039/C1CP21134J.

(193) Bisquert, J.; Janssen, M. From Frequency Domain to Time Transient Methods for Halide Perovskite Solar Cells: The Connections of IMPS, IMVS, TPC, and TPV. *J. Phys. Chem. Lett.* **2021**, *12* (33), 7964–7971. DOI: 10.1021/acs.jpclett.1c02065.

(194) Dloczik, L.; Ileperuma, O.; Lauermann, I.; Peter, L. M.; Ponomarev, E. A.; Redmond, G.; Shaw, N. J.; Uhlendorf, I. Dynamic Response of Dye-Sensitized Nanocrystalline Solar Cells: Characterization by Intensity-Modulated Photocurrent Spectroscopy. *J. Phys. Chem. B* **1997**, *101* (49), 10281–10289. DOI: 10.1021/jp972466i.

(195) Schlichthörl, G.; Huang, S. Y.; Sprague, J.; Frank, A. J. Band Edge Movement and Recombination Kinetics in Dye-Sensitized Nanocrystalline TiO_2 Solar Cells: A Study by Intensity Modulated Photovoltage Spectroscopy. *J. Phys. Chem. B* **1997**, *101* (41), 8141–8155. DOI: 10.1021/jp9714126.

(196) Thapa, D.; Huso, J.; Miklos, K.; Wojcik, P. M.; McIlroy, D. N.; Morrison, J. L.; Corolewski, C.; McCluskey, M. D.; Williams, T. J.; Grant Norton, M.; Bergman, L. UV-luminescent MgZnO semiconductor alloys: nanostructure and optical properties. *J Mater Sci: Mater Electron* **2017**, *28* (3), 2511–2520. DOI: 10.1007/s10854-016-5825-2.

(197) Thapa, D.; Huso, J.; Lapp, J.; Rajabi, N.; Morrison, J. L.; McCluskey, M. D.; Bergman, L. Thermal stability of ultra-wide-bandgap MgZnO alloys with wurtzite structure. *J. Mater. Sci.: Mater. Electron.* **2018**, *29* (19), 16782–16790. DOI: 10.1007/s10854-018-9772-y.

(198) Morrison, J. L.; Huso, J.; Che, H.; Thapa, D.; Huso, M.; Norton, M. G.; Bergman, L. The formation of MgZnO luminescent ceramics. *J. Mater. Sci.: Mater. Electron.* **2012**, *23* (2), 437–444. DOI: 10.1007/s10854-011-0530-7.

(199) Das, A. K.; Misra, P.; Ajimsha, R. S.; Bose, A.; Joshi, S. C.; Porwal, S.; Sharma, T. K.; Oak, S. M.; Kukreja, L. M. Effect of Mg diffusion on photoluminescence spectra of MgZnO/ZnO bi-layers annealed at different temperatures. *J. Appl. Phys.* **2013**, *114* (18), 183103. DOI: 10.1063/1.4830010.

(200) Hu, C.; Mi, J.; Shang, S.; Shangguan, J. The study of thermal decomposition kinetics of zinc oxide formation from zinc oxalate dihydrate. *J. Therm. Anal. Calorim.* **2014**, *115* (2), 1119–1125. DOI: 10.1007/s10973-013-3438-z.

(201) Sabira, K.; Muraleedharan, K. Exploration of the thermal decomposition of zinc oxalate by experimental and computational methods. *J. Therm. Anal. Calorim.* **2020**, *142* (3), 1315–1327. DOI: 10.1007/s10973-019-09169-6.

(202) Ringleb, A.; Ruess, R.; Hofeditz, N.; Heimbrodt, W.; Yoshida, T.; Schlettwein, D. Influence of Mg-doping on the characteristics of ZnO photoanodes in dye-sensitized solar cells. *Phys. Chem. Chem. Phys.* **2021**, *23* (14), 8393–8402. DOI: 10.1039/d1cp00179e.

(203) Song, J.; Zheng, E.; Liu, L.; Wang, X.-F.; Chen, G.; Tian, W.; Miyasaka, T. Magnesium-doped Zinc Oxide as Electron Selective Contact Layers for Efficient Perovskite Solar Cells. *ChemSusChem* **2016**, *9* (18), 2640–2647. DOI: 10.1002/cssc.201600860.

(204) Mali, S. S.; Patil, J. V.; Hong, C. K. Simultaneous Improved Performance and Thermal Stability of Planar Metal Ion Incorporated $CsPbI_2Br$ All-Inorganic Perovskite Solar Cells Based on MgZnO Nanocrystalline Electron Transporting Layer. *Adv. Energy Mater.* **2020**, *10* (3), 1902708. DOI: 10.1002/aenm.201902708.

(205) Rohwer, E.; Richter, C.; Heming, N.; Strauch, K.; Litwinski, C.; Nyokong, T.; Schlettwein, D.; Schwoerer, H. Ultrafast photodynamics of the indoline dye D149 adsorbed to porous ZnO in dye-sensitized solar cells. *ChemPhysChem* **2013**, *14* (1), 132–139. DOI: 10.1002/cphc.201200715.

(206) Benkö, G.; Kallioinen, J.; Korppi-Tommola, J. E. I.; Yartsev, A. P.; Sundström, V. Photoinduced ultrafast dye-to-semiconductor electron injection from nonthermalized and thermalized donor states. *J. Am. Chem. Soc.* **2002**, *124* (3), 489–493. DOI: 10.1021/ja016561n.

(207) Ramakrishna, G.; Jose, D. A.; Kumar, D. K.; Das, A.; Palit, D. K.; Ghosh, H. N. Strongly coupled ruthenium-polypyridyl complexes for efficient electron injection in dye-sensitized semiconductor nanoparticles. *J. Phys. Chem. B* **2005**, *109* (32), 15445–15453. DOI: 10.1021/jp051285a.

List of Abbreviations

ALD	Atomic layer deposition
$Co(bpy_3)$	Tris(2,2'-bipyridine)cobalt
$Cu(tmby)_2$	Bis-(4,4',6,6'-tetramethyl-2,2'-bipyridine)copper
DEZ	Diethylzinc
DSSC	Dye-sensitized solar cell
EQE	External quantum efficiency
IMPS	intensity-modulated photocurrent spectroscopy
IMVS	intensity-modulated photovoltage spectroscopy
$Mg(EtCp_2)$	Bis(ethyl cyclopentadienyl)magnesium
MOCVD	metal-organic chemical vapor deposition
MZO	Magnesium-doped zinc oxide
PCE	Photo conversion efficiency
PEDOT	Poly(3,4-ethylene dioxythiophene)
PLD	Pulsed laser deposition
TBP	4-tert-butyl pyridine
TCO	Transparent conductive oxide
TGA MS	Thermogravimetric analysis and mass spectroscopy
XRD	X-ray diffraction

List of Symbols

A	Absorbance
$AM1.5G$	Standard solar illumination
α	Absorptance
α_i	Absorption coefficient
α_t	Trap distribution parameter
β	Recombination parameter
c	Concentration
C_{CE}	Capacitance between electrolyte and counter-electrode
C_μ	Chemical capacitance
d	Layer thickness
d_{hkl}	Distance between parallel planes
D_n	Efficient diffusion coefficient
D_0	Diffusion coefficient of conduction band electrons
E_C	Conduction band energy
E_f	Fermi energy
E_{fn}	Quasi-Fermi energy
E_g	Band gap energy
E_{redox}	Redox potential of the electrolyte
E_V	Valence band energy
ε_λ	Wavelength-depended molar absorptivity of the dye
$E^0(S^+/S)$	Ground state of the dye
$E^0(S^+/S^*)$	Exited state of the dye
η_{col}	Charge-collection efficiency
η_{reg}	Regeneration efficiency
η_{inj}	Injection efficiency
η_{lh}	Light-harvesting efficiency
F_{hkl}	Structure factor
f_i	Atomic form factor
FF	Fill factor
$g(E_{fn})$	Exponential density of states distribution at the Fermi-level
I_T	Transmitted light intensity
I_0	Incident light intensity

$\hat{J}$	Amplitude of the AC current response
k_B	Boltzmann constant
k_{decay}	Rate constant for radiative and non-radiative decay
k_{inj}	Rate constant of electron injection
k_{rec}	Rate constant for recombination
$k_{rec\text{-}d}$	Rate constant for recombination to the dye
k_{reg}	Rate constant for dye regeneration
k_{tr}	Rate constant for electron transport
L_n	Electron diffusion length
n_c	Density of conduction band electrons
N_c	Effective density of conduction band states
n_t	Density of trapped electrons
N_t	Total trap density
P_{max}	Maximum power of a solar cell
P_0	Power of the incident light
q	Electrical charge
$\Phi(\lambda)$	Spectral flux density
$\hat{\phi}$	Amplitude of the modulated light intensity
R	Resistance
R_{CE}	Charge-transfer resistance
R_S	Series resistance
R_{tr}	Transport resistance
R_∞	Absolute reflectance
ρ	Reflectance
T	Temperature
τ	Transmittance
$\hat{V}$	Amplitude of the AC voltage response

List of Publications

Publication (I): *Influence of Mg-doping on the characteristics of ZnO photoanodes in dye-sensitized solar cells*, A. Ringleb, R. Ruess, N. Hofeditz, W. Heimbrodt, T. Yoshida, D. Schlettwein, Phys. Chem. Chem. Phys., **2021**, 23, 8393-8402

Publication (II): *Harnessing the Potential of Porous ZnO Photoanodes in Dye-Sensitized Solar Cells by Atomic Layer Deposition of Mg-Doped ZnO*, A. Ringleb, P. Klement, J. Schörmann, S. Chatterjee, D. Schlettwein, ACS Appl. Energy Mater., **2022**

Earlier contributions to publications related to the discussions in this work:

Dye-sensitized solar cells with electrodeposited ZnO and Co(bpy)(3) redox electrolyte: Investigation of mass transport in the electrolyte and interfacial charge recombination, R. Ruess, S. Haas, A. Ringleb, D. Schlettwein, Electrochim. Acta, **2017**, 258, 591-598

Diverging surface reactions at TiO2- or ZnO-based photoanodes in dye-sensitized solar cells, R, Ruess , S. Scarabino, A. Ringleb, K. Nonomura, N. Vlachopolous, A. Hagfeldt, G. Wittstock, D. Schlettwein, Phys. Chem. Chem. Phys., **2019**, 21, 13047-13057

Efficient Electron Collection by Electrodeposited ZnO in Dye-Sensitized Solar Cells with $TEMPO^{+/0}$ as the Redox Mediator, R. Ruess, J. Horn, A. Ringleb, D. Schlettwein, J. Phys. Chem. C, **2019**, 36, 22074-22085

Acknowledgements

First and foremost, I would like to thank my supervisor Prof. Schlettwein for his long-standing support of my scientific career. Since I came to him to ask for supervision of an external bachelor thesis, he always had an open ear and mind about my ideas and pointed out opportunities, that had wide-reaching effects on my future. I much appreciate the variety of professional and personal experiences I had during my years in this group.

I also would like to thank Prof. Tsukasa Yoshida for hosting me in his group at Yamagata University in Yonezawa, Japan. The experience performed under his supervision played an important role in the early parts of this project and the opportunity to visit Japan will stay with me as a life-long memory.

A huge thanks to the Deutsche Bundesstiftung Umwelt (DBU) whose financial support made this work possible in the first place. I am proud to call myself an alumnus of this organization and hope to stay in contact throughout my career with the DBU and my fellow alumni.

A special thanks goes to my former co-supervisor Dr. Raffael Ruess for introducing me to the field of DSSCs and always having an open door for questions and discussions, even after leaving the group.

I also want to thank Dr. Philip Klement for his great efforts in establishing the ALD deposition of MZO and never turning down any of my numerous requests or ideas for additional studies as well as his contributions as a co-author. These thanks naturally extend to the rest of my co-authors Nico Hofeditz and Prof. Wolfram Heimbrodt from Marburg University and Prof. Sangam Chatterjee from JLU Gießen, who’s contributions added great value to the publications.

Naturally I would like to thank all current and past members of Prof. Schlettwein´s group for their scientific and moral support during the years. Our traditional meetings on Friday will be missed.

Lastly, I would like to thank my family for their continued support during the years. Without their help, my career and by extension this doctoral thesis would not have been possible.